On the Modelling and Characterisation of Photoconducting Antennas

Fiorellini Bernardis, A.

DOI
10.4233/uuid:469e35d4-7aa8-4301-94a0-17baceb3af1c

Publication date
2022

Document Version
Final published version

Citation (APA)
Fiorellini Bernardis, A. (2022). *On the Modelling and Characterisation of Photoconducting Antennas*. [Dissertation (TU Delft), Delft University of Technology]. https://doi.org/10.4233/uuid:469e35d4-7aa8-4301-94a0-17baceb3af1c

On the Modelling and Characterisation of Photoconducting Antennas

Arturo (A.) Fiorellini Bernardis

May 3, 2022

On the Modelling and Characterisation of Photoconducting Antennas

DISSERTATION

for the purpose of obtaining the degree of doctor
at Delft University of Technology
by the authority of the Rector Magnificus, Prof.dr.ir. T. H. J. J. van der Hagen,
chair of the Board of Doctorates,
to be defended publicly on
Tuesday 24 May 2022 at 12:30 o'clock

by

Arturo FIORELLINI BERNARDIS

Master of Science in Electrical Engineering,
Delft University of Technology, The Netherlands
born in Padua, Italy.

This dissertation has been approved by the promotors.

Composition of the doctoral committee:

Rector Magnificus,	Chairman
Prof.dr. N. Llombart Juan,	Delft University of Technology, promotor
Prof.dr. A. Neto,	Delft University of Technology, promotor
Independent members:	
Prof.dr.ir J. J. A. Baselmans,	Delft University of Technology
Prof.dr. J. Gomez Rivas,	Eindhoven University of Technology
Prof.dr. J. Romeu Robert,	Technical University of Catalonia, Spain
Prof.dr A. Freni,	University of Florence, Italy
Dr.ir A. J. L. Adam,	Delft University of Technology
Reserve member:	
Prof.dr. A. Yarovoy,	Delft University of Technology

The work presented in this thesis has been carried out at TU Delft and financed by the European Research Council starting grant (ERC-2014-StG LAA-THz-CC), no. 639749.

Keywords, Photoconductive Antennas, Photoconductive Sources, Lens Antennas, Terahertz, time-domain sensing, time-domain spectroscopy, advanced antenna architectures

To me,
you already have the acknowledgements.

Contents

Chapter 1

Introduction

In the last 30 years the interest in terahertz (THz) technology sparked thanks to the emergence of the many possible applications in spectroscopy, imaging and security screening: the THz bandwidth can indeed be exploited to study biological samples and help medical diagnostics; it serves as a harmless non-destructive testing (NDT) technique for medical and pharmaceutical products; it is used to inspect food and other packaging for quality control in a non-invasive fashion; it is adopted in body scanner systems for security screenings of people [1, 2, 3, 4, 5, 6, 7, 8, 9].

Many of these new emerging applications rely on the adoption of photoconducting antennas (PCAs), optoelectronic sources able to radiate and detect electromagnetic fields in the THz spectrum. PCAs consist in a metallization printed over a substrate of photoconducting material and radiating into a dense dielectric lens, while excited by pulsed optical signals, thus exploiting the photoconductive effect. Moreover, they come at a relatively low cost, thanks to the recent advancements in semiconductor technology [10, 11, 12, 13, 14, 15].

Typically, PCAs suffer from low levels of radiated THz power, making them inconvenient to use in long-range applications due to the excessively long integration time required to detect the signals. Moreover, for portability and maintenance reasons, they usually are excited by in-fibre travelling laser pulses: this sets a limit to the maximum power travelling along the optical fibre due to its intrinsic dispersion.

So far, most of the scientific community focused mainly on the engineering of the material, trying to increase the amount photocurrent induced by the same optical

excitation and biasing conditions [1, 10, 11, 16]. On the other hand, scarce effort has been directed to improve the antenna architecture and its radiation properties, and the coupling with the quasi-optical path guiding the radiated fields. In order to obviate to these issues and increase the power radiated by these sources, effective tools to aid the analysis and improve the design of PCAs are essential. Indeed, to obtain an equivalent circuit that accounts for the physical phenomena involved in the photocurrent generation and conjugates them to the electromagnetic effect of the radiation can thus lead to photoconductive source designs that are more efficient in terms of emitted THz power.

1.1 THz time domain sensing and spectroscopy systems

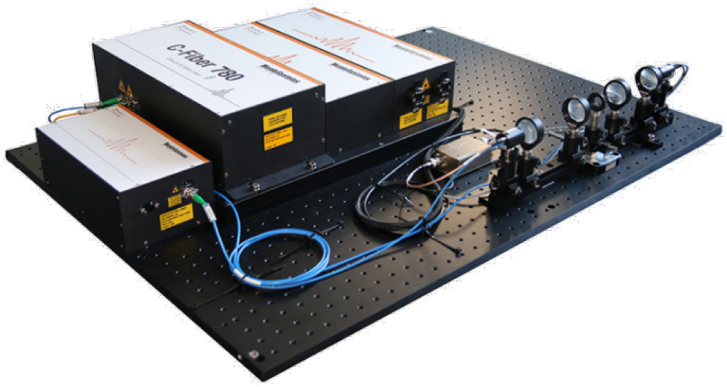

Figure 1.1: All fiber coupled TDSS system: TERA K15 available at Menlo Systems GmbH

The availability of PCAs has given rise to the emergence of THz time domain sensing and spectroscopy (TDSS) systems, Fig. 1.1, that stand out as one of the most efficient techniques to study plasmas, phonons in crystalline solids, molecular dipoles and relaxation dynamics in hydrated biological samples [1, 16]. TDSS systems typically consists in two communicating photoconducting antennas (PCAs)

[10, 17, 18, 19], one in transmission (TX) and one in reception (RX). Such sources rely on semiconductors that, when excited by optical lasers, are characterised by photo-carriers with high mobility and short life-times: these properties are exploited to generate signals with spectral components ranging from a few hundreds of GHz to a few units of THz. These frequencies couple with the meV energy transitions and pico-seconds transient dynamics typical of the aforementioned applications [12].

Current TDSS commercial systems are based on single planar antenna geometries, printed on a semiconductor, and coupled to a high resistivity (HR) silicon (Si) lens [9]. In particular, the gap of the antenna is periodically (80-100 MHz) shined by a femtoseconds (e.g. with full width at half maximum FWHM of 100 fs) laser pulse with a wavelength matched to the semiconductor energy gap.

1.1.1 Common antenna geometries

The most widely adopted planar antenna geometries are the Auston switch, the bow tie, and the logarithmic spiral antenna, Fig. 1.2. These feeds are typically coupled to high resistivity Silicon lenses to increase the directivity, thus the illumination of the lenses is crucial to obtain optimal radiation patterns outside the lens. An extensive analysis of these three antenna architectures can be found in [20], and only a brief overview is offered in this section.

Auston switch the radiation pattern characteristics of the Auston switch are quite poor. Both the angular pattern and the polarisation are frequency dependent. At low frequencies the radiation is mostly generated by the bias lines, which illuminate only the lateral portion of the lens surface. Only at very high frequencies does the Auston switch start to radiate towards the central portion of the lens, when the photocurrent spectrum is significantly decayed already. The radiation patterns of the field radiated by the feed into the HR silicon lens are showed in Fig. 1.3 for two frequency points, [21].

Bow tie the radiation pattern of the bow tie is rather stable as a function of the frequency, as its polarisation. However, due to the leaky wave effect also this feed illuminates mostly the lateral portion of the lens. The radiation patterns

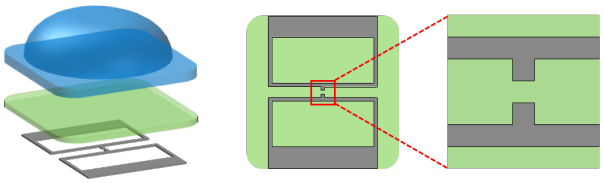

(a) Auston switch

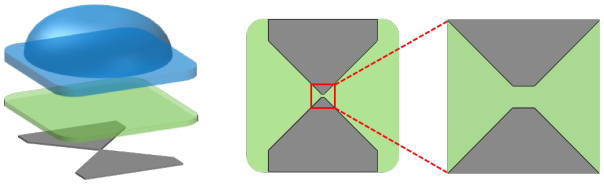

(b) Bow tie

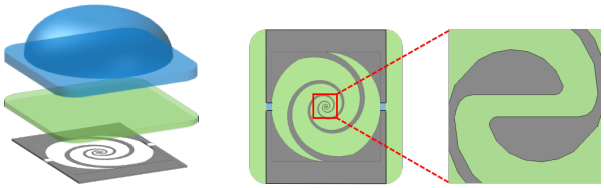

(c) Logarithmic spiral

Figure 1.2: Most common antenna geometries for PCAs adopted in TDSS systems

of the field radiated by the feed into the HR silicon lens are showed in Fig. 1.4 for two frequency points, [21].

Logarithmic spiral the radiation pattern of the logarithmic spiral illuminates the lens in a more uniform and symmetric way, with an angular pattern directed towards the top of the lens. Only at high frequencies does the pattern start to be degraded. The radiation patterns of the field radiated by the feed into the HR silicon lens are showed in Fig. 1.5 for two frequency points, [21].

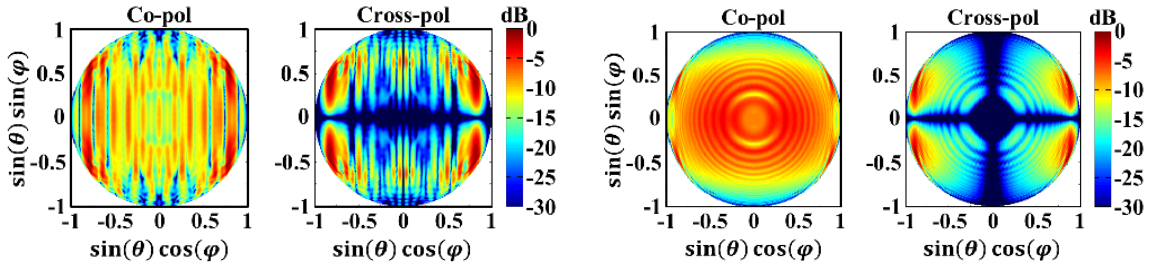

(a) 0.5 THz (b) 1.5 THz

Figure 1.3: Simulated 2D radiation patterns of the Auston switch; field radiated into the dielectric lens (primary field).

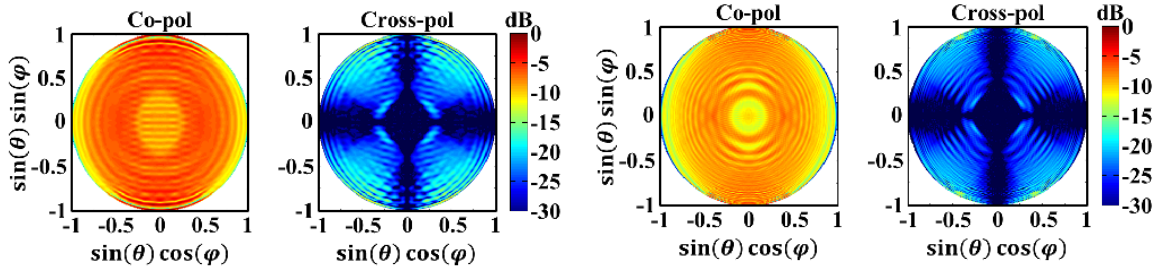

(a) 0.5 THz (b) 1.5 THz

Figure 1.4: Simulated 2D radiation patterns of the bow tie antenna; field radiated into the dielectric lens (primary field).

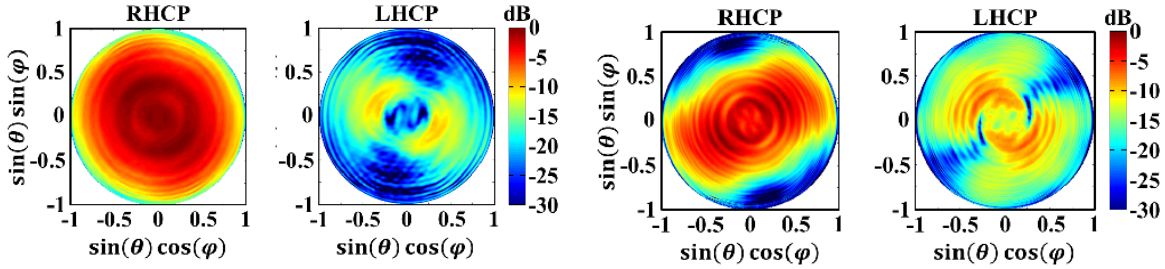

(a) 0.5 THz (b) 1.5 THz

Figure 1.5: Simulated 2D radiation patterns of the logarithmic spiral antenna; field radiated into the dielectric lens (primary field).

1.1.2 Leaky lens antenna architecture

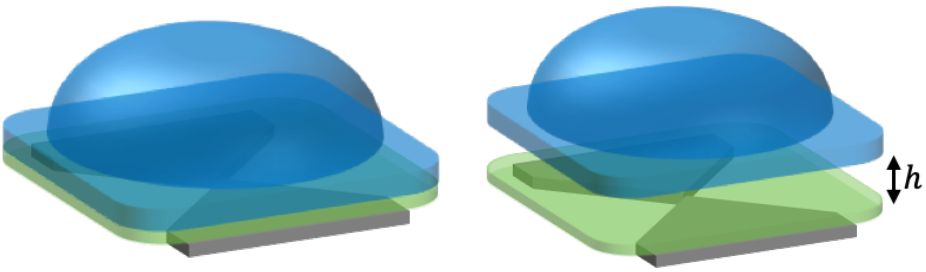

Figure 1.6: Layered structure of a two different PCAs. (a) The HR silicon lens is glued directly on top of the semiconductor membrane. (b) A small air gap is placed in between the semiconductor membrane and the lens to exploit the leaky wave phenomenon.

This subsection highlights how the introduction of an air cavity between the photoconductive membrane on which the metallisation is printed and the HR silicon lens leads to advantages in terms of directivity, pattern symmetry and polarisation purity, characteristics that are especially useful in time domain sensing applications, [22]. Indeed, in order to improve the pattern of the planar antennas listed in the previous subsection, to introduce an air gap between the metallization and the lens is sufficient to enable a broad-band leaky radiation towards the lens vertical axis [22]; note that the gap is small with respect to the wavelength of the radiated field. The resulting leaky wave antenna, characterised by a stable radiation phase centre, improves the directivity of the PCA radiation pattern and its coupling with the QO channel. Fig. 1.7 from [22] shows the 2D simulated radiation pattern in absolute value of the leaky wave bow tie antenna for two frequency points, 0.5 THz and 2 THz, as opposed to the patterns of a standard bow tie showed in Fig. 1.4.

To exploit the leaky wave effect improves mainly three efficiency parameters thanks to the better illumination of the lens: the reflection efficiency, the Gaussian beam efficiency and the relative phase error. However, it has to be noted that in case the air gap height becomes comparable to the radiated wavelength the front to back ratio may end up significantly worsened; this is especially relevant for the higher frequency portion of the radiated spectrum.

An enhanced leaky wave PCA will be characterised in Chapter 4: so far, there has not been any experimental validation of PCAs exploiting the leaky wave phenomenon.

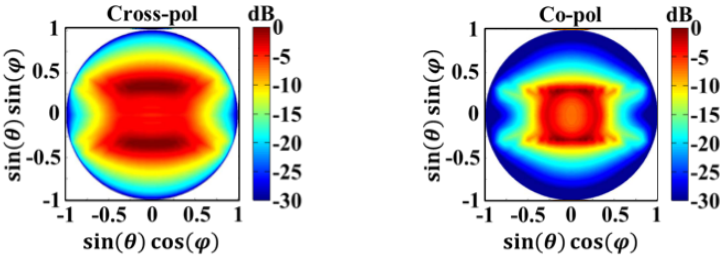

(a) 0.5 THz (b) 2 THz

Figure 1.7: Simulated 2D radiation patterns of the leaky wave bow tie antenna; field radiated into the dielectric lens (primary field), [22]. The electrically small air gap improves the directivity of the pattern and lead to a more efficient illumination of the lens, see Fig. 1.4

1.2 Working principles of PCA sources

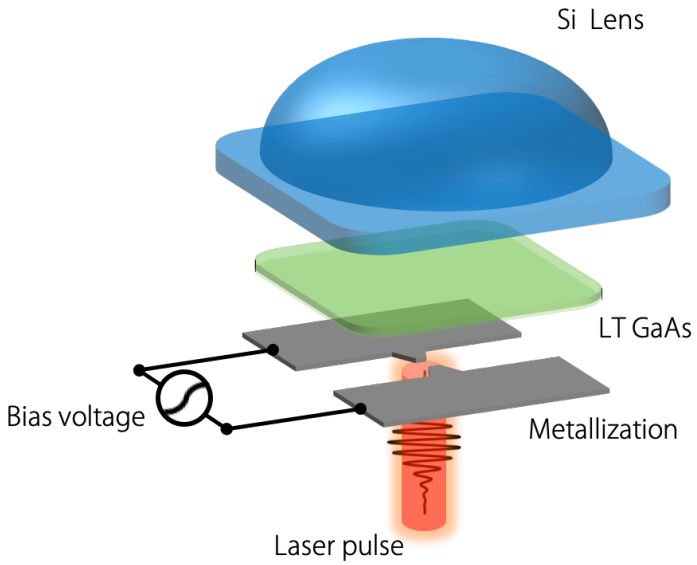

Figure 1.8: Schematic of a PCA in transmission. A metallization, biased at a constant voltage, printed over a PC substrate, excited by a pulsed laser and radiating into a HR dielectric lens

A photoconductive antenna (PCA) consists of a metallization biased to a constant voltage level, printed over a photoconductive substrate, excited by a pulsed laser and radiating into a dense dielectric lens, Fig. 1.8. When a laser pulse with carrier frequency matched to the band gap of the semiconductor impinges on the device gap, the provided energy injects free electrons from the valence to the conduction band. In the PCA in transmission (TX) the injected photocarriers are accelerated by an applied bias voltage, while in the PCA in reception (RX) by the EM field radiated by the former. In the following, TX PCAs will be considered.

Generation and recombination processes are both active for the whole duration of the laser pulse, although the recombination is much slower than the generation, that can be considered instantaneous. Moreover, the recombination time constant in LT-GaAs is typically longer than the duration of the fs optical pulse used to pump the material. For these reasons, the recombination can be neglected during the duration of the optical pulse. Thus, one can imagine carriers to keep getting

injected into the conduction band when the laser is active, while they then are progressively reabsorbed by the material once the excitation is no longer active.

The photo-carrier generation process induces a time dependent change in the carrier density within the gap; the free charges are then accelerated by the bias applied over the gap, effectively generating a time-varying current flowing through the excited volume. Eventually, this current induces a radiation that in turn tends to counteract the field applied over the gap of the PCA. Since the amplitude of the carrier density depends on the optical pulse, the larger the power shone onto the antenna, the larger the current, and the stronger the radiation: when the amplitude of the radiated field becomes comparable to the forced bias voltage, the gap is effectively short-circuited. This phenomenon sets a maximum level to the current that can be achieved with TX-PCAs, and is referred to as radiation field screening.

1.2.1 Electrically small photoconductive gaps

Photoconductive antennas are characterised by a gap over which the laser is shone that is small with respect to the wavelength of the EM field that is radiated. For such sources, a distinctive effect limiting their THz power output is the saturation emerging when larger and larger optical excitations are used to pump the PC substrate; the majority of the authors have associated this saturation to screening effects introduced by the antenna radiation and\or space charge build-up, [11, 23, 24, 25].

Several equivalent circuits have been proposed in the literature [26], although all of them required *a posteriori* fine tuning procedures to have the predictions matched to the measurements, making them inconvenient for the design of PCAs.

1.3 Equivalent circuits for PCA sources

Among the many equivalent circuits developed to predict the behaviour of PCAs, two of the most significant are going to be introduced here. In [27], the authors presented a model characterised by time-varying components and different sources: a constant voltage source representing the bias, V_b; a constant resistance representing the antenna radiation resistance, R_a; a time-varying component representing

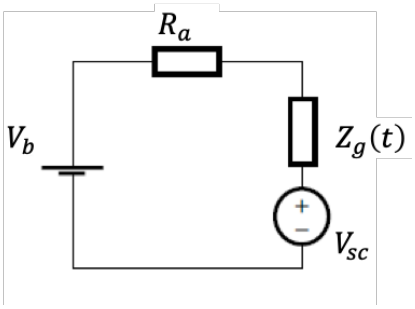

Figure 1.9: time-domain equivalent circuit presented in [27]

the impedance of the gap, $Z_g(t)$; a constant voltage source representing the screening induced by the space-charge region, V_{sc}. This model, Fig. 1.9, ascribed the saturation of the power radiated by PCAs under pulsed lasers to a reduction of the effective field applied over the PCA gap due to both the feedback from the antenna radiation together with a region of space-charge building up during the operation. However, the amplitude of V_{sc} was experimentally tuned a-posteriori to match the measurements. Moreover, the tool does not account for possible effects of the forcing field over the motion of the induced photocarriers, translating in to an impedance presented by the gap, $Z_g(t)$, that has no dependence on the bias.

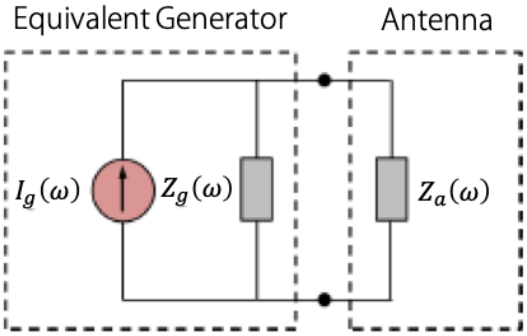

Figure 1.10: Norton equivalent circuit presented in [28]

In [28], the authors introduced an equivalent Norton model in the frequency domain, Fig. 1.10, consisting in an equivalent generator, $I_g(\omega), Z_g(\omega)$, feeding

the antenna radiation impedance, $Z_a(\omega)$. The circuit is easy to use to design antennas, as it constructed with frequency dependent component; also, it gives accurate results in case of low optical excitations, when the radiation field screening effect can be neglected. However, in order to match the measurements even under large optical excitations, the DC mobility adopted by the model needed to be tuned as a function of the average power of the laser, [29]. Arguably, the inaccuracy of the model was due to the fact that only a DC mobility was adopted, and radiation screening effects over the gap potential were not considered. The Norton model in [28] was indeed constructed assuming that the voltage across the PCA gap remained constant during the whole evolution of the induced photocurrent, approximation that holds only in case of very weak optical excitations. Finally, also this tool does not account for possible effects of the forcing field over the motion of the induced photocarriers, translating in to an impedance presented by the gap, $Z_g(\omega)$, that has no dependence on the bias.

1.4 Novel contributions of this thesis

This thesis introduces a novel equivalent circuit that predicts the behaviour of photoconductive antennas subject to optical excitations. Stemming from a careful time-domain analysis of the physical processes involved in the photocarrier generation, motion and recombination in a semiconductor excited by a pulsed laser, an equivalent circuit model in time domain is then derived; the model is immediate to translate in the frequency domain in order to deal with electromagnetic concepts such as the antenna impedance and the quasi-optical channel efficiency. The procedure is applied to the analysis and characterisation of a photoconductive device manufactured with a substrate of Low Temperature grown Gallium Arsenide (LT-GaAs), excited by a pulsed femtosecond laser, fed by a constant bias voltage and radiating into a HR silicon lens.

The analysis starts resorting to the Drude-Lorentz model [30, 31] to assess the behaviour of the carrier density change induced by the optical excitation, [32, 33]; the forcing bias field is then included, represented by a voltage source, as well as the impedance introduced by the antenna structure itself, evaluated through a full wave software analysis; eventually, the procedure proceeds constructing an

equivalent circuit in time domain that can be solved following the time-stepped procedure presented in [34].

The equivalent circuit estimates the temporal evolution of the photocurrent induced in the gap of PCAs and of the transient voltage across it, all the while including the parameters of the photoconducting material as well as of the laser exciting it. The time-evolving photocurrent is then translated into the spectral domain to use it and operate with the radiation characteristics of the antenna and the efficiency of the quasi optical path, evaluated through in-house tools and EM software. Moreover, the equivalent circuit gives a clear picture of what concurs in the generation of the emitted THz field and what limits it, such as radiation field screening effects. The model allows one to analyse the entire power budget of the system, from the laser exciting the transmitter to the field captured by the receiver, while accounting for all the characteristics of the optical signal, the semiconductor, the antenna architecture and radiation pattern and the quasi optical channel.

The hereby introduced procedure aims at bridging the gap between the pure material engineering and the antenna engineering, serving as a tool to analyse the behaviour of PCAs and to evaluate the power budget of the entire link, from the excited semiconductor of the transmitter to the power detected by the receiver.

The model is validated by comparison of the expected power and spectra with data collected from a measurement campaign. Thanks to the accurate analysis of the generation, motion and recombination of the photocarriers the model does not overestimate the induced current, and the results agree exceptionally well, without any a-posteriori tuning procedures, needed instead in [27, 28, 29]. The methodology stands out as a great tool for a faster analysis as well as a better design of PCAs.

Furthermore, it has been developed a novel methodology to aid the design of receiving terminal antennas immersed in complex scattering scenarios and maximise the received power: the observable field. This procedure estimates the maximum portion of a generic incident field that an ideal antenna, allocated in a certain volume, can receive. In particular, the observable field is defined as the portion of the field impinging on the device that contributes to the available power. The methodology results especially beneficial in environments where the incident field can be expressed as a summation of multiple coherent planes waves,

such as those present in sensing (e.g. communicating PCA's in TDSS systems) and communication scenarios, where the receiver is found close to multiple scatterers. In such situations, the knowledge of the amplitude, the phase, and the direction of incidence of the different contributions can be used to fine-tune the design of the receiving antenna pattern.

1.5 Outline of this thesis

This thesis consists of four main parts. Part 1, consisting of Chapter 2, presents the theoretical derivation of an equivalent circuit model proposed to analyse PCAs; Part 2, consisting of Chapter 3 and 4, presents the experiments conducted to characterise different PCAs and to test the model against the acquired measurements; Part 3, consisting of Chapter 5, presents a theoretical model that aims to aid the design of receiving antennas immersed in complex scattering scenarios; Part 4, consisting of Chapter 6, presents the conclusions and lists possible outlooks of this work. A more detailed list is given in the following:

Chapter 2 The expression for the photocurrent is derived. The analysis starts resorting to semiconductor physics to model the behaviour of the carrier density change induced by the optical excitation. The main simplifying hypotheses are introduced. The forcing bias field is then included, represented by a voltage source, as well as the impedance introduced by the antenna structure itself, evaluated through a full wave software analysis. The results given by the equivalent circuit in time domain are presented for different antennas and material parameters.

Chapter 3 Presented here is the experiment to characterise a bow tie PCA. First, the design of the antenna itself is outlined, then the whole measurement setup adopted is detailed thoroughly: the adopted instrumentation, the design of the laser delay line, the focusing of the beam and its profile measurement. The power detected as a function of the optical excitation is showed and then compared to the predictions from the model. Finally, the detected time evolving pulse is showed together with its spectral distribution.

Chapter 4 Presented here is the experiment to characterise a leaky wave PCA. First, the design of the antenna itself is outlined, then the whole measurement setup adopted is detailed thoroughly: the adopted instrumentation, the design of the laser delay line, the focusing of the beam and its profile measurement. The power detected as a function of the optical excitation is showed and then compared to the predictions from the model.

Chapter 5 Presented here is the procedure to derive the observable field for a terminal antenna immersed in a complex scattering scenario. Given a generic incident field and fixed antenna volume, the observable field aims to derive the best possible current distribution to capture it. The derivation of angular distribution and amplitude is detailed, and then of the available power. Finally, a practical situation is pictured to test the observable field in real case scenarios.

Chapter 6 The most significant results together with future outlooks for this work are presented here.

Appendix A This appendix describes the arithmetical steps used to calculate the amplitude of the optical excitation that is then adopted in the time domain equivalent circuit of Chapter 2.

Appendix B This appendix shows the Thevenin representation of the PCA, leading to the same results as the Norton equivalent circuit introduced in Chapter 2.

Appendix C This appendix describes the manufacturing process of the leaky wave PCA characterised in Chapter 4.

Appendix D This appendix shows the procedure to derive the homogenous plane wave expansion of a generic incident field in the surroundings of a point, later used in Chapter 5.

Appendix E This appendix explains the steps to evaluate the amplitude of the observable field, introduced in Chapter 5, by means of reaction integrals.

Appendix F This appendix shows how the classic Drude model can be used along with transmission line theory to improve the design of bulk absorber for

any frequency, with focus on the THz range. This appendix focuses on the measurement performed to validate the technique, which is instead thoroughly detailed in [31].

Chapter 2

Time domain modelling of pulsed photoconducting sources

Presented here is the procedure for the derivation of a novel equivalent circuit in time domain to analyse and predict the behaviour of PCAs subject to optical excitation and to a forcing voltage potential. The model is constructed starting from a careful analysis of generation, motion and recombination of photocarriers in a semiconductor based on the Drude-Lorentz model, which accounts for the electrical properties of the PC material, such as scattering and recombination time. The electromagnetic features of the antenna architecture are evaluated resorting to EM software and included in the derivation of an equivalent circuit in time domain. The circuit model predicts the temporal evolution of voltage and current in a PCA, as well as the radiated power and its spectral distribution with great accuracy, standing out as an effective tool to analyse and design these devices. In the following, the analysis will focus on PCAs excited by periodically pulsed lasers and biased to a constant voltage.

2.1 Introduction

In recent years the interest in terahertz (THz) technology has been driven by the possibility of building instruments to work with the THz bandwidth (0.3-3 THz) of the EM spectrum while maintaining a relatively low cost [2, 3, 7]. These instruments

typically make use of the field radiated and received by two communicating PCAs to study the object under test.

PCAs are patterned metallization printed over semiconductor substrates and radiating into HR silicon lenses. These devices exploit the generation of electron-hole pairs happening when the semiconductor is illuminated by an optical signal with the appropriate carrier frequency. The carriers are accelerated by a constant bias voltage in the emitter, while in the receiver they are accelerated by the field radiated by the former, eventually producing a time-varying current flowing across the gap of the device.

This chapter studies PCAs operating in transmission, illuminated by pulsed fs lasers, biased to a constant voltage potential; also, small area emitters are considered, characterised by a photoconductive (PC) gap over which the laser is shone that is small with respect to the wavelength of the EM field that is radiated. For such sources, a distinctive effect limiting their THz power output is the saturation emerging when larger and larger optical excitations are used to pump the photoconductive substrate.

Different authors gave different explanations as to why this happens, and to explain this behaviour several equivalent circuits have been proposed in the literature, [26, 28, 29]. However, all these circuits present cumbersome derivations of multiple sources and different lumped components, and\or *a posteriori* tuning based on the collected data to make the predictions match against the measurements.

In contrast with previous works, introduced here are the steps to derive an equivalent circuit in time domain composed of a single source, a component describing the excited volume of the photoconductor and a component representing the radiation of the antenna. The circuit predicts the temporal evolution for the voltage and the current in the load, the average radiated power as well as its spectral distribution accurately, without the need of any *a posteriori* fine tuning of the circuit components, as in [27, 29], even in the case of high optical excitations.

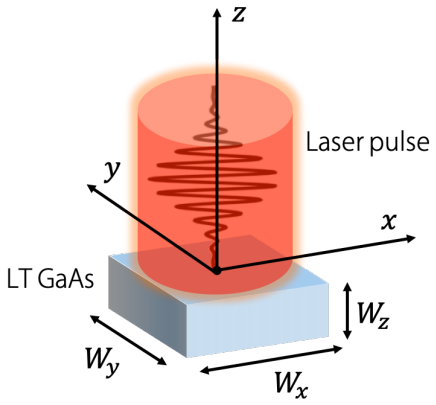

Figure 2.1: Reference system and dimensions of the illuminated gap of the PCA under analysis

2.2 Photocurrent induced in a biased photoconductor under pulsed optical excitations

The active portion of the photoconducting source with a volume is identified as $Vol = W_x W_y W_z$, as shown in Fig. 2.1, where the z axis is orthogonal to the dielectric slab, the x axis parallel to the biasing electric field, and the y axis transverse to the direction of propagation of the current. The semiconductor adopted is low temperature grown Gallium Arsenide (LT GaAs).

2.2.1 Simplifying hypotheses

When the gap of the PCA, Vol, is illuminated by a laser pulse with a carrier frequency slightly exceeding the band gap of the semiconductor, $f_c = 780nm$, electrons are injected from the valence into the conduction band, and electron-hole pairs are generated. The carrier generation function, indicated as $g_{gen}(t, \vec{r})$, is different for every observation point in time, t, and space, $\vec{r}$, within the volume of the PCA gap, Vol, since the optical excitation does not have a constant intensity profile in (x, y) and is absorbed along z with an exponential decaying function. However, for the sake of simplicity the photo-carrier generation function is averaged across the whole active volume, $\bar{g}_{gen}$ (refer to Appendix A).

Moreover, since the dimensions of Vol are small in terms of the radiated wave-

Laser parameters	
Wavelength	$\lambda_c = 780nm$
Pulse FWHM	$\tau_p = 100fs$
Repetition rate	$T_L = 12.5ns$
Semiconductor parameters	
Carrier recombination time	$\tau_{rec} = 300fs$
Carrier scattering time	$\tau_s = 8.5fs$
Dielectric constant	$\varepsilon = 12.96$
Electron effective mass	$m_e = 0.067m_0$
Plane wave reflection coefficient	$\Gamma = 0.5477$
Absorption coefficient	$\alpha = 1\mu m$
Ideal optical efficiency ($W_{x,y} = W_{gap}$)	$\eta_{opt} = 0.35$
Constants	
Planck's constant	$h = 6.63 \cdot 10^{-34} m^2 kg/s$
Electron mass	$m_0 = 9.11 \cdot 10^{-31} kg$
Electron charge	$q_e = 1.6 \cdot 10^{-19}$ C

Table 2.1: List of parameters adopted in this thesis

length spectrum, the electric field over the gap, $\vec{e}_g(t,\vec{r})$, can be assumed independent from z, uniform along (x,y), and oriented along $\hat{x}$, such that $\vec{e}_g(t) \simeq e_g(t)\hat{x}$. These hypotheses for the carrier density and the electric field distribution simplify the analysis, and justify the use of a lumped circuit representation for the PCA gap.

2.2.2 Induced photocurrent derivation

A theoretical description of the photocurrent induced in semiconductors under pulsed lasers is presented in [33]. In order to arrive to a conclusive expression for the current density flowing across the PCA gap, the procedure begins characterising the motion of charge particles adopting the Drude-Lorentz model, under all the assumptions stated above:

$$\frac{d}{dt}\vec{v}_c(t) + \frac{\vec{v}_c(t)}{\tau_s} = \frac{q_e}{m_e}\vec{e}_g(t) \tag{2.1}$$

where $\vec{v}_c(t)$ is the carrier velocity, τ_s the carrier scattering time, q_e is the electron charge, m_e is the effective mass of the electron in LT-GaAs and $\vec{e}_g(t)$ is the electric field applied over the PCA gap. The solution of equation (2.1) yields:

$$\vec{v}_c(t,t'') = \int_{t''}^{t} \mu(t-t')\vec{e}_g(t')dt' \tag{2.2a}$$

$$\mu(t) = \frac{q_e\tau_s}{m_e}\frac{e^{-\frac{t}{\tau_s}}}{\tau_s} = \mu_{DC}\frac{e^{-\frac{t}{\tau_s}}}{\tau_s} = \left[\frac{m^2}{Vs^2}\right] \tag{2.2b}$$

where $\mu(t)$ is the time domain mobility response function, μ_{DC} is the well-known DC frequency domain mobility, t is the time of observation and t'' represents the time of arrival of the excitation. Next, the partial carrier density is introduced, $n_p(t,t'')$, which accounts for all the carriers injected into the conduction band at t'' and not yet reabsorbed by the substrate when observed at t:

$$n_p(t,t'') = Ag_{gen,N}(t'')h_{GaAs}(t-t'') = \left[\frac{1}{m^3 s}\right] \tag{2.3a}$$

$$g_{gen,N}(t) = e^{-4ln2\frac{t^2}{\tau_p^2}}, h_{GaAs} = e^{-\frac{t}{\tau_{rec}}} \tag{2.3b}$$

where $g_{gen,N}(t)$ is the Gaussian normalised temporal envelope of the carrier generation function corresponding to the optical excitation, τ_p is the full width at half maximum (FWHM) duration of the optical excitation h_{GaAs} is the material impulse response, τ_{rec} is the average carrier recombination constant, and A is the amplitude of the excitation as defined in Appendix A, which results:

$$A = \eta_{opt} \frac{\tilde{P}_L}{h f_c} \frac{T_L}{\tau_p} \sqrt{\frac{4ln2}{\pi}} \frac{1}{Vol} \tag{2.4}$$

η_{opt} is an efficiency parameter that accounts for the spill-over of the optical pulse over the gap, its absorption in z and the reflection the dielectric-air interface. $\tilde{P}_L$ is the average power of the pulsed laser, h is the Planck's constant, f_c is the laser carrier frequency, T_L is the laser repetition rate. All the values of the parameter of equations (2.1), (2.2), (2.3), (2.4) are enlisted in Table 2.1.

Note that both the generation and recombination functions, (2.3b), are active as soon as the laser pulse starts; however, the generation lasts only when the pulse is active, while the recombination does until all the electron-pair holes are recombined. This means that free carriers keep getting injected into the conduction band and reabsorbed during the whole pulse duration, but since the generation can be considered instantaneous and $\tau_p < \tau_{rec}$, the generation is dominant at earlier time instants, and the effect of the recombination can be neglected while the pulse is active. For this reason, the current reaches its maximum amplitude approximately at the end of the pulse. This is not immediately visible from (2.3a), since it is a partial density function which needs to be integrated.

Using (2.2), (2.3) the partial current density is introduced, which represents the amount of current observed at t generated by an excitation at t'' (note that there is an additional s^{-1} dependence with respect to a current density, as the partial carrier density defined in (3.a) is being used):

$$\vec{j}_{g,p}(t, t'') = q_e n_p(t, t'') \vec{v}_c(t, t'') = \left[\frac{A}{m^2 s}\right] \tag{2.5}$$

To obtain the photocurrent density, one needs to account for every excitation instant

in t'', and integrate (2.5) for the distributed temporal evolution of the pulse:

$$\vec{j}_g(t) = \int_{-\infty}^{t} \vec{j}_{g,p}(t, t'')dt'' \tag{2.6}$$

The latter expression, (2.6), is a double temporal convolution that accounts for history in the process of generating, accelerating and recombining the photocarriers.

Averaging the current density in (2.6) over the cross section of the active gap, and assuming that it is oriented only parallel to the electric field, $\vec{j}_g(t) = j_g(t)\hat{x}$, the net photocurrent flowing across the gap results:

$$j_g(t) = \int_{W_x}\int_{W_y} \vec{j}_g(t) \cdot \hat{x}dxdy \tag{2.7}$$

Similarly, integrating the electric field along the gap a voltage drop is obtained:

$$v_g(t) = \int_{W_x} \vec{e}_g(t) \cdot \hat{x}dx = e_g(t)W_x \tag{2.8}$$

Eventually, substituting (2.2), (2.3), (2.3), (2.5), (2.6), (2.8) in (2.7), one obtains a conclusive relation for the induced photocurrent that links it to the time-varying voltage over the gap:

$$i_g(t) = q_e \frac{W_y W_z}{W_x} \int_{-\infty}^{t} n_p(t, t'') \int_{t''}^{t} \mu(t - t')v_g(t')dt'dt'' \tag{2.9}$$

Equation (2.9) represents a deterministic relation between voltage and current valid for the general case where the photocarrier injection is induced by a pulsed laser, and the semi-conductor can be characterised by a carrier scattering time, τ_s, from the Drude-Lorentz model, and a recombination time, τ_{rec}, representing the impulse response of the material. To determine the temporal evolution of the voltage across the PCA gap the boundary conditions of the problem have to be specified.

2.3 Equivalent Norton circuit in time domain

A Norton equivalent circuit representing the problem under investigation is shown in Fig. 2.2. The component representing the constitutive relation of equation (2.9)

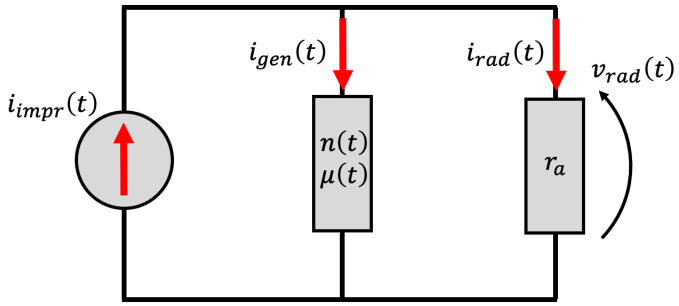

Figure 2.2: Norton equivalent circuit in time domain consisting in a current source, $i_{impr}(t)$, a component representing the excited PCA gap, $n(t), \mu(t)$, and a component representing the effect of the antenna radiation, r_a

appears here as a component in parallel with a load, representing instead the antenna response. The equivalent generator, $i_{impr}(t)$, is obtained using the constitutive relation of (2.9) with the constant voltage bias, V_b, applied at the antenna terminals. The current flowing in the impedance of the equivalent generator, $i_{gen}(t)$, is instead evaluated using (2.9) with the voltage drop across the load. These two currents are expressed as:

$$i_{impr}(t) = q_e \frac{W_y W_z}{W_x} \int_{-\infty}^{t} n_p(t, t'') \int_{t''}^{t} \mu(t - t') V_b dt' dt'' \tag{2.10a}$$

$$i_{gen}(t) = q_e \frac{W_y W_z}{W_x} \int_{-\infty}^{t} n_p(t, t'') \int_{t''}^{t} \mu(t - t') v_{rad}(t') dt' dt'' \tag{2.10b}$$

To properly represent the effect of the antenna in time domain, the impulse response of the architecture should be included. However, electrically long, broadband antennas have impulse responses can be approximated as Dirac's deltas, when one neglects late time reflections from the edges. For these configurations it is then legitimate to represent the load as a real radiation resistance, and the field radiated by the antenna as a voltage drop across the load. To solve the circuit leads to a system of two equations and two unknowns, $(i_{rad}(t), v_{rad}(t))$, that can be solved numerically:

$$i_{rad}(t) = q_e \frac{W_y W_z}{W_x} \int_{-\infty}^{t} n_p(t, t'') \int_{t''}^{t} \mu(t - t') \left(V_b - v_{rad}(t')\right) dt' dt'' \tag{2.11a}$$

$$v_{rad}(t) = i_{rad}(t) r_a \tag{2.11b}$$

For the sake of simplicity, the begin of the laser pulse is set at $t'' = 0$.

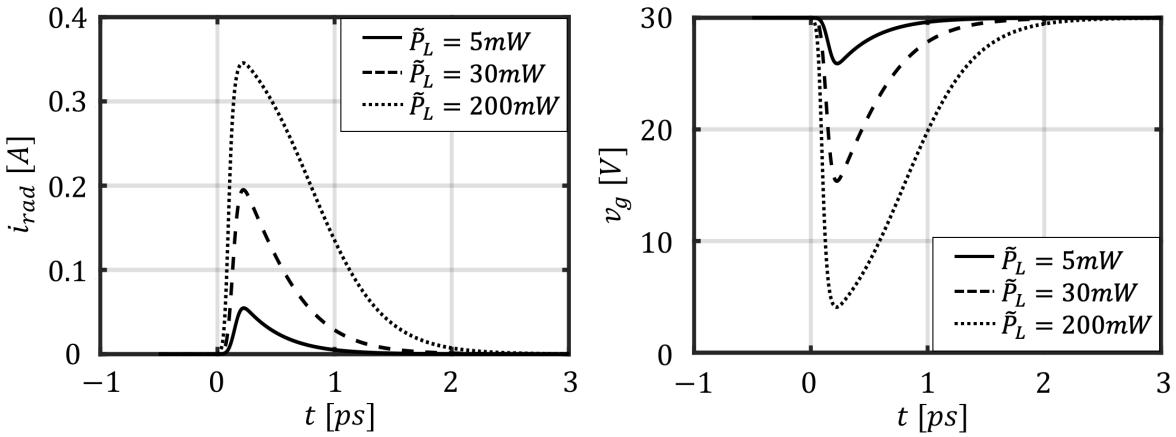

Figure 2.3: Temporal evolution of current, $i_{rad}(t)$, and voltage, $v_g(t)$, across the photoconductive gap for a bias voltage of $V_b = 30V$, a radiation resistance of $r_a = 75\Omega$, a scattering time of $\tau_s = 8.5fs$, an optical efficiency of $\eta_{opt} = 0.35$ and three different optical excitation $\tilde{P}_L$.

Fig. 2.3 shows the temporal evolution of the radiation current, $i_{rad}(t)$, and the PCA gap voltage, $v_g(t)$, predicted by the circuit for three different laser power levels arriving at $t'' = 0$, a bias of $V_b = 30V$, and an antenna radiation impedance of $r_a = 75\Omega$; the material and laser parameters are given in Table 2.1. The gap is assumed to be $W_x = W_y = 10\mu m, W_z = 2\mu m$, excited with an optical efficiency (discussed in Appendix A) of $\eta_{opt} = 0.35$. It is important to stress the fact that not only does a linear increase of the optical excitation not lead to a corresponding increase in amplitude, it also modifies the time signature of both the current and the voltage on the gap.

After having solved the circuit and calculated the induced photocurrent, the power radiated by the feed, r_a, is evaluated as:

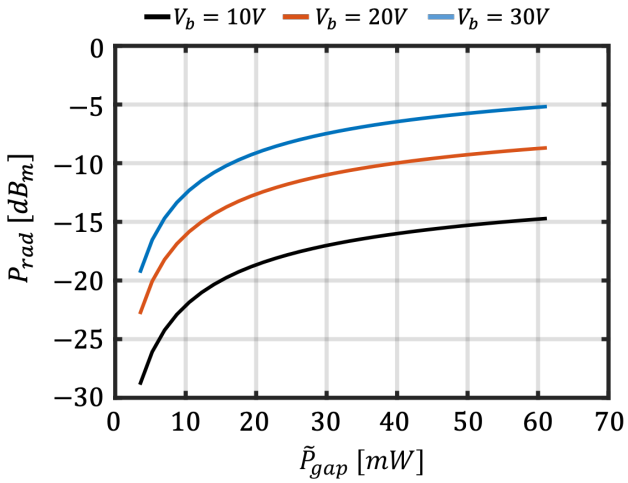

Figure 2.4: Power radiated by the load, r_a, as a function of the average laser power absorbed by the gap, $\tilde{P}_{gap} = \eta_{opt}\tilde{P}_L$, with $\eta_{opt} = 0.35$, for three different bias voltage, $V_b = 10, 20, 30V$.

$$P_{rad}(f) = \frac{2}{T_L}\int_0^{\infty} r_a \left|I_{rad}(f)\right|^2 df \tag{2.12}$$

Fig. 2.4 shows the power radiated by the feed, r_a, predicted by the equivalent circuit of Fig. 2.2 as a function of the average laser power absorbed by the gap, $\tilde{P}_{gap} = \eta_{opt}\tilde{P}_L$, for three different bias voltage, $V_b = 10, 20, 30V$. As discussed in Appendix A the ideal optical efficiency adopted to produce these results is $\eta_{opt} = 0.35$. The power radiated by the antenna saturates as one increases the optical excitation level: this is the mark of the radiation field screening caused by the generated radiation.

Appendix B presents a Thevenin equivalent circuit leading to the same system of equation in (2.11) that offers a different picture of the phenomena involved in the photocurrent generation.

2.4 Radiated power Vs antenna impedance

The radiation impedance of an antenna is in general a frequency domain entity composed of a real part, representing the power radiated in the far field region, and

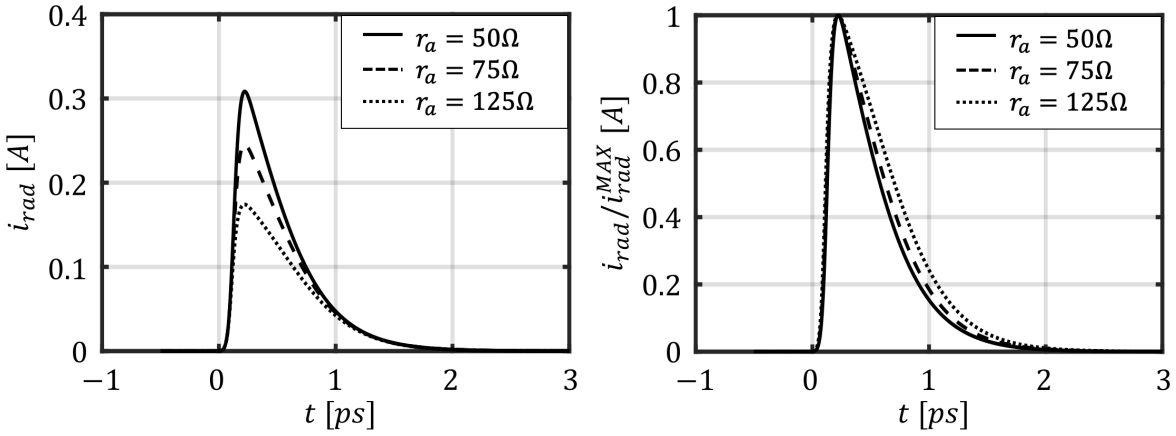

(a) (b)

Figure 2.5: Temporal evolution of the induced photocurrent, $i_{rad}(t)$, for three different different radiation resistance, $r_a = 50, 75, 125\Omega$. The current is obtained solving either one of the circuit of Fig. 2.2 and Fig. B.1 with a bias source of $V_b = 30V$, a scattering time of $\tau_s = 8.5fs$, an optical excitation of $\tilde{P}_L = 50mW$ and an optical efficiency of $\eta_{opt} = 0.35$.

an imaginary part, representing the reactive energy stored in the proximity of the device, $Z_a(f) = \Re[Z_a(f)] + j \cdot \Im[Z_a(f)]$. In case one wanted to translate the effect of the antenna radiation in time domain, an integral relation between the antenna impulse response and the voltage/current generator would have to be used. However, for broadband antennas, characterised by radiation impedances with approximately constant real parts much larger than the imaginary parts, $\Re[Z_a(f)] \gg \Im[Z_a(f)]$, the radiation impedance can approximated entirely as a resistance. This assumption greatly simplifies the evaluation of the current responsible for the radiation in equation (2.11).

The results of Fig. 2.3 and Fig. 2.4 are generated assuming a radiation resistance of $r_a = 75\Omega$, typical of broadband bow tie lens antennas printed over LT GaAs. Obviously, different antenna architectures present different radiation impedances, and different radiation impedances modify the behaviour of the photocurrent. Fig. 2.5 pictures the temporal evolution of the induced photocurrent, $i_{rad}(t)$, for three different different radiation resistance, $r_a = 50, 75, 125\Omega$. The current is obtained solving either one of the circuit of Fig. 2.2 and Fig. B.1 with a bias source of $V_b = 30V$, an optical excitation of $\tilde{P}_L = 50mW$. Fig. 2.5 (a) shows the actual $i_{rad}(t)$,

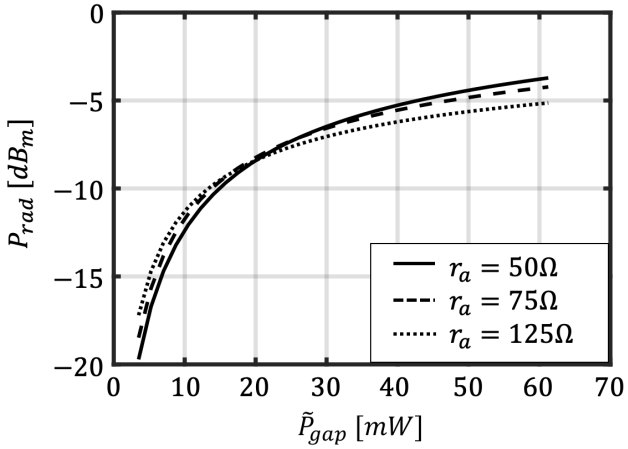

Figure 2.6: Power radiated by three different loads, $r_a = 50, 75, 125\Omega$, as a function of the average laser power absorbed by the gap, $\tilde{P}_{gap} = \eta_{opt}\tilde{P}_L$, with $\eta_{opt} = 0.35$, for a bias voltage $V_b = 30V$.

while Fig. 2.5 (b) plots its normalised envelope, to highlight the different behaviour caused by different radiation impedances.

A different behaviour of the induced photocurrent translates into different saturation behaviours of the power generated by the PCA. Fig. 2.6 shows the power radiated by three different feeds, $r_a = 50, 75, 125\Omega$, into the HR silicon lens as a function of the average laser power absorbed by the gap, $\tilde{P}_{gap} = \eta_{opt}\tilde{P}_L$, with $\eta_{opt} = 0.35$, for a bias voltage $V_b = 30V$. Lower values of r_a generate less THz power when excited with weak optical signals, but they approach saturation less rapidly, resulting in larger values of radiated THz power when excited with high optical signals. Different antennas can thus be adopted depending on the laser excitation in order to have the best possible signal to noise ratio.

Considerations about the antenna radiation pattern, the illumination of the lens and the coupling of the field after the lens with the quasi-optical path used to collect the radiation will be made later.

2.5 Radiated spectrum and power Vs carrier scattering time

The carrier scattering time in LT GaAs is a parameter that presents great variability. Indeed, the procedure to grow LT GaAs is not as standard as for other semiconductors, such as silicon, making its properties change considerably depending on where the wafers are manufactured, and what recipe is adopted. The range of values found in the literature is $\tau_s = 3 \rightarrow 180fs$.

It is apparent from the equations in (2.2) that the value of the scattering time directly changes the shape of the time domain mobility response function and, in turn, the behaviour of the velocity of the carrier; the velocity of the carrier is then further integrated in the calculation of the induced photocurrent, (2.9). Thus, not only does the choice of τ_s affect the amplitude of the current responsible for the radiation, (2.11), but it modifies its temporal evolution as well.

Fig. 2.7 pictures the temporal evolution of the induced photocurrent, $i_{rad}(t)$, for three different different scattering times, $\tau_s = 3, 8.5, 25fs$. The current is obtained solving either one of the circuit of Fig. B.1 and Fig. 2.2 with a bias source of $V_b = 30V$, an optical excitation of $\tilde{P}_L = 50mW$, and an antenna load of $r_a = 75\Omega$. Fig. 2.7 (a) shows the actual $i_{rad}(t)$, while Fig. 2.7 (b) plots its normalised envelope, to highlight the different behaviour caused by varying the scattering time.

Larger value of τ_s imply longer average times between electron-electron and electron-ion scattering events, and consequently larger time spans over which the carriers are accelerated by the field applied to the gap terminals. This results in an overall larger amplitude of the current, and a slower ending tails after the end of the optical pulse, effectively amplifying the low frequency portion of the spectrum. This is apparent from Fig. 2.8, showing the spectrum of the energy radiated by the feed, r_a, for three different different scattering times, $\tau_s = 3, 7.5, 25fs$. The energy radiated by the load is defined as:

$$E_{feed}(f) = r_a \left| I_{rad}(f) \right|^2 \tag{2.13}$$

Finally, Fig. 2.9 shows the power radiated by the feed into the HR silicon lens

as a function of the average laser power absorbed by the gap for three different scattering time: $\tau_s = 3, 8.5, 25fs$, with $\tilde{P}_{gap} = \eta_{opt}\tilde{P}_L$, $\eta_{opt} = 0.35$, and a bias voltage $V_b = 30V$. It is apparent that the amplification of the lower frequency portion of the radiated spectrum given by larger scattering times translates into larger values of radiated power, and a faster saturation under large optical excitations.

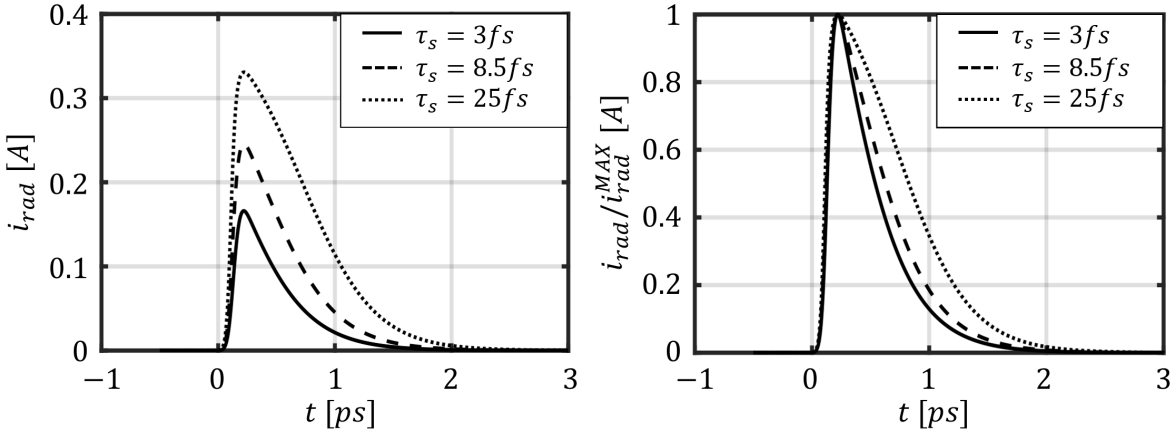

(a) (b)

Figure 2.7: Temporal evolution of the induced photocurrent, $i_{rad}(t)$, for three different different scattering times, $\tau_s = 3, 8.5, 25fs$. The current is obtained solving either one of the circuit of Fig. 2.2 and Fig. B.1 with a bias source of $V_b = 30V$, an optical excitation of $\tilde{P}_L = 50mW$, with $\eta_{opt} = 0.35$, and an antenna load of $r_a = 75\Omega$.

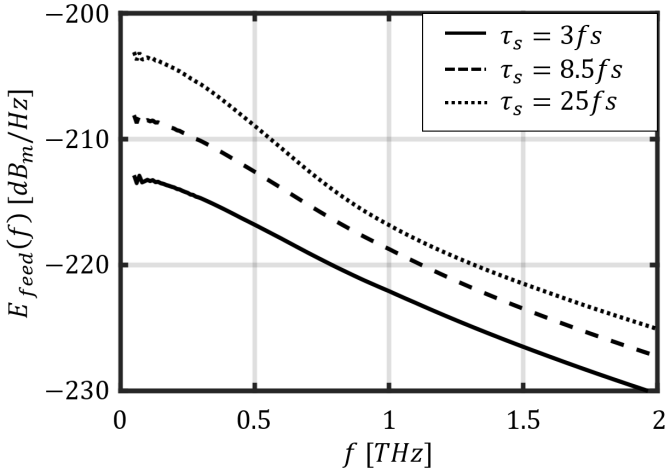

Figure 2.8: Spectrum of the energy radiated by the feed for three different different scattering times, $\tau_s = 3, 8.5, 25fs$. The current is obtained solving either one of the circuit of Fig. B.1 and Fig. 2.2 with a bias source of $V_b = 30V$, an optical excitation of $\tilde{P}_L = 50mW$, with $\eta_{opt} = 0.35$, and an antenna load of $r_a = 75\Omega$.

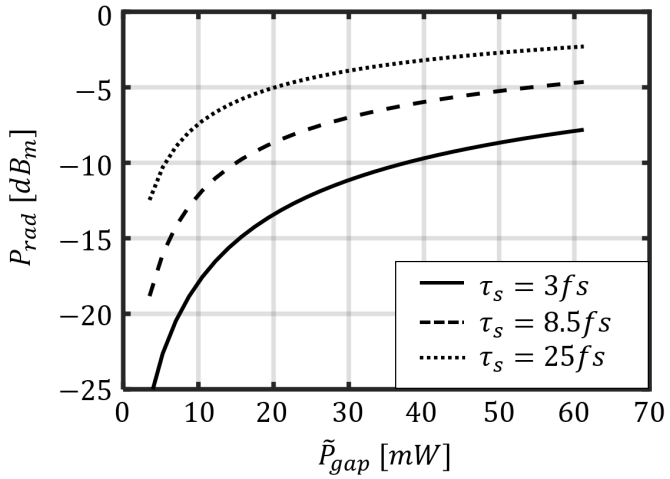

Figure 2.9: Power radiated by the feed, $r_a = 75\Omega$, into the HR silicon lens as a function of the average laser power absorbed by the gap for three different scattering time: $\tau_s = 3, 8.5, 25fs$, with $\tilde{P}_{gap} = \eta_{opt}\tilde{P}_L$, $\eta_{opt} = 0.35$, and a bias voltage $V_b = 30V$.

Chapter 3

Characterisation of bow tie photoconductive lens antennas

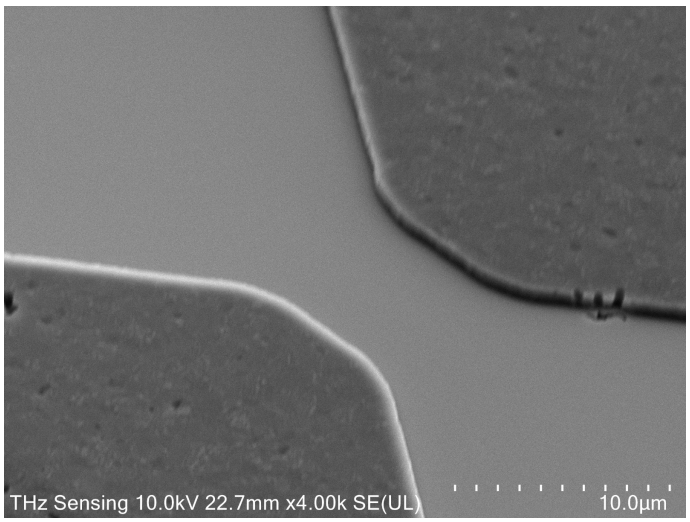

Figure 3.1: Picture acquired with a scanning electron microscope of the front side of the leaky wave lens antenna. One can see the metallisation pattern and the gap onto which the laser is shone, found at the opposite side of the HR Si Lens.

In order to assess the validity of the model presented in this thesis a campaign of measurements is undertaken to characterise a photoconductive antenna with a slotted bow-tie geometry, same device that with partial success was investigated in [29]. The campaign is carried out in the Time Domain Laboratory of the Tera-Hertz

Sensing Group, TU Delft.

3.1 Photoconductive antenna design

The bow tie antenna under test consists of a metallization printed over a substrate of photoconductive material, namely low-temperature grown Gallium Arsenide (LT GaAs), radiating into a HR silicon lens. Fig. 3.2 (a) depicts the layer structure of the chip. Starting from the side of the metallization, one finds $2\mu m$ of LT-GaAs, $400nm$ of AlGaAs with 0.75% aluminium content, $400nm$ of GaAs buffer, a $525\mu m$ thick SI-GaAs wafer. Fig. 3.1 shows a picture of the lens antenna from the metallisation side. The metallisation pattern of the antenna follows a bow tie geometry, Fig. 3.2 (b), with $45°$ taper angle and a square gap of $W_x = W_y = 10\mu m$. A hemispherical silicon lens with radius $R_{lens} = 10mm$ and extension length $E_{lens} = 0.29R_{lens}$ is placed on top of the bow tie slot. The lens is coated with a quarter-wavelength matching layer (at frequency 0.4THz) in order to reduce the reflection at the lens-air interface. This matching layer is made with a $114\mu m$ thick parylene-c coating with a relative permittivity of 2.72 [35]. More details about the design, fabrication and assembly of this device are thoroughly detailed in [29]. The material properties are included in Table 2.1.

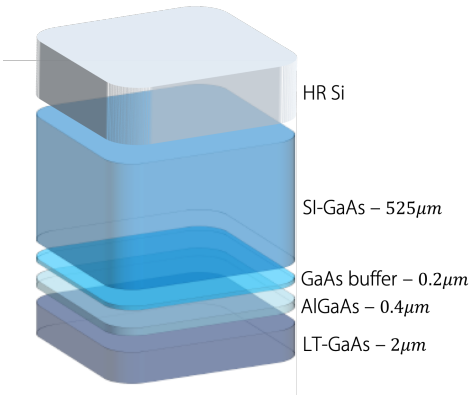

(a)

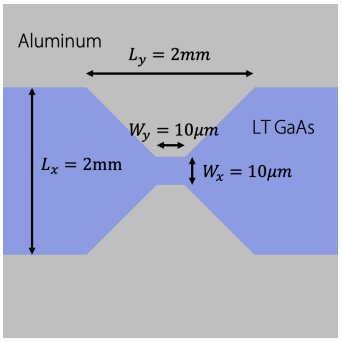

(b)

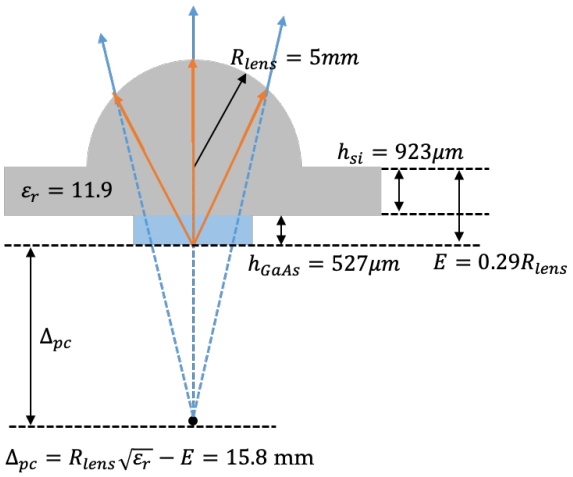

(c)

Figure 3.2: Details of the antenna under test. (a) The dielectric stratification adopted for the device; the antenna is printed at the bottom side of the LT GaAs membrane; (b) the metallization bow tie geometry printed over the photoconductor with a taper angle of $90°$; (c) the geometry of the hemispherical lens placed on top of the LT GaAs membrane.

3.2 Experimental setup

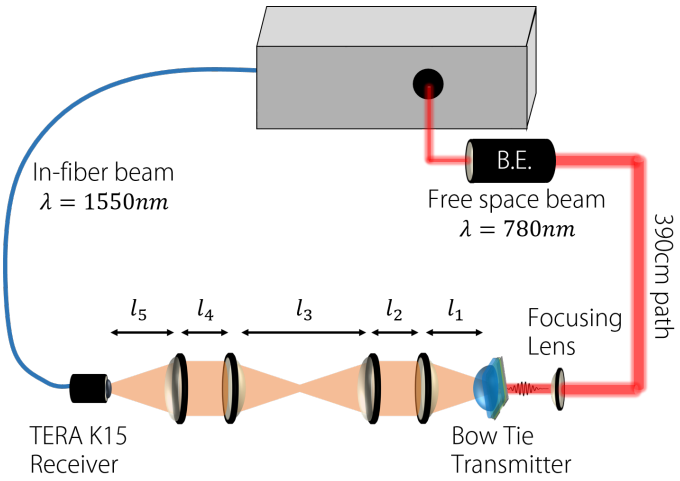

(a)

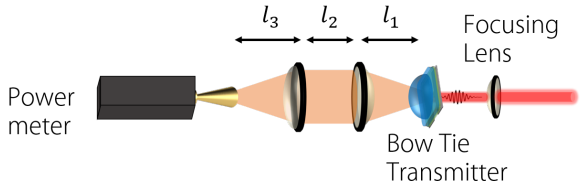

(b)

Figure 3.3: Schematic of the measurement setup: the transmitting PCA (Bow Tie under investigation) is excited by the free space laser. (a) Spectrum acquisition: the receiver is the native Auston switch lens antenna adopted by the TERA K15 from Menlo Systems G,bH. The free-space delay line of 390cm ensures the synchronisation of the two devices. The quasi optical path consists of 4 identical plano-convex polymer lenses, its dimensions are $l_1 = 20mm, l_2 = 100mm, l_3 = 90mm, l_4 = 100mm, l_5 = 25mm$. (b) Power acquisition: the receiver is a power meter coupled to a multi-mode horn antenna via 2 identical plano-convex polymer lenses, its dimensions are $l_1 = 35mm, l_2 = 60mm, l_3 = 20mm$

The setup adopted for the measurements is shown in Fig. 3.3. The setup is used for the acquisition of spectrum and power radiated by the PCA: the spectrum is measured using the whole setup, Fig. 3.3 (a); while the power is measured using the modified version in Fig. 3.3 (b) with a power meter collecting the radiation at the intermediate focus of Fig. 3.3. The TDSS system adopted for the campaign

is commercially available at Menlo Systems GmbH (TERA K15), [36], with ad hoc modifications. Specifically, the in-fibre fed transmitter of the TERA K15 is replaced by the bow tie under investigation, which is instead fed by the free space optical delay line shown in Fig. 3.3. The TX PCA is biased to a fixed voltage, V_b, which accelerates the photocarriers injected by the free space laser source, operating at 780nm.

The receiver's (RX) lens antenna in the spectrum measurement setup of Fig 3.3 (a) is the native Auston switch adopted by the TERA K15, fed instead by in-fibre optical pulses, operating at 1550nm. Both in-fibre and optical excitations are pulsed at $f_L = 80MHz$. The free photo-carriers injected in the RX PCA are accelerated by the THz field incoming from the transmitter. The synchronisation between the TX PCA and the receiver is achieved through a 390cm optical delay path, such that the receiver is excited by the in-fibre laser when the field radiated by the TX PCA impinges on it. An actual picture taken from the top of the setup in Fig. 3.3 (a) is shown in Fig. 3.4.

Finally, the photocurrent induced in the receiver is sent to a trans-impedance amplifier and processed by the read-out electronics. The temporal evolution of the THz pulse is recovered through a stroboscopic sampling technique, where the reciprocal delay between the two laser sources is modulated by an optical delay unit (ODU) controlled electronically. The laser sources, the read-out electronics as well as the ODU are part of the TERA K15.

The THz pulse radiated with the transmitter is characterised in three steps:

- the laser beam exciting the bow tie is profiled on the plane where the antenna will be placed.
- the power radiated by the bow tie under test is collected using a power meter (Virginia Diodes, PM5, [37]) using the setup sketched in Fig. 3.3 (b). The coupling losses introduced by the channel are discussed in Section 3.4.
- the pulse emitted by the bow tie PCA is coupled to the Auston switch of the TERA K15 to acquire its temporal evolution and frequency behaviour.

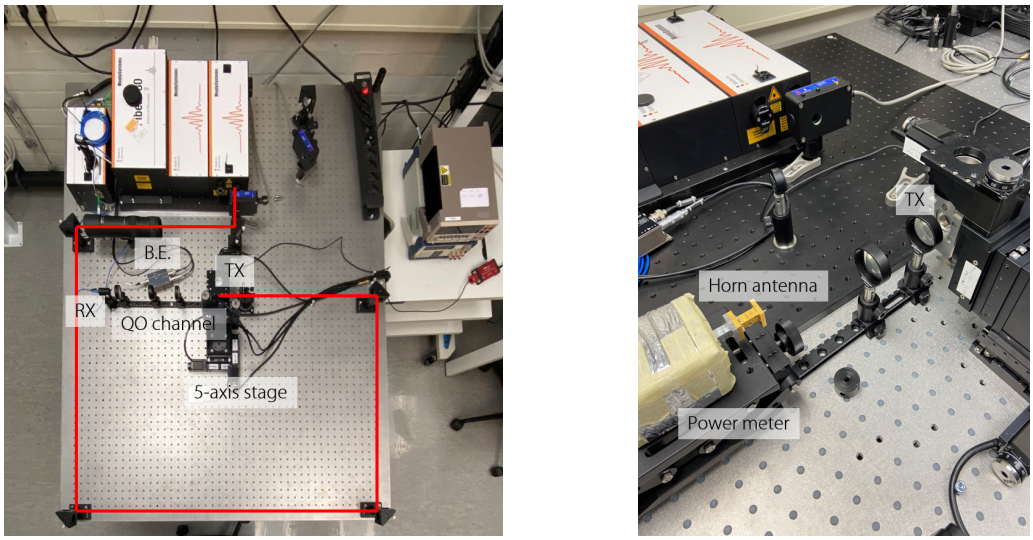

(a) (b)

Figure 3.4: Pictures of the measurement setup. (a) Top view of the setup depicted in Fig. 3.3 (a). The red line shows the laser delay line, leaving the TERA K15 and arriving to the antenna, placed in a holder controlled by a 5-axis motorised stage, as described in section 3.3. One can also see the beam expander, the TX PCA, the RX lens antenna, and the QO channel that couples them. (b) view of the setup in Fig. 3.3 (b)

3.3 Optical path and focused laser beam

The 390cm of Fig. 3.3 optical path is achieved through 5 flat protected-gold mirrors (ThorLabs, PF05-03-M01), a beam expander (ThorLabs, BE02-05-B) and a focusing lens (ThorLabs, LA4725-B-ML) [38]. The two THz lens antennas are coupled by a quasi-optical path consisting of 4 identical plano-convex polymer lenses (ThorLabs, TPX50) that collect the TX radiation and guide it to the RX PCA.

The laser delay line is built as follows: the pulse has a Gaussian temporal profile with a full width at half maximum of $\tau_p = 100fs$, and a repetition rate of $T_L = 12.5ns$ $(f_L = 80MHz)$; the power available from the free-space output at 780nm ranges from $\tilde{P}_L = 1 \rightarrow 240mW$.

The beam emerges with a $1/e$ waist of $w_0 = 0.6mm$, and needs to be focused down to a waist of $w_L = 8.5\mu m$ (which corresponds to a -3dB radius of $R_L = 5mm$, or diameter of $D_L = 2R_L = 10mm$) to match the PCA gap lateral dimensions

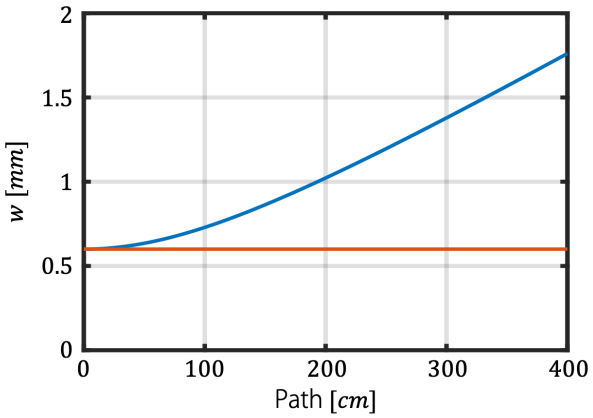

Figure 3.5: Divergence of the laser beam waist as a function of the distance (solid blue line); the red solid line represent the waist at its source, $w_0 = 0.6mm$. The propagation of the beam is calculated using the well known expression $w(x) = w_0\sqrt{1 + \left(\frac{\lambda x}{\pi w_0^2}\right)^2}$, where x is the length of the optical path.

$W_x = W_y = 10\mu m$, ideally.

To avoid the divergence of the beam over the 390cm optical path, plotted in Fig. 3.5 a beam expander with a factor 5X magnification is placed at the beginning of the delay line. The lens focusing the optical beam onto the antenna gap is a fused silica plano-convex lens with a diameter of 25.4mm and a focal length of 75mm.

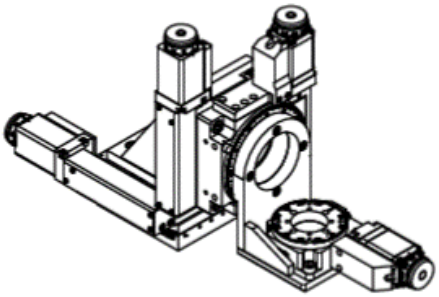

Figure 3.6: Drawing of the 5-axis (3 translational and 2 rotational axes) stage adopted to control the blades and the TX PCA.

To verify the laser spot and the alignment, the focused beam is profiled on both the horizontal and vertical axes using two metal blades and the knife-edge tech-

nique [39]. The blades are placed in a holder controlled by a 5-axis (3 translational and 2 rotational axes) motorised stage with a translational resolution of $1.25\mu m$ and a rotational resolution of $0.01°$; a drawing of the stage is showed in Fig. 3.6. The stage is computerised and controlled by an *ad-hoc* software developed in-house. The holder of the blade is the same one used for the antenna, thus ensuring that the measured profile is eventually the same exciting the investigated PCA.

The results are showed in Fig. 3.7. The measured spill-over efficiency is $\eta_{SO}^{y} = 0.58$ on the vertical axis, and $\eta_{SO}^{y} = 0.59$ on the horizontal axis. The ideal value that guarantees an almost uniform optical distribution on the gap is $\eta_{SO}^{id} = 0.58$. The average of the spill-over efficiency over the two axes is used to extract the optical efficiency: it results $\eta_{opt} = 0.35$.

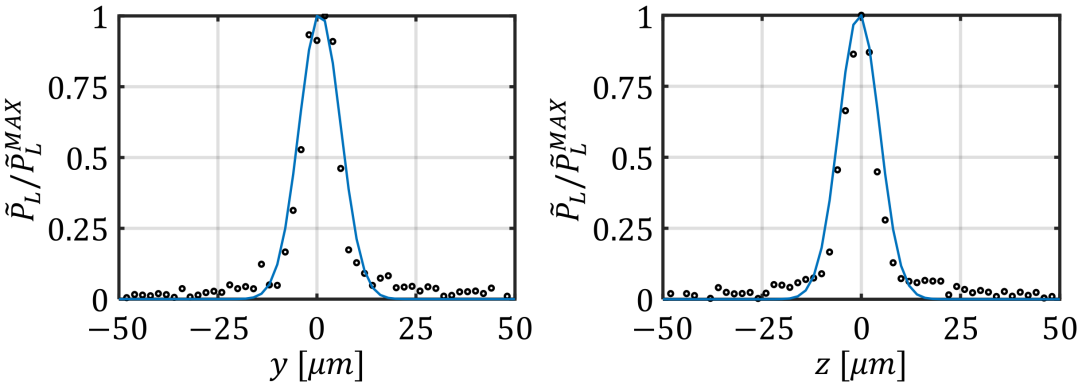

(a) profile on the vertical axis

(b) profile on the horizontal axis

Figure 3.7: Profile of the focused optical beam obtained with the setup in Fig. 3.3 along the vertical (y) and horizontal (z) axis, respectively. The solid blue line is a Gaussian fit to verify the gaussicity of the focused beam. The -3dB diameter of the beam along the y axis is $D_L^y = 10.2\mu m$, on the z axis it is $D_L^z = 9.5\mu m$.

After the losses introduced by the mirrors, the beam expander and the focusing lens along the optical delay line of 390cm the maximum power reaching the device is 180mW, instead of 240mW.

3.4 Detected THz power

Once the desired optical beam profile on the focal plane is achieved, the blades are replaced with the target TX PCA. The holder of the antenna is identical to that used for the blades, thus ensuring that the gap of the PCA is excited by the measured beam profile; however, due to tolerances in the manufacturing of the holders, it was necessary to fine tune the device position in order to achieve the optimal illumination. The fine tuning is performed by biasing the antenna and measuring the DC current induced in the gap excited by the laser, maximising it with micrometrical position adjustments controlled by the 5-axis stage. Fig. 3.8 shows the value of the measured DC current as a function of the laser average power absorbed in the gap ($\tilde{P}_{gap} = \eta_{opt}\tilde{P}_L, \eta_{opt} = 0.35$) with the PCA at the optimised position.

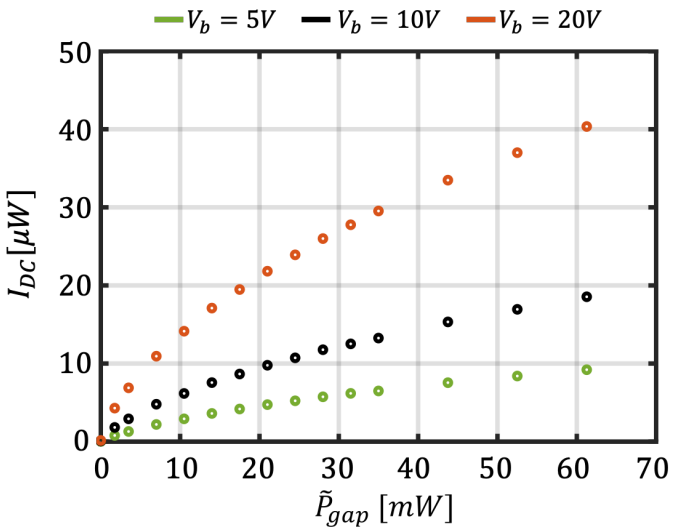

Figure 3.8: Measured DC current with the beam obtained in Fig. 3.7 as a function of the laser power absorbed in the gap ($\tilde{P}_{gap} = \eta_{opt}\tilde{P}_L, \eta_{opt} = 0.35$) for three bias points: $V_b = 5, 10, 20V$.

Before detecting the power radiated by the PCA, the position of the two lenses and the horn of the quasi-optical path are fine-tuned until the maximum power is received by the power meter. The final configuration is detailed in Fig. 3.3 (b). The power radiated by the photoconductive antenna is then characterised as a

function of the optical power. The chip is biased to a voltage potential which is parametrically varied: $V_b = 10, 20, 30V$. The THz radiated power is collected with a power meter (Virginia Diodes, PM5, [37]), coupled to the antenna through a quasi-optical path consisting of two plano-convex polymer lenses (ThorLabs, TPX50) and a receiving conical horn antenna (Virginia Diodes, conical horn antenna CH-WR10). The set-up is depicted in Fig. 3.3 (b).

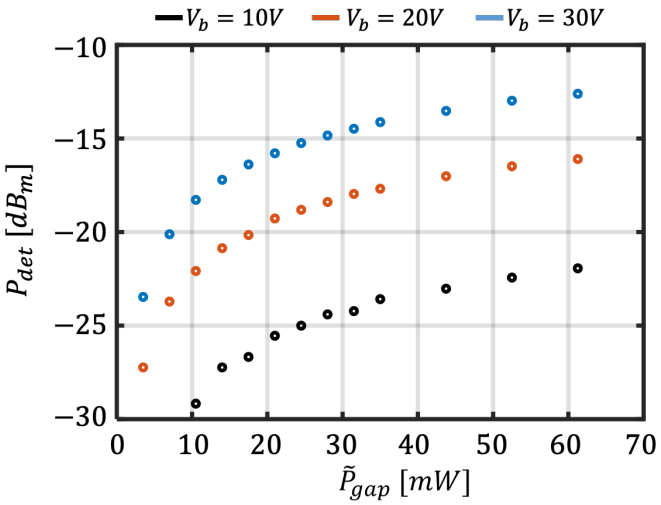

Figure 3.9: Detected THz power for three different bias levels, $V_b = 10, 20, 30V$, as a function of the optical power absorbed in the PCA gap, $\tilde{P}_{gap} = \eta_{opt}\tilde{P}_L, \eta_{opt} = 0.35$. Note the saturation in the output power emerging under larger and larger optical excitations.

Fig. 3.9 shows the THz power read by the power meter sketched in Fig. 3.3 (b), P_{det}, as a function of the laser power absorbed in the gap of the device ($\tilde{P}_{gap} = \eta_{opt}\tilde{P}_L, \eta_{opt} = 0.35$) for the three different bias points: $V_b = 10, 20, 30V$.

As expected, the increase of the average power of the pulsed laser does not simply lead to a quadratic increase of the THz power, as one might expect. For larger optical excitations, the saturation effect becomes manifest.

3.4.1 Comparison between simulations and measurements

In this section the measurements are compared against the prediction of the model introduced in Chapter 2. In order to do so, one needs to estimate the current in eq. (2.11), as well as simulate the antenna radiation properties and the coupling

between the TX PCA and the receiving horn connected to the power meter for the setup in Fig. 3.3 (b). First, the average power radiated by the antenna is calculated as:

$$P_{rad} = \frac{2}{T_L} \int_0^{\infty} \Re\left[Z_a(f)\right] \left|I_{rad}(f)\right|^2 \eta_{QO,tot}(f) df \tag{3.1}$$

where the integration is performed with unilateral spectra. The current, $i_{rad}(t)$, from equation (2.11) is evaluated with the time-domain either equivalent circuit of Fig. B.1 or Fig. 2.2. The parameters of the substrate of LT GaAs, except for the scattering time τ_s which is unknown, and of the laser are listed in Table 2.1. The amplitude of the optical excitation, equation (2.4), is calculated using the measured -3dB beam diameter of Fig. 3.7.

The antenna radiation impedance, $Z_a(f)$, is simulated as a function of the frequency using a full-wave EM software, CST [40]. The impedance is shown in Fig. 3.10.

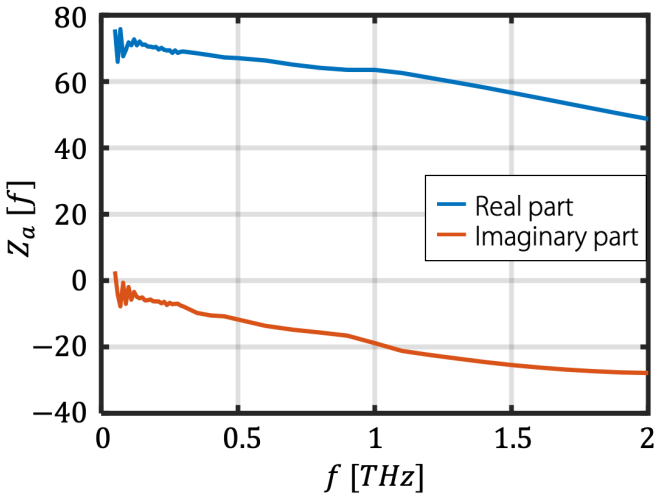

Figure 3.10: Radiation impedance of the antenna under test simulated with CST

From Fig. 2.8 one sees that the PCA radiates higher energy in the low frequency portion of the spectrum: most of the radiated power is contained in the band from 100GHz to 500GHz. The power meter and the QO channel coupling, on the other hand, introduce a cut off at 75GHz, as shown in Fig. 3.11. Furthermore, the

PCA radiation impedance in Fig. 3.10 exhibits a real part which is significantly larger than the imaginary part. For these reasons the impedance is approximated as a constant resistance, $Z_a(f) \simeq 75\Omega$. This radiation resistance is used to solve the circuit and calculate the induced photocurrent in eq. (2.11), $i_{rad}(t)$, and its Fourier transform as: $I_{rad}(f) = \mathscr{F}[i_{rad}(t)]$. To approximate the radiation impedance of an antenna as a simple resistance is an assumption that can be justified only in broad-band antennas, such as the bow tie PCA under analysis; if this condition is not met, the proper temporal impulse response of the antenna should be calculated in order to have a good estimation of its behaviour.

Fig. 3.11 shows the efficiency of the quasi-optical channel coupling the TX PCA to the horn connected to the power meter; the definition and evaluation of the QO channel efficiency follows a similar procedure than what reported in [21]. The dimensions, detailed in Fig. 3.3 (b) are found maximising the received power during its acquisition. The losses introduced by quasi-optical channel are evaluated through both measurements and simulations resorting to an in-house tool [41] alongside an EM modelling software, Ticra GRASP [42]; the PCA beam pattern has been computed and imported from CST. Fig. 3.11 (a) shows the coupling efficiency, $\eta_{QO}(f)$; Fig. 3.11 (b) the ohmic losses introduced by the polymer lenses guiding the THz radiation, $\eta_{TPX}(f)$; Fig. 3.11 (c) the total losses of the QO channel, $\eta_{QO,tot}(f) = P_{det}(f)/P_{rad}(f)$, as a function of the frequency. $\eta_{QO}(f)$ is estimated with in-house tool and Ticra GRASP; $\eta_{TPX}(f)$ is estimated for a plane wave propagating and using the $tan(\delta)$ given by measurements performed at Menlo Systems, GmbH laboratories; $\eta_{QO,tot}(f)$ is the result of the product of the former two, $\eta_{QO,tot}(f) = \eta_{QO}(f) \cdot \eta_{TPX}(f)$.

The frequency oscillation of Fig. 3.11 (a) is the result of the adoption of a single matching layer that is tuned to maximise the efficiency at 400GHz and multiples. Instead, the largest losses are associated to the spill over in the conical horn: indeed, the horn is much more directive than the lens antenna, and as a consequence the quasi optical efficiency remains limited. Finally, the cut-off introduced by the waveguide of the power meter is at 75GHz. The quasi optical efficiency is complemented with the dielectric losses in the lenses, to obtain the total efficiency, $\eta_{QO,tot}$, as show in Fig 3.11.

Fig. 3.12 shows the THz power captured with the power meter as a function

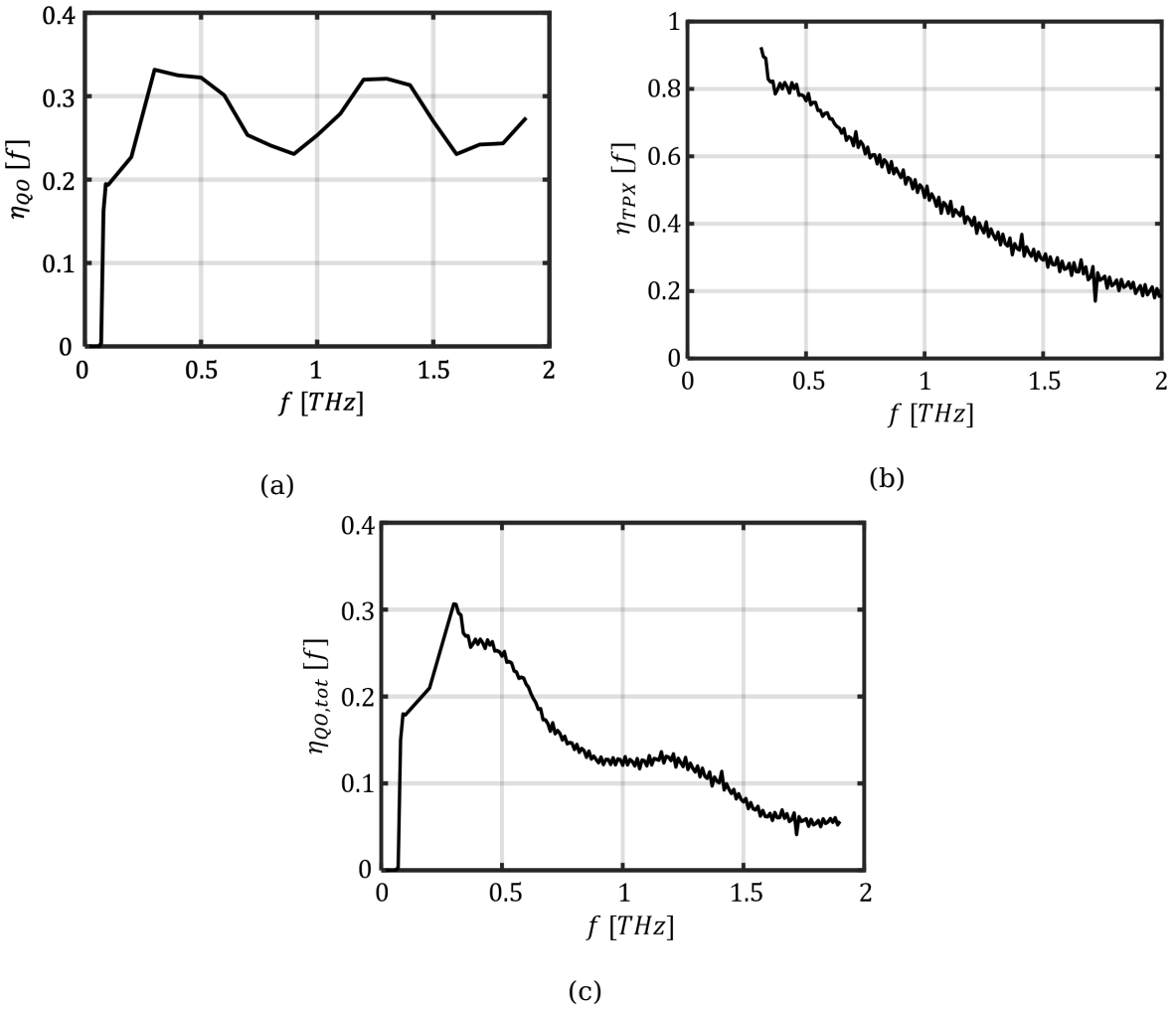

Figure 3.11: Quasi-optical efficiency describing the losses in the measurement setup in Fig. 3.3 (b). (a) Radiation coupling losses between TX PCA and the horn connected to the power meter, (b) Ohmic losses introduced by the TPX lenses, (c) Total losses of the system, given by the product of the former two.

of the average optical power absorbed by the gap of the device for 3 different bias levels, $V_b = 10, 20, 30V$; the measurements are compared to the corresponding simulations. The dots represent the measured data point, while the solid line represents the predictions of the model.

Table 2.1 shows all the parameters adopted, except for the carrier scattering

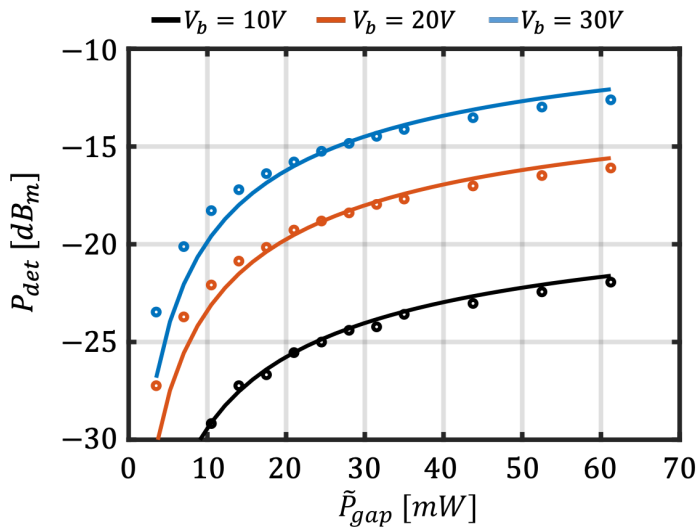

Figure 3.12: Power detected by the power meter evaluated using the methodology presented in this thesis opposed to the acquired measurements for three different bias levels, $V_b = 10, 20, 30V$, as a function of the optical power absorbed by the gap of the PCA ($\tilde{P}_{gap} = \eta_{opt}\tilde{P}_L, \eta_{opt} = 0.35$). The dots represent the measured data point, while the solid line represents the predictions of the model.

time, which is unknown. In line with values found in the literature [18], a scattering time of $\tau_s = 8.5fs$ is chosen to achieve the best match: the agreement is exceptional, and the differences between the data predicted by the model presented here and the measurement lie within only 1dB. The saturation effect occurring at large optical power levels emerging from the measured data is predicted by the model with great accuracy.

The saturation of the THz power radiated by the PCA is the consequence of a reduction of the total field applied over the gap caused by the radiation itself, as in equation (2.10). This acts as a feedback limiting the maximum photocurrent that can be induced in the device feedback from the antenna: the larger the average laser power shone onto the device, the stronger the radiation and the stronger the drop over the gap potential, until the amplitude of the radiation equals the bias level effectively short-circuiting the gap, $v_g(t) \to 0$.

Adopting a Thevenin circuit representation, as in Fig. B.1, one can ascribe the saturation to the screening induced over the gap by the field radiated by the PCA.

On the contrary, adopting a Norton circuit representation, as in Fig. 2.2, one can ascribe the saturation to the gap load shorting the radiation load.

3.4.2 Effect of the QO channel

This subsection highlights the effect on the detected power caused by the coupling between the TX PCA and the horn connected to the power meter, together with the ohmic losses in the polymer lenses. The adopted QO channel, sketched and detailed in Fig. 3.3, belongs to the TERA K15 by Menlo Systems GmbH, and is a solution often used by other commercial TDSS: the only difference lies in that now the TX PCA is not the native Auston switch, but the bow tie PCA analysed in this chapter.

Fig. 3.13 shows the effect of the losses of the QO path in Fig. 3.11. The comparison is done by plotting the power radiated versus the power detected from the bow tie PCA as predicted by the model presented in Chapter 2 for two bias voltage points. The solid line represents the detected power, while the dotted line represents the radiated power (obtained setting $\eta_{QO,tot}(f) = 1$ in eq. (3.1)).

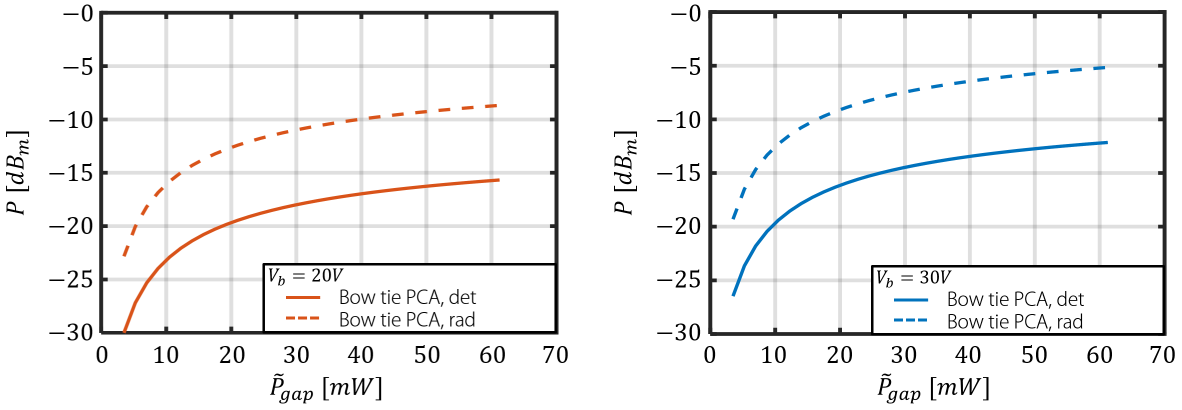

(a) (b)

Figure 3.13: Effect of the QO channel, *i.e.* Fig. 3.11: comparison between the power radiated (dotted line) and detected (solid line) from the bow tie PCA as predicted by the model of Chapter 2.

3.5 Time domain pulse and spectral response

After having coupled the bow tie PCA under test with the RX Auston switch of the TERA K15, the time domain pulse is acquired via the complete setup of Fig. 3.3; then, the spectral response is derived from the Fourier transform of the pulse. It is apparent that the temporal envelope of the received pulse is affected by both the TX PCA and the RX PCA affect, as well as the QO channel that couples the two.

One should bear in mind that the radiation patterns of the Auston switch and the bow tie are significantly different, as showed in Fig 1.3 and 1.4 in Chapter 1. Moreover, the radiation pattern of the Auston switch is frequency dependent. Finally, the Auston switch is a heavily polarisation sensitive architecture, thus to rotate either one of the two antennas greatly affects amplitude and shape of the received pulse. For these reasons, the coupling efficiency between TX and RX PCA cannot but remain poor. In the acquisition of the pulse, the relative position between the Auston switch and the bow tie is optimised to obtain the highest possible amplitude.

Fig. 3.14 shows the THz pulses received by the RX module of the TERA K15 with the TX PCA biased at $V_b = 30V$ and excited by different optical pulses exciting the TX PCA ranging $\tilde{P}_L = 20 \rightarrow 180mW$. In order to know the optical power absorbed in the TX PCA it is sufficient to multiply the total laser power times the optical efficiency, $\eta_{opt} = 0.35$

The received signals in Fig. 3.14 are in arbitrary units since the receivers are not absolutely calibrated. However, the relative differences are of interest. Stronger responses are clearly visible for stronger optical excitations, and it is apparent that to vary the laser power alters the temporal evolution of the received signal, which will in turn affect its frequency behaviour.

Also plotted is the pulse received using the TERA K15 original link: the system uses two Auston switches with different gap dimensions in a polarisation matched configuration; for the details refer to [36].

The corresponding spectra, also in arbitrary units, are evaluated performing the Fourier transforms of the signals of Fig. 3.14 and are shown in Fig. 3.15.

As apparent from Fig. 1.3 and 1.4, the radiation patterns of bow tie and Auston switch PCAs are vastly different. This makes the coupling between the

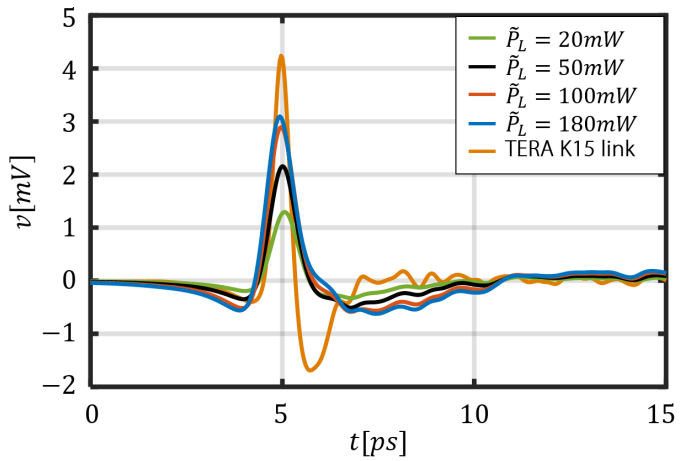

Figure 3.14: Measured time domain pulses radiated by the bow tie under investigation and collected by the receiver native of the TERA K15: the TX antenna is biased at $V_b = 30V$ and excited by different levels of optical power, $\tilde{P}_L = 20, 50, 100, 180mW$. Also plotted is the pulse detected using the TERA K15 native link.

two antennas rather poor. Moreover, the matching is further complicated by the frequency dependent behaviour of the Auston switch radiation pattern. Finally, at frequencies below 250GHz, the bias lines feeding the Auston switch radiate instead of the gap itself, heavily worsening its pattern, [22]. For all of these reasons it is difficult to make considerations on the relative power emitted by the two devices.

The spectra detected using the bow tie PCA as a transmitter present stable behaviours, with sharp absorption lines given by the water content in the air. The strong oscillations observable at very low frequencies are induced by the TX antenna, which does not radiate efficiently below 100GHz. Moreover, the low frequency portion of the spectra is heavily affected by the response of RX Auston switch used by the TERA K15, whose spectral signature presents a maximum around 400GHz and is not efficient for frequencies lower than 250GHz. A careful observation of the curves shows that for higher optical excitations, the largest increases in power occur at the lower frequencies, while only moderate enhancements emerge for the higher spectral components. Finally, for low power optical excitation the dynamic range of the signal received is too close to the noise floor to appreciate this behaviour.

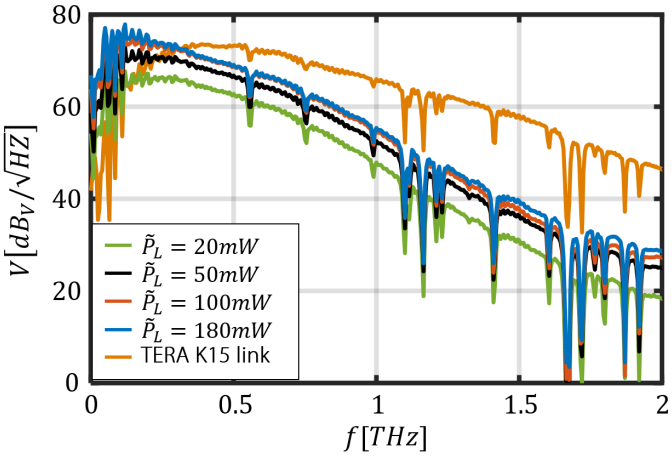

Figure 3.15: Spectra of the measured time domain pulses radiated by the bow tie under investigation and collected by the receiver native of the TERA K15: the TX antenna is biased at $V_b = 30V$ and excited by different levels of optical power, $\tilde{P}_L = 20, 50, 100, 180mW$. Also plotted is the spectrum of the pulse detected using the TERA K15 native link.

Fig. 3.16 shows the spectra of the energy radiated by the bow tie feed under investigation into the silicon lens predicted by the model introduced in this thesis, as:

$$E_{feed}(f) = \Re\left[Z_a(f)\right] |I_{rad}(f)|^2 \tag{3.2}$$

One should realise that these spectra do not account for the optical path or the lens radiation efficiency. An increase of laser power, clearly corresponds to higher overall energy spectra. However, the most significant enhancement of energy is predicted at the lower frequency portion of the spectrum, rather than at the higher.

Fig. 3.17 compares measurements and simulations focusing on the difference between normalised spectra at high ($\tilde{P}_L = 180mW$) and low ($\tilde{P}_L = 20mW$) laser power. The normalisation of both spectra is at 50GHz. Specifically, the measurement curve (solid line) is extracted as:

$$\frac{E^{meas}_{feed}(\tilde{P}_L = 20mW)}{E^{meas}_{50GHz}(\tilde{P}_L = 20mW)} - \frac{E^{meas}_{feed}(\tilde{P}_L = 180mW)}{E^{meas}_{50GHz}(\tilde{P}_L = 180mW)} \tag{3.3}$$

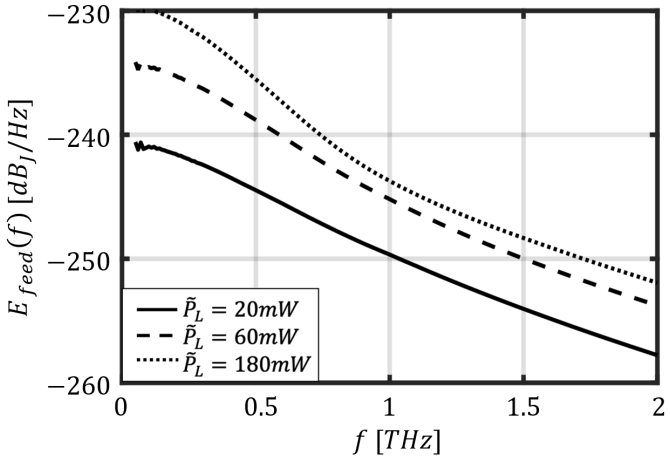

Figure 3.16: Energy spectra radiated by the feed into the silicon lens antenna evaluated using the methodology presented in this paper. The curves refer to three different optical excitations, $\tilde{P}_L = 20, 60, 180mW$.

corresponding to the spectra of 3.15. Instead, the simulation curve (dashed line) is evaluated as:

$$\frac{E_{feed}(\tilde{P}_L = 20mW)}{E_{50GHz}(\tilde{P}_L = 20mW)} - \frac{E_{feed}(\tilde{P}_L = 180mW)}{E_{50GHz}(\tilde{P}_L = 180mW)} \tag{3.4}$$

where the spectra are calculated using equation (3.2).

As expected the higher frequency components due to lower optical powers appear larger in both simulations and measurements. The fact that the tendency is similar in simulations and measurements can be interpreted as comforting. In fact the circuit model predicts well the that there will be comparatively less power at high frequencies when exciting the structure with more optical power. In commenting Fig. 3.17 one should recall that the antenna impulse response was assumed instantaneous in the derivation of the time domain current, eq. (2.11), and that the received signal are heavily affected by the poorer efficiency of the Auston switch for frequencies lower than 250GHz. At higher frequencies the

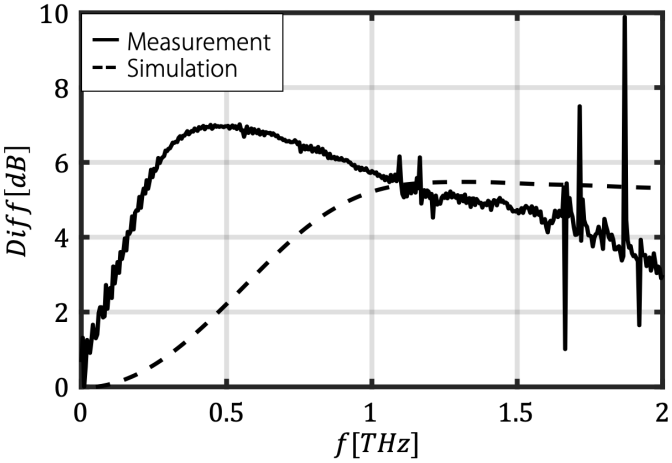

Figure 3.17: Comparison between measurements and predictions of the model focusing on the difference between normalised spectra at high ($\tilde{P}_L = 180mW$) and low ($\tilde{P}_L = 20mW$) laser power. The normalisation of both spectra is at 50GHz.

predictions and the measurements tend to agree up to 2THz, when the measured signal approaches the noise floor of the system.

3.6 Conclusions

The procedure introduced in Chapter 2 and hereby validated stems from semiconductor physics to assess the behaviour of the injected photocarriers rigorously, it proceeds building an equivalent circuit in time domain solved following a stepped time evolution, it calculates the photocurrent flowing across the antenna gap, and translates it into the frequency domain performing its Fourier transform. The antenna radiation impedance, its beam pattern, and the quasi-optical channel efficiency are simulated resorting to in house tools combined with commercially available EM modelling software. Once the main parameters characterising the photoconductor and the optical excitation are known, the theory proves to be an efficient tool to obtain a fast and precise evaluation of the temporal evolution of the field across the gap, the induced photocurrent and its spectrum, and the power radiated with the THz beam of broad band photo-conductive antenna excited by pulsed lasers. The saturation of the radiated power observed under large optical

excitations as predicted by the model shows an excellent agreement with the measurements.

If an even more accurate evaluation of the time evolution of the current signal and its spectral behaviour were necessary, one could use the full temporal impulse response of the antenna in either circuit model of Fig. B.1 or Fig. 2.2 instead of the approximated load r_a. However, in case of broad band antennas characterised by radiation impedances with an approximatively constant real part, such as the bow tie investigated, an appropriate resistance represents a very good approximation.

The procedure hereby presented improves dramatically the state of the art from [26, 27, 28] as it allows to include the history of the PC materials while it does not necessitate any fine tuning from the measurements. The level of accuracy of the modelling introduced with this thesis is now comparable to that expected in non-pulsed heterodyne systems, and opens new opportunities to engineer much more advanced front ends, which will be in the end limited by the quality of the antenna designs.

Chapter 4

Fabrication and characterisation of leaky lens PCA for higher power fibre-based THz time domain systems

Presented in this chapter is the characterisation of a leaky wave photoconductive antennas that outperform the devices currently used in THz commercial systems for time-domain sensing applications. It is the first time that an antenna exploiting the leaky wave effect is manufactured with photoconductive material and employed in a TDSS setup. The power detected from the radiation of such leaky wave PCA's results much greater than what measured with state of the art devices under the same bias and optical excitation conditions. This makes these novel leaky wave PCA's stand out as a great candidate to be adopted in commercial THz time-domain sensing and spectroscopy systems, where the maximum laser power that can be used is limited by the dispersion in the optic fibre for high power excitations. The leaky wave PCA is entirely designed, manufactured, assembled and characterised within the TeraHertz Sensing Group and the Else Kooi Laboratory, at the Delft University of Technology.

4.1 Introduction

In commercial time domain sensing and spectroscopy systems, such as the one in fig. 1.1 adopted for the experiments of this thesis, the two communicating PCA's are coupled to femto-second lasers guided through optical fibres. These are used to pump the semiconductor over which the antenna is printed, which suddenly transits from a quasi-insulating to a highly conductive state.

The dynamic range of TDSS systems is highly dependent on the power radiated by the transmitter and its coupling with the receiver, as well as the frequency dispersion of the quasi-optical channel linking the two. In the literature, the use of coherent arrays of PCA's excited by high-power free-space lasers has been proposed to increase the power output of the transmitter [20]. However, the complex optical path necessary to excite the device makes them inconvenient for commercial applications, which typically require compact, portable systems. On the other hand, the use of fibre-coupled PCA's limits the laser power level that can be used due to the fibre dispersion: this caps the maximum THz power that can be generated with PCAs excited in this fashion, consequently affecting the dynamic range of the system.

As thoroughly explained in Chapter 2 the amplitude, temporal evolution and spectral distribution of the photocurrent induced in a transmitting PCA is a function of the properties of the optical excitation, of the semiconductor and of the effective electric field applied over the gap. In particular, the spectral distribution of the induced radiation depends on:

- the emitter photo-current magnitude and bandwidth;
- the matching between the impedance presented by the excited semiconductor gap and the antenna radiation impedance
- the QO channel propagation efficiency.

It appears from the literature that in the THz community the efforts have been mainly focused on the engineering of the semiconductor properties, e.g. carrier scattering and life time, through materials synthesis and post-processing [43, 44]. On the other hand, in the vast majority of the contributions the antenna architecture

and its radiation properties have never been a critical point of investigation, and the Auston switch remained the most widely adopted geometry in commercial as well as in research applications.

This chapter illustrates how the adoption of a leaky wave architecture based on a tapered slot would lead to more efficient illumination of the high-resistivity silicon lens and improve the quasi-optical efficiency. Specifically, the introduction of a small (in terms of the wavelength of the radiated field) air gap between the metallization and the lens is sufficient to enable a broad-band leaky radiation towards the lens vertical axis [22]. This leaky wave antenna, characterised by a stable radiation phase centre, improves the coupling between the PCA radiation with the QO channel.

The realisation of the device relies on a novel manufacturing technique that allows the creation of suspended LT-GaAs membranes with thicknesses of a few μm. In this chapter it is demonstrated that such a technique enables the fabrication of leaky-wave PCA's that reliably outperform the state-of-the-art devices in terms of radiated power and QO channel efficiency. In particular, these sources radiate higher levels of THz power under the same bias and optical conditions typical of commercial applications, disclosing their full potential for fibre-coupled THz TDSS systems.

Finally, the equivalent time-domain circuit introduced in Chapter 2 is tested using the leaky wave PCA presented in this chapter, confirming its accuracy in predicting the power radiated by broadband PCA sources even in case of large optical power levels.

4.1.1 Leaky wave PCA geometry

The detailed manufacturing procedure of the device can be found in Appendix C. The metallic component of the membrane antenna (see Fig. 4.1) is a 70° tapered, $1\mu m$ thick pure Al bow tie, with a square gap of $7.5\mu m$ side. The bow tie patter is 2mm long and 3mm wide. The contact pads extend beyond, for a total chip size of 6mm$\times$6mm. The LT-GaAs suspended membrane occupies the central square area of the chip, with the bow-tie gap at its centre. The membrane has a square shape of 3mm side and is $2\mu m$ thick. All the chip front surface, except for the

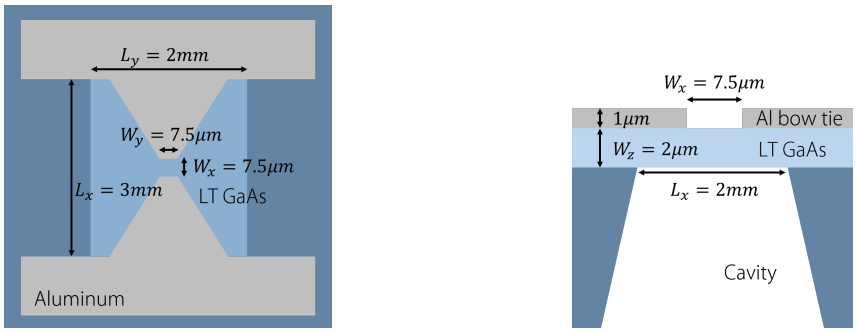

(a) (b)

Figure 4.1: Details of the leaky wave antenna introduced in this chapter. (a) The metallization bow tie geometry printed over the photoconductor with a taper angle of $70°$. (b) The details of the stratification of the structure on the vertical plane

contact pads has been covered with $2.6\mu m$ thick amorphous fluoropolymer (Cytop from AGC Chemicals, [35]) in order to provide a better mechanical strength to the fragile LT-GaAs membrane. The Cytop layer also serves to passivate the membrane surface against the formation of moisture layer, which would foster a premature electrical breakdown of the LT-GaAs during high voltage operation.

4.1.2 Leaky wave PCA assembly

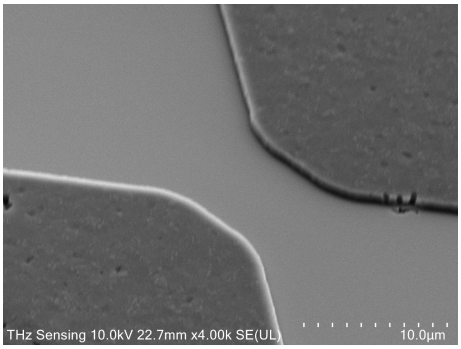

Figure 4.2: Picture acquired with a scanning electron microscope of the front side of the leaky wave lens antenna. One can see the metallisation pattern and the gap onto which the laser is shone, found at the opposite side of the HR Si Lens.

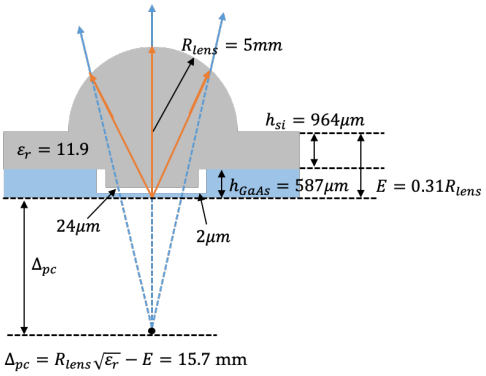

(a)

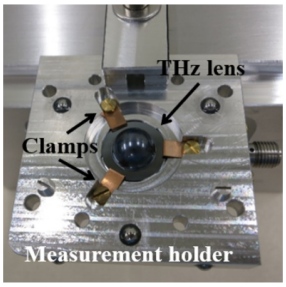

(b)

Figure 4.3: Details of the leaky wave antenna introduced in this chapter. (a) Geometry of the whole assembly on the vertical plane with the lens. (b) Picture of the actual leaky wave PCA on the measurement holder from the side of the Si lens.

To create the 3D structure required for the operation of the leaky lens antenna, a very similar assembly to the one used by the authors in [29] is adopted. An actual picture of the front side of the leaky lens antenna acquired with a scanning electron microscope is shown in Fig. 4.2. The assembling procedure, *e.g.* the alignment of the components to one another and the fixture, is the same as reported in [29]; the only difference lies in that the lens design is different in order the create the air gap between the antenna feed and the lens. The lens design is depicted in Fig. 4.3. This lens presents a mushroom-like shape, with a stalk sticking out of the flat side of it. The stalk protrudes inside the membrane cavity at the back of the wafer and is used to create the air gap.

In order the ensure that the air gap has the correct dimension, the membrane cavity depth is measured with a confocal microscope. The length of the stalk of the lens is changed accordingly to have a $20\mu m$ gap between the antenna feed and the lens. The depth of the membrane opening is $586\pm5\mu m$ depending on the position of the cavity in the wafer. The lens is made out of a high resistivity ($> 10k\Omega cm$) silicon ingot using single point diamond turning [45], and is fabricated after measuring the membrane cavity depth. The length of the stalk is consequently set at $561\pm5\mu m$.

4.2 Experimental validation

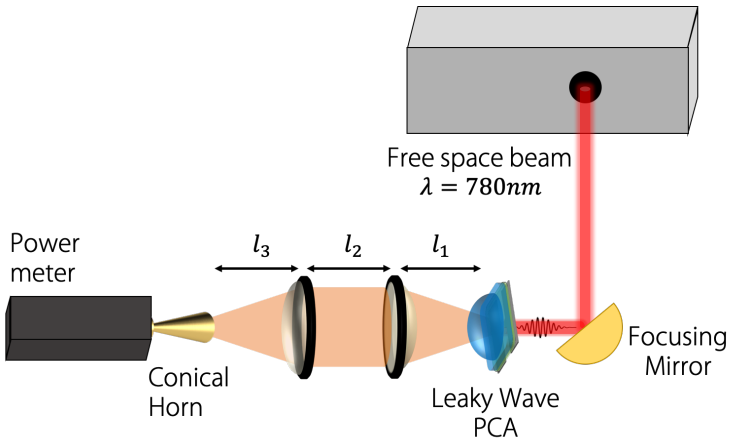

Figure 4.4: Schematic of the measurement setup adopted to characterise the power radiated by the leaky wave PCA: the transmitting PCA, the leaky wave lens antenna under investigation, is excited by the free space laser focused by an off-axis parabolic mirror. The field radiated is coupled to the receiving horn connected to a power meter via two polymer lenses. The quasi optical path dimensions are $l_1 = 35mm, l_2 = 60mm, l_3 = 20mm$.

The performances of the leaky wave photoconductive antenna presented in this chapter are assessed with experiments conducted in the Time Domain Laboratory of the Tera-Hertz Sensing Group, TU Delft. The set up adopted for the measurements is shown in Fig. 4.4, and is similar to what used in the characterisation of the bow tie in chapter 3.

The free space laser source used to excite the leaky wave PCA is part of the commercial system TERA K15, [36]: it operates at 780nm and is pulsed at 80MHz. The PCA is biased to a fixed voltage, V_b, which accelerates the photocarriers injected by the laser source. The induced pulse of photocurrent generates a radiation that is collected by a horn antenna (VDi, CH-WR10) connected to a power meter (VDi, PM5) [37]. The leaky wave lens antenna and the horn are coupled through a quasi-optical (QO) path consisting of 2 identical plano-convex polymer lenses (ThorLabs, TPX50) [38] that collect the THz radiation and guide it towards the horn.

4.2.1 Optical path and focused laser beam

The laser path is built as follows: the pulse has a Gaussian temporal profile with a full width at half maximum of $\tau_p = 100fs$; the average power ranges from $P_L = 1 \rightarrow 100mW$. The beam emerges with a 1/e waist of $w_0 = 6mm$, and needs to be focused down to a waist of $w_L = 6.4\mu m$ (which corresponds to a -3dB radius of $R_L = 3.75\mu m$, or diameter of $D_L = 2R_L = 7.5\mu m$) to match the PCA gap lateral dimensions $W_x = W_y = 7.5\mu m$, ideally. 40cm from the laser output is a gold 90° off-axis parabolic mirror with a reflected focal length of 15mm (ThorLabs, MPD00M9-M01) to focus the beam down to the desired value. Along the 40cm the beam remains well collimated.

Opposed to the setup in Fig. 3.3 the leaky wave PCA is not coupled to the TERA K15 receiver, which saves the need of the 390cm path: the total path amount to around 40cm, and the beam expander is not needed, since the beam stays well collimated. Finally, a focusing mirror is used instead of a lens.

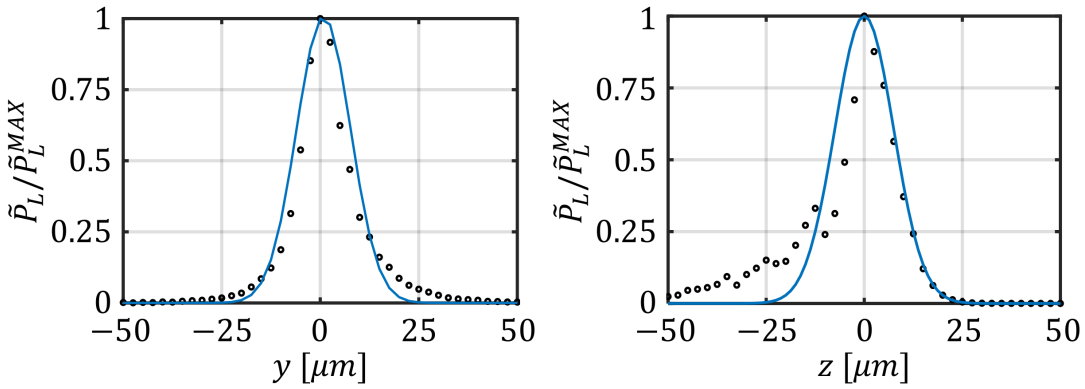

(a) profile on the vertical axis

(b) profile on the horizontal axis

Figure 4.5: Profile of the focused optical beam obtained with the setup in Fig. 4.4 along the vertical (y) and horizontal (z) axis, respectively. The solid blue line is a Gaussian fit to verify the gaussicity of the focused beam. The -3dB diameter of the beam along the y axis is $D_L^y = 11.9\mu m$, on the z axis it is $D_L^z = 12.7\mu m$.

To verify the laser profile and the alignment, the focused beam is profiled on both the horizontal and vertical axes using two metal blades and the knife-edge technique [39]. The blades are placed in a holder controlled by a 5-axis (3

translational and 2 rotational axis) motorised stage with a translational resolution of 1.25μm and a rotational resolution of 0.01°. The holder of the blade is the same one used for the antenna, thus ensuring that the measured profile is eventually the same exciting the investigated PCA.

The results are showed in Fig. 4.5. The best alignment obtained with the set-up in Fig. 4.5 could not match the ideal -3dB diameter of 7.5μm, and the aberration given by the focusing mirror introduces an asymmetric tail in the vertical plane. The measured spill-over efficiency is $\eta_{SO}^{y} = 0.42$ on the vertical axis, and $\eta_{SO}^{y} = 0.33$ on the horizontal axis, for an average spill-over efficiency of $\eta_{SO} \simeq 0.38$. The average spill-over efficiency between horizontal and vertical plane is measured at $\eta_{opt} = 0.23$.

4.2.2 Detected power

Once the desired optical beam profile on the focal plane is achieved, the blades are replaced with the target TX PCA. The holder of the antenna is identical to that used for the blades, thus ensuring that the gap of the PCA is excited by the measured beam profile; however, due to tolerances in the manufacturing of the holders, it was necessary to fine tune the device position in order to achieve the optimal illumination. The fine tuning is performed by biasing the antenna and measuring the DC current induced in the gap excited by the laser, maximising it with micrometrical position adjustments controlled by the 5-axis stage.

Before detecting the power radiated by the PCA, the position of the two lenses and the horn of the quasi-optical path are fine-tuned until the maximum power is received by the power meter. The final configuration is detailed in Fig. 4.4. The power radiated by the photoconductive antenna and collected by the power meter is then characterised as a function of the optical power. The chip is biased to a voltage potential which is swept as: $V_b = 10, 20, 30V$. Fig. 4.6 shows the THz power collected by the power meter; as a reference, the results are plotted against the power absorbed with the power meter using a bow tie PCA manufactured on the same wafer as the leaky wave PCA under test. The bow tie lens antenna adopted for the comparison is identical to the one analysed in Chapter 3, except for the gap of 7.5μm instead of $10\mu m$. Leaky wave PCA and bow tie PCA are excited by the same

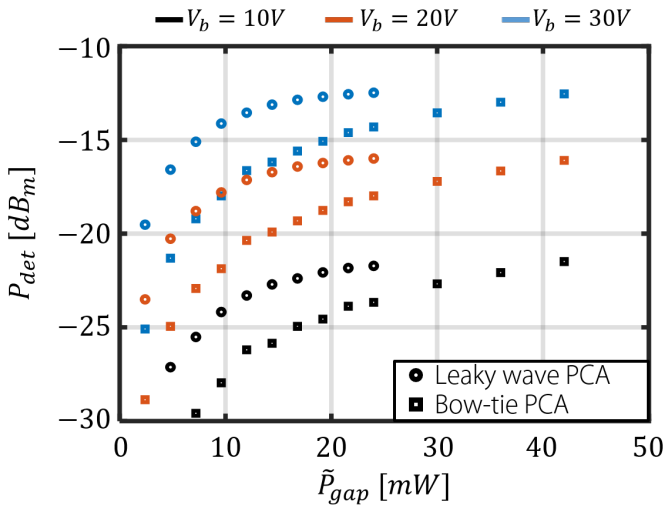

Figure 4.6: Detected THz power from leaky wave PCA and bow tie PCA for three different bias levels, $V_b = 10, 20, 30V$, as a function of the optical power absorbed in the PCA gap, $\tilde{P}_{gap} = \eta_{opt}\tilde{P}_L$. Note the saturation in the output power emerging under larger and larger optical excitations, which is faster for the leaky wave PCA.

beam of Fig. 4.5 and tested with the same bias and optical excitations. To compare the two different devices the power is expressed as a function of the optical power absorbed by the gap of the antennas, $\tilde{P}_{gap}$. Specifically, $\tilde{P}_{gap}$ relates to the total power illuminating the antenna through the optical efficiency as $\tilde{P}_{gap} = \eta_{opt}\tilde{P}_L$: η_{opt} accounts for the spill-over of the beam over the PCA gap, its absorption in the vertical axis z and its reflection efficiency (see Appendix A for the detailed derivation).

The optical efficiency is equal for the two devices under analysis, as the gaps onto which the laser is shone have the same dimensions. As expected, for both devices the increase of the average power of the pulsed laser does not lead to a proportional increase of the THz power. For larger optical excitations, the saturation effect becomes manifest, and it occurs faster for the leaky wave PCA than the bow tie PCA due to its larger radiation impedance, as visible in Fig. 2.6.

It is apparent that at any given bias voltage and laser power the leaky wave PCA radiates more efficiently than the bow tie, all the way up to saturation, after which it would make no sense to shine more power over the device. Indeed, while the photocurrent generated in the feed of the two devices is the same, the

power detected from the leaky wave PCA is significantly larger as opposed to what captured from the bow tie PCA under the same bias and optical excitation conditions. This is thanks to the better radiation pattern generated by the leaky wave PCA: the feed is more directive, illuminates the HR Si lens better, resulting in an overall better coupling with the QO path. However, since the saturation of the power radiated by the bow tie PCA happens for larger laser power, it appears that such a PCA might be adopted under stronger optical excitations; also greater bias voltages can be used, as the bow tie PCA is characterised by a bulky nature, and not a thin membrane, as opposed to the leaky wave PCA. Instead, the novel leaky wave PCA appears to be a great candidate when there are constraints on the maximum laser power that can be used, *e.g.* in commercial TDSS systems with in-fibre laser excitations, where the power travelling along the fibre cannot be increased indefinitely due to its dispersive behaviour. The leaky wave PCA indeed exhibits more directive patterns, reducing the coupling losses along the QO channel typically implemented by these systems.

4.2.3 Comparison between power measurements and simulations

The measurements are compared with the results predicted by the time-domain equivalent circuit presented in Chapter 2 and showed in the following. In order to do so, one needs to estimate the current in eq. (2.11), as well as simulate the antenna radiation properties and the coupling between the TX PCA and the receiving horn connected to the power meter for the setup in Fig.4.4. The average power radiated by the antenna is calculated as in equation (3.1), where the integration is performed with unilateral spectra. The parameters of the substrate of LT GaAs, with the scattering time $\tau_s = 8.5fs$ extracted in Chapter 3, and of the laser are listed in Table 2.1. The amplitude of the optical excitation, equation (2.4), is calculated using the measured -3dB beam diameter of Fig. 4.5.

The antenna radiation impedance, $Z_a(f)$, is simulated as a function of the frequency using a full-wave EM software, CST [40]. The impedance is shown in Fig. 4.7. In order to solve either time domain circuit of Fig. 2.2 or Fig. B.1 and evaluate the induced photocurrent of eq (2.11), $i_{rad}(t)$, it is convenient

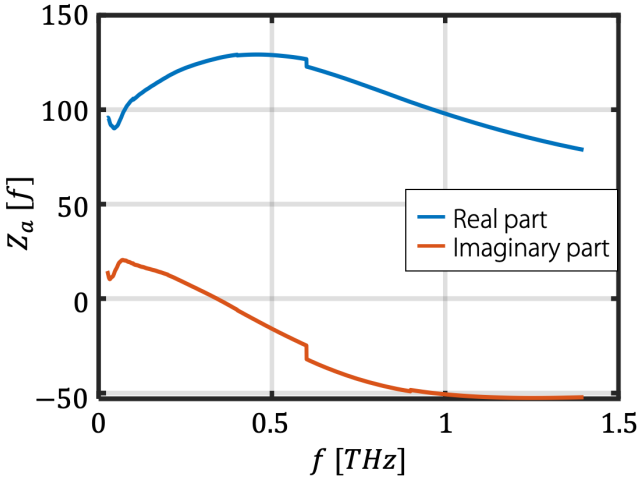

Figure 4.7: Radiation impedance of the leaky wave antenna under test simulated with CST

to approximate the antenna radiation impedance as a constant resistance. The resistance that led to the best matching between the predictions of the model and the actual measurements, see Fig. 4.9 while using the same $\tau_s = 8.5fs$ extracted in Chapter 3, results $Z_a(f) \simeq 125\Omega$. This radiation resistance is used to solve the circuit and calculate the induced photocurrent, $i_{rad}(t)$, and its Fourier transform as: $I_{rad}(f) = \mathscr{F}[i_{rad}(t)]$. However, this represents a very rough approximation for the leaky wave PCA radiation impedance of Fig. 4.7: a proper time domain impulse response must be extracted from the anti-Fourier transform of $Z_a(f)$ to obtain a better estimation.

The losses introduced by quasi-optical channel of Fig. 4.4 are evaluated through both measurements and simulations resorting to an in-house tool [41] alongside an EM modelling software, Ticra GRASP [42]; the PCA beam pattern has been computed and imported from CST. Fig. 4.8 (a) shows the coupling efficiency of the channel, $\eta_{QO}(f)$; Fig. 4.8 (b) the ohmic losses introduced by the polymer lenses guiding the THz radiation, $\eta_{TPX}(f)$; Fig. 4.8 (c) the total losses of the QO channel, $\eta_{QO,tot}(f) = P_{det}(f)/P_{rad}(f)$, as a function of the frequency. $\eta_{QO}(f)$ is estimated with in-house tool and Ticra GRASP; $\eta_{TPX}(f)$ is estimated for a plane wave propagating and using the $tan(\delta)$ given by measurements performed at the laboratories of

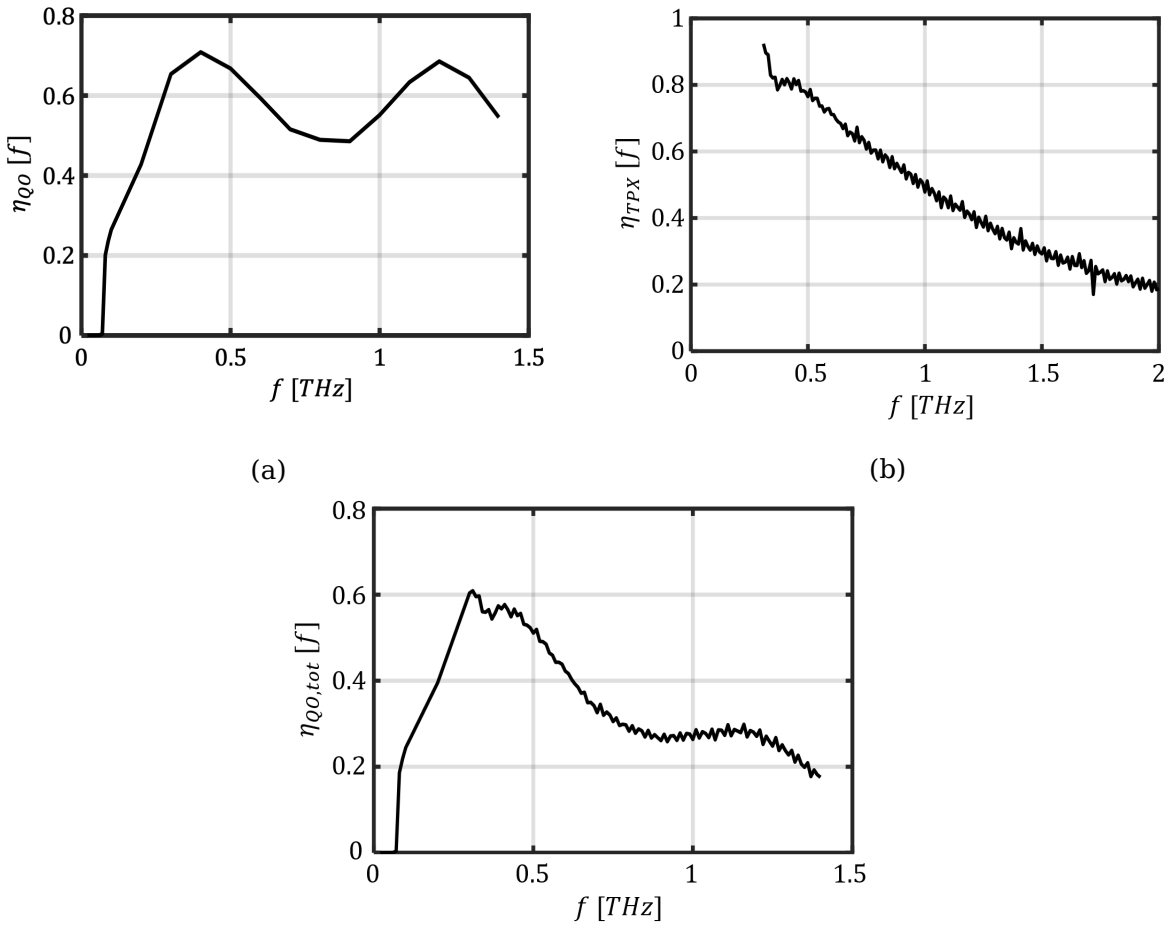

Figure 4.8: Quasi-optical efficiency describing the losses in the measurement setup in Fig. 4.4. (a) Radiation coupling losses between TX PCA and the horn connected to the power meter, (b) Ohmic losses introduced by the TPX lenses, (c) Total losses of the system, given by the product of the former two.

Menlo Systems, GmbH; $\eta_{QO,tot}(f)$ is the result of the product of the former two, $\eta_{QO,tot}(f) = \eta_{QO}(f) \cdot \eta_{TPX}(f)$.

The frequency oscillation of Fig. 4.8 (a) is the result of the adoption of a single matching layer that is tuned to maximise the efficiency at 400GHz and multiples. Instead, the largest losses are associated to the spill over in the conical horn: indeed, the horn is much more directive than the lens antenna, and as

a consequence the quasi optical efficiency remains limited. Finally, the cut-off introduced by the waveguide of the power meter is at 75GHz.

The quasi optical path of Fig. 4.4 is very similar to the one of 3.3 (b); however, the quasi optical efficiency here is much larger, thanks to the higher directivity of the leaky wave PCA that couples to the polymer lenses and the receiving horn antenna used to collect the THz radiation much more efficiently.

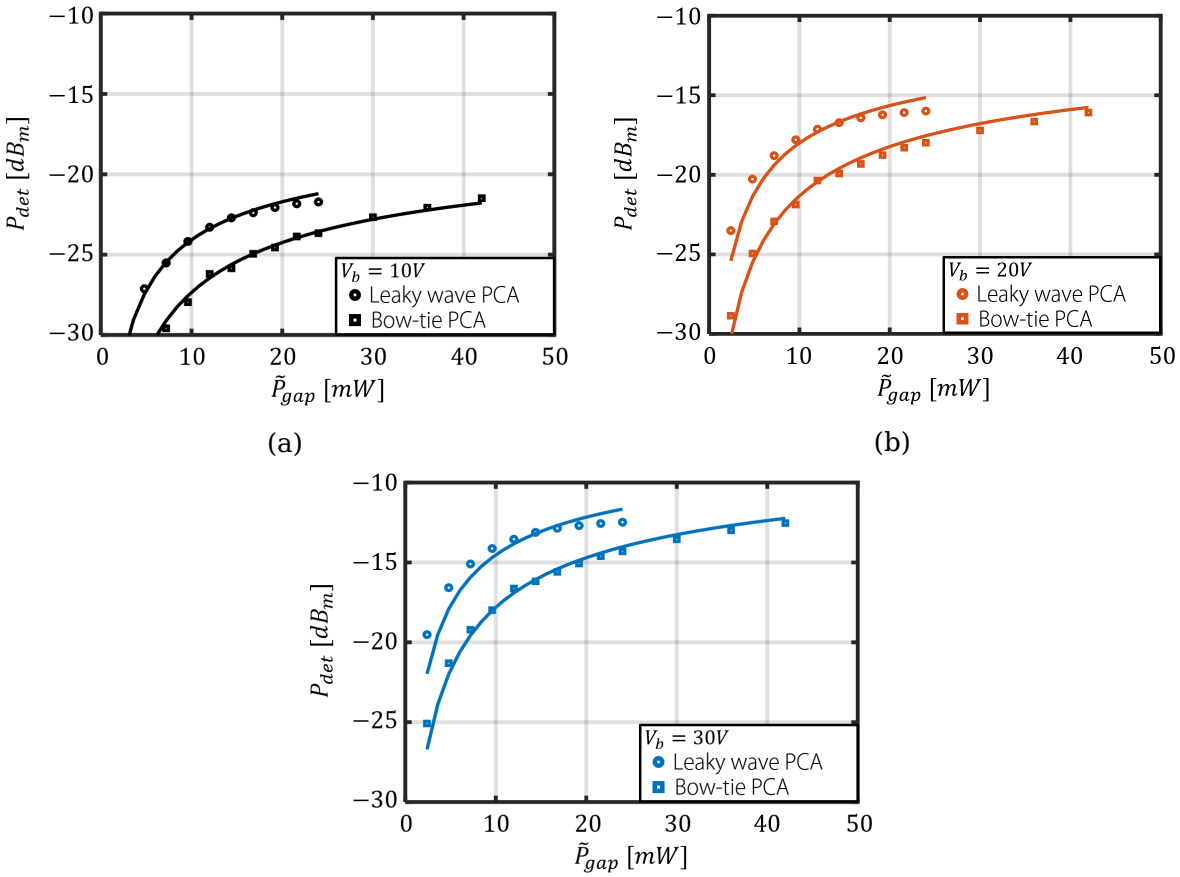

Figure 4.9: Detected THz power from leaky wave PCA and bow tie PCA for three different bias levels, $V_b = 10, 20, 30V$, as a function of the optical power absorbed in the PCA gap, $\tilde{P}_{gap} = \eta_{opt}\tilde{P}_L$. Note the saturation in the output power emerging under larger and larger optical excitations, which is faster for the leaky wave PCA.

Fig. 4.9 shows the THz power detected with the setup of Fig. 4.4 as a func-

tion of the average laser power exciting the antenna for 3 different bias levels, $V_b = 10, 20, 30V$, compared to the corresponding simulations. The agreement is exceptional, and the differences between the data predicted by the model presented here and the measurement lie within only 1dB. The scattering time chosen to fit the predictions from the model with the simulations is $\tau_s = 8.5fs$, same scattering time adopted for the bow tie studied in Chapter 3.

Also for this leaky wave antenna architecture the saturation effect occurring at large optical power levels emerging from the measured data is predicted by the model with outstanding accuracy. The slight disagreement emerging for the curve at low excitation levels is caused by the fact the THz radiated power approaches -30dBm, the lowest measurable power with the current set-up, worsening the signal to noise ratio. As a comparison, the results regarding the leaky wave PCA introduced in this chapter are plotted against those for the bow tie PCA with a $7.5\mu m$ gap manufactured on the same wafer: it is apparent that the leaky wave PCA is much more efficient, and the detected power is significantly higher as opposed to the bow tie under the same bias and excitation conditions. This is given by a better illumination of the HR Si lens from the feed, resulting in more directive radiated patterns and an overall better coupling with the QO path used to capture the radiation.

4.2.4 Effect of the QO channel

This subsection highlights the effect on the detected power caused by the coupling between the TX PCA and the horn connected to the power meter, together with the ohmic losses in the polymer lenses. The adopted QO channel, sketched and detailed in Fig. 4.4, belongs to the TERA K15 by Menlo Systems GmbH, and is a solution often used by other commercial TDSS: the only difference lies in that now the TX PCA is not the native Auston switch, but the leaky wave PCA analysed in this chapter.

Fig. 4.10 shows the effect of the losses of the QO path in Fig. 4.8. The comparison is done by plotting the power radiated versus the power detected from the leaky wave PCA as predicted by the model presented in Chapter 2 for two bias voltage points. The solid line represents the detected power, while the dotted line

represents the radiated power (obtained setting $\eta_{QO,tot}(f) = 1$ in eq. (3.1)).

Added in the plots is also the estimated radiated and detected power by the bow tie PCA with a $7.5\mu m$ wide gap. It is apparent that bow tie and leaky wave PCA radiate about the same power under the same excitation conditions. However, the field radiated by the leaky wave PCA couples better with the QO channel thanks to its better pattern, resulting in an overall larger detected power. Adopting this antenna in relatively low optical power scenarios, such as those of commercial TDSS systems, might be an advantage.

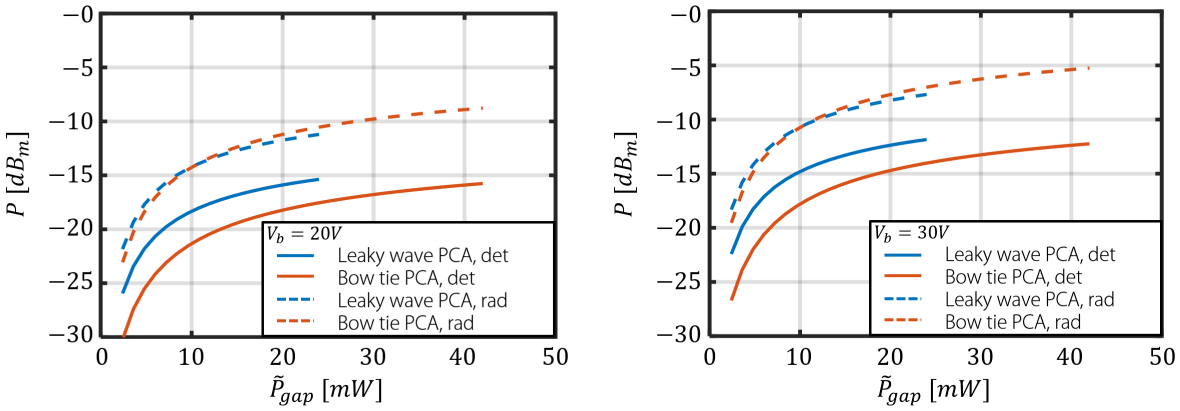

(a) (b)

Figure 4.10: Effect of the QO channel, *i.e.* Fig. 4.8: comparison between the power radiated (dotted line) and detected (solid line) from the leaky wave PCA as predicted by the model of Chapter 2. The estimated power radiated for the bow tie PCA with a $7.5\mu m$ gap is also plotted.

4.3 Conclusions

For all the aforementioned reasons the novel PCA presented in this chapter stands out as an excellent candidate for time domain sensing and spectroscopy systems. Indeed, the dynamic range of such systems is highly dependent on the power radiated by the TX PCA and its coupling with the QO channel. In the literature, the use of coherent arrays of PCAs combined with high-power lasers has been proposed for enhancing the power radiated by PCAs [20], but this would require optical

levels achievable exclusively through free-space laser excitations, inconvenient for most commercial applications, as they are more prone to optical components misalignment induced by transportation, thermal contraction/expansion of the materials due to the environment temperature fluctuations etc. Instead, the adoption of optical fibres to excite the photoconductive device make the system more compact as well as easier to transport and maintain. This is the solution generally chosen by commercial systems, which coupled to the leaky wave PCA presented here allow for larger levels of THz radiated power, and thus larger dynamic ranges, under the same bias and excitation conditions.

Chapter 5

The observable field in complex scattering scenarios

The observable field is defined as the portion of the incident field that can contribute to the power received by an antenna. Recently, the observable field was estimated for a plane wave incidence. Here, the procedure is extended to a general incident field expressed as a superposition of homogeneous plane waves. The observable field concept provides a methodology to evaluate the maximum power that could be received by an ideal antenna under a general field incidence. In particular, it emerges that to maximise the received power, the pattern of the antenna if it were used in reception should be synthesised to reproduce the angular pattern of the observable field. This is specifically relevant in cases of non-line of sight (NLOS) at high frequencies, where the power received can drop by orders of magnitude.

5.1 Introduction

The definition of the power available to an antenna illuminated by a plane wave has been extensively discussed in [46, 47, 48, 49] and it is still a relevant research topic [50, 51, 52]. Nowadays, there are many applications, such as time-domain sensing, radar systems, wireless communications, and automotive applications, where the receiving antenna is immersed in a complex environment, and the incident field cannot be represented with a single plane wave. In such complex scenarios, it

could be very useful to *a priori* understand what could be the maximum power that can be theoretically received by a lossless antenna. In fact, this knowledge allows to evaluate the margin of improvement that could be expected when a complex antenna system is exploited.

For this purpose, hereby presented is a generalisation of the observable field methodology already introduced in [52] for a single plane wave incidence. There, the observable field was defined as the portion of a single incident plane wave that can contribute to the signal received by an antenna filling a fixed volume (a sphere of radius a). The observable field was obtained by removing from the incident field the portion that provides negligible contributions to the received signal, *i.e.* the remaining field, $\vec{e}_{rem}(\vec{r})$, as follows:

$$\vec{e}_{obs}(\vec{r}) = \vec{e}_i(\vec{r}) - \vec{e}_{rem}(\vec{r}) \tag{5.1}$$

In particular, for a given incident plane wave with electric field, $\vec{e}_i(\vec{r})$, the angular distribution of the observable field was constructed in [52] as the radiation from the equivalent currents radiating the incident field behind the antenna but truncated on a disk, with diameter equal to the minimum sphere enveloping the antenna, orthogonal to the direction of propagation. The angular distribution was multiplied by a specific constant that can be analytically calculated, ensuring that the observable field carries the available power that an ideal antenna can receive, even in the case of electrically small antenna domains. For a complex incident field distribution, the field can be first expressed as a continuous superposition of homogeneous plane waves. Then, a procedure similar to that described in [52] can be applied, where the equivalent currents distributions are calculated as coherent superposition of those obtained for each component of the homogeneous plane wave spectrum (PWS) distributed now on a spherical domain. The amplitude of the observable field cannot anymore be evaluated analytically but numerically via field reaction integrals.

The observable field evaluates the largest portion of a generic incident field that can be absorbed by a spherical volume: in other words, this methodology synthesises the optimal spatial current distribution within that volume for that specific field. This is especially useful when the receiving terminal is immersed in

a complex scattering scenario, as in the example of the experiment conducted in Chapter 3 and Chapter 4 and for other sensing applications.

However, to demonstrate the validity of the proposed methodology, terminal antennas for 5G [53] or for further generation communication systems are discussed. In complex scattering scenarios, the optimal terminal antenna that maximises the received power is an open research question [54, 55]. In particular, in high-frequency wireless links, the receiving terminal can be a phased array antenna with beam-shaping capabilities [54, 56, 57, 58] to overcome limitations due to possible absence of a line of sight (LOS) link [59]. The terminal antenna should be steered toward the base station (LOS link) or toward strong nearby reflecting objects, non line of sight (NLOS) link. Moreover, for mm-wave links, the terminal antenna could also exploit beam-shaping capabilities to ensure the link from nearby objects, as shown in the scenario described in this chapter.

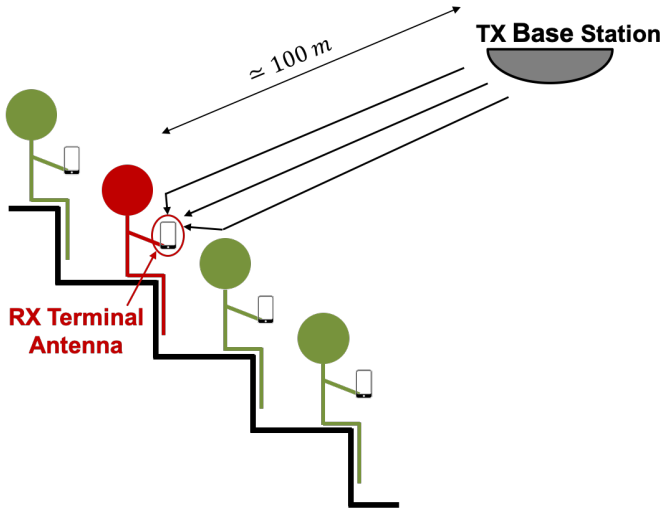

Figure 5.1: Stadium scenario: geometry, including the base station, and the main scatterers

The imagined scenario depicts tens of thousands of users each one carrying a mobile terminal antenna receiving a signal coming from a transmitting base station located, in the centre of the stadium at about 100 m, see Fig. 5.1. For such scenario, a possible 120 GHz architecture, based on an LOS power budget analysis to provide on-demand coverage, was proposed in [60]. To derive the optimal

beam shape which maximises the received signal, it is convenient to analyse the propagation channel in downlink. This is because the base station antenna provides a predictable field independently of the position and orientation of each specific terminal. Thus, the incident field on the mobile terminal needs to be evaluated just once.

Here, a carrier frequency of 120 GHz is investigated. The dominant contribution to the observable field is typically given by the LOS signal; however, contributions emerging from the main nearby scatterers (reflected, transmitted, and diffracted rays) are also clearly identifiable and, thus, can be driving the synthesis of the reception beams when the LOS is not the dominant term.

5.2 Observable field evaluation for general incident field

In this section, a procedure is proposed to derive the observable field for an antenna located inside a spherical domain S_a of radius a, when illuminated by an arbitrary incident field. The observable field evaluates the maximum power that can be received by the antenna. In the literature, different procedures have been suggested to evaluate such maximum power for a single plane wave incidence [46, 47, 48, 52]. Here, the procedure in [52] is generalised to account for an arbitrary illumination.

For a general source distribution, the incident electric field, defined in the absence of the antenna, can be expressed as a continuous superposition of homogeneous plane waves as:

$$\vec{e}_i(\vec{r}_a) = \int_0^{2\pi} \int_0^{\pi} \vec{E}_i^{pws}(-\hat{k}_i) e^{jk\vec{r}_a \cdot \hat{k}_i} d\hat{k}_i \tag{5.2}$$

where $\vec{r}_a$ identifies an observation point on the antenna domain, $\hat{k}_i = sin\beta_i cos\alpha_i \hat{x} + sin\beta_i sin\alpha_i \hat{y} + cos\beta_i \hat{z}$, $\vec{E}_i^{pws}$ is the electric field PWS associated to the incident field, $-\hat{k}_i$ is the direction of propagation of each plane wave. The magnetic field spectrum is evaluated as $\vec{H}_i^{pws} = -\hat{k}_i \times \vec{E}_i^{pws}/\zeta$. The integral in equation (5.2) is parametrised with $\beta_i \in (0, \pi), \alpha_i \in (0, 2\pi)$ and $d\hat{k}_i = sin\beta_i d\beta_i d\alpha_i$. The derivation of the PWS, $\vec{E}_i^{pws}$,

from the knowledge of the incident electric and magnetic fields on a sphere of radius $R_f > a$ enclosing the antenna domain is shown in Appendix D.

Similarly, as in [52], the observable field is defined in the far field of the antenna domain, $\vec{r}_\infty$, as the product of a normalised spherical wave, $\vec{f}_{po}(\vec{r}_\infty)$, and the amplitude, C:

$$\vec{f}_{obs}(\vec{r}_\infty) \simeq C\vec{f}_{po}(\vec{r}_\infty) \tag{5.3}$$

where for convenience the electric and the magnetic fields are combined in a unique vector:

$$\vec{f}(\vec{r}) = \begin{pmatrix} \vec{e}(\vec{r}) \\ \vec{h}(\vec{r}) \end{pmatrix} \tag{5.4}$$

Both the amplitude, C, and the angular distribution, $\vec{f}_{po}$, are functions of the incident field and the antenna domain S_a via its radius a. The amplitude C ensures that the observable field carries the available power that the ideal antenna can receive. This amplitude tends to unity for electrically large antenna domains, while it grows for $a/\lambda \to 0$. For each plane wave component of the spectrum in (5.2), the field scattered by the ideal receiving antenna can be approximated using surface currents, $\vec{j}_{po}(\hat{k}_i, \vec{r}_a), \vec{m}_{po}(\hat{k}_i, \vec{r}_a)$, defined over the antenna domain, and evaluated adopting a physical optics approximation. The angular distribution $\vec{f}_{po}$ is then derived from the field radiated by the superposition of all the current distributions (one for each component of the homogeneous PWS of the incident field).

Specifically, the electric and magnetic fields in the right-hand side of (5.3) are expressed as the sum of an inward and an outward propagating wave, as:

$$\vec{e}_{po}(\vec{r}_\infty) = \vec{V}_{po}^{inw}(\vec{k})\frac{e^{jkr_\infty}}{r_\infty} + \vec{V}_{po}^{outw}(\vec{k})\frac{e^{jkr_\infty}}{r_\infty} \tag{5.5a}$$

$$\vec{h}_{po}(\vec{r}_\infty) = -\frac{1}{\zeta}\hat{k} \times \vec{e}_{po}^{inw}(\hat{k}) + \frac{1}{\zeta}\hat{k} \times \vec{e}_{po}^{outw}(\hat{k}) \tag{5.5b}$$

where $\hat{k} = sin\theta cos\phi\hat{x} + sin\theta sin\phi\hat{y} + cos\theta\hat{z}$ and $\vec{V}_{po}^{inw}(\hat{k}) = \vec{V}_{po}^{outw}(-\hat{k})$. In (5.5), the factorisation of the inward and outward waves separates the angular (θ, ϕ) dependence of the observable field from the radial dependence (r_∞).

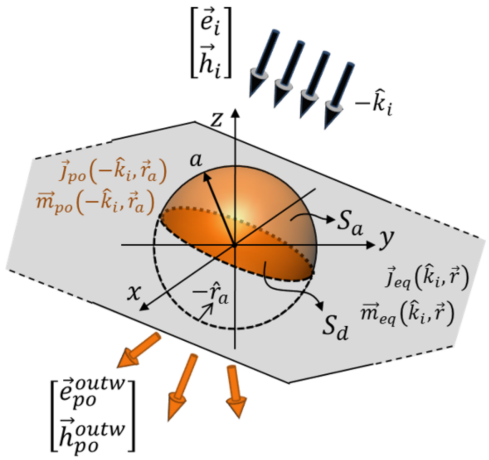

Figure 5.2: Geometrical definition of the domains where the PO currents $\vec{j}_{po}, \vec{m}_{po}$ are distributed for a single plane wave impinging from $-\hat{k}_i$. The equivalent currents, defined over a plane orthogonal to $\hat{k}_i$ (highlighted in grey), plus those defined on the disk S_d or on the top hemisphere of S_a, represent the incident field in the half space $\vec{r}_i \cdot \vec{k}_i < 0$. The PO currents are the equivalent currents truncated over the antenna domain (highlighted in orange): either the disk S_d or the top hemisphere of S_a.

5.2.1 Angular distribution of the observable field

In [52], it was proposed that the outward angular distribution, $\vec{V}_{po}^{outw}(\vec{k})$, of the observable field related to an ideal antenna illuminated by a single plane wave, $-\hat{k}_i$, could be evaluated as the field radiated by uniform surface currents, $\vec{j}_{po}(\hat{k}_i, \vec{r}_a), \vec{m}_{po}(\hat{k}_i, \vec{r}_a)$, defined over the disk $S_d(\hat{k}_i)$ of radius a, defined in Fig. 5.2, orthogonal to the plane wave direction of propagation. The currents over the disk can be seen as a spatial truncation of the equivalent currents that will describe the plane wave incident field in the half space below the disk (*i.e.* $\vec{r} \cdot \hat{k}_i < 0$ in Fig. 5.2). An ideal antenna operated in reception should scatter a field, $\vec{e}_{scat}(\vec{r}_\infty)$ which is equal but opposite to the outward propagating wave of the observable field, $\vec{e}_{scat}(\vec{r}_\infty) = -C\vec{e}_{po}^{outw}(\vec{r}_\infty)$, cancelling it out. In other words, the ideal antenna absorbs the entire inward propagating power of the observable field.

It can be shown that the equivalent currents, evaluated over the disc or over a half spherical surface that is bounded by the same disk (see Fig. 5.2), radiate the same field in $\vec{r} \cdot \hat{k}_i > 0$. The advantage of expressing the currents on the sphere

S_a rather than on the disk is that, when multiple plane waves are combined, an effective total current emerges as the sum of all contributions over a continuous surface.

Generalising to any incident plane wave direction, $-\hat{k}_i$, the chosen hemispherical surface, where to distribute the equivalent currents, faces the direction of origin of the plane wave, *i.e.* $\vec{r} \cdot \hat{k}_i > 0$ (top sphere). Therefore, the appropriate set of PO currents over the entire spherical domain S_a can be expressed as follows:

$$\vec{j}_{po}(-\hat{k}_i, \vec{r}_a) = \begin{cases} -\hat{r}_a \times \vec{H}_i^{pws}(-\hat{k}_i) e^{jk\vec{r}_a \cdot \hat{k}_i} & \vec{r} \cdot \hat{k}_i > 0 \\ 0 & \vec{r} \cdot \hat{k}_i < 0 \end{cases} \tag{5.6a}$$

$$\vec{m}_{po}(-\hat{k}_i, \vec{r}_a) = \begin{cases} \hat{r}_a \times \vec{E}_i^{pws}(-\hat{k}_i) e^{jk\vec{r}_a \cdot \hat{k}_i} & \vec{r} \cdot \hat{k}_i > 0 \\ 0 & \vec{r} \cdot \hat{k}_i < 0 \end{cases} \tag{5.6b}$$

The angular distribution of the outward component of the observable field, $\vec{e}_{po}^{outw}$, can be then calculated as the radiation from a continuous summation of the currents distributions in (5.6) related to each homogenous plane wave components of the incident field spectrum, as follows:

$$\vec{j}_{po}(\vec{r}_a) = \int_0^{2\pi} \int_0^{\pi} \vec{j}_{po}(-\hat{k}_i, \vec{r}_a) d\hat{k}_i \tag{5.7a}$$

$$\vec{m}_{po}(\vec{r}_a) = \int_0^{2\pi} \int_0^{\pi} \vec{m}_{po}(-\hat{k}_i, \vec{r}_a) d\hat{k}_i \tag{5.7b}$$

Fig. 5.3 gives a graphical example of how these ideal currents are generated in a point Q of the spherical surface S_a of coordinate $\vec{r}_a$. In particular, only the inward portion of the incident field spectrum for which $\vec{r}_a \cdot \hat{k}_i > 0$ contributes to the equivalent currents in Q.

The spherical surface S_a is taken here for the sake of simplicity, however any closed surface bounding the antenna can be chosen and the proposed procedure can be easily extended, following the same PO approximation.

For the sake of clarity, Fig. 5.4 shows the ideal electric currents due to different combinations of plane waves impinging from the $z > 0$ half space and propagating along the (x, z) plane. Fig. 5.4 (a) shows the magnitude of the x component of the

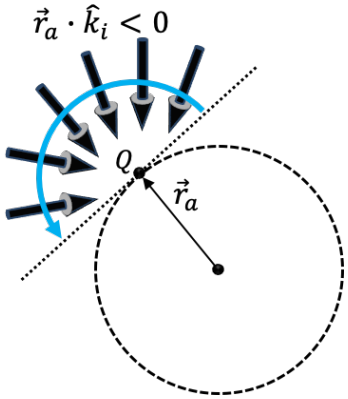

Figure 5.3: Inward plane waves contributing to the PO currents in an arbitrary point Q of the spherical surface S_a.

equivalent electric current distribution $\vec{j}_{po}$ on the sphere S_a for the case of a single plane wave coming from broadside, $\beta_i = 0$, whose electric field is linearly polarised along $\hat{x}$. The antenna spherical domain radius is set to $a = \lambda$. The currents are distributed only on the upper half of the sphere. Fig. 5.4 (b) and (c) show the magnitude of the x component of the equivalent electric currents $\vec{j}_{po}$ in case of two plane waves coming from directions $\beta_i = \pm 15°$ and polarised as shown in the figures inset. Fig. 5.4 (b) is pertinent to two plane waves whose electric field sum in-phase at the origin (referred as in-phase configuration) whereas Fig. 5.4 (c) corresponds to the out of phase summation (referred as out-phase configuration). For these configurations, the currents remain relevant only on the top sphere. Finally, Fig. 5.4 (d) and (e) show similar quantities but for two plane waves coming from directions $\beta_i = \pm 15°$. In these cases, the ideal currents are relevant also on the bottom sphere.

It is worth noting that for more realistic cases where the field spectrum is continuous, no discontinuities will be observed for the current distributions, unlike for these simplified examples.

The far-field outward distributions of the observable fields corresponding to the in-phase and out-phase plane wave configurations of Fig. 5.4 (b) and (c) are shown in Fig. 5.5 (a) and (b), respectively. Three different antenna domain radii are now investigated. It is apparent that for large radii in terms of wavelength,

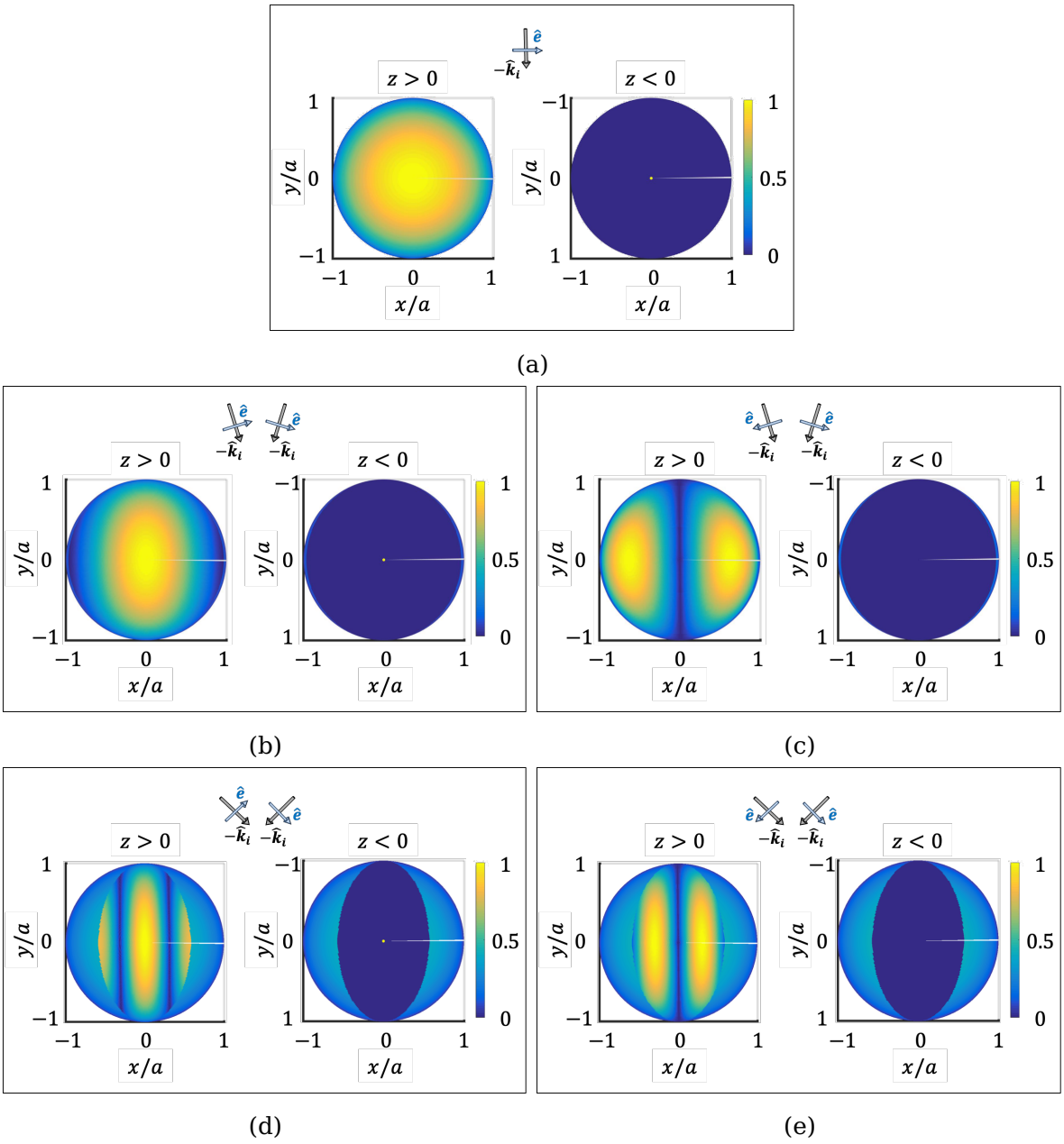

Figure 5.4: Normalised magnitude of the x-component of the ideal electric currents $|\vec{j}_{eq,x}|/max|\vec{j}_{eq,x}|$ (top-hemisphere $z > 0$ to the left, bottom-hemisphere $z < 0$ to the right), for the plane wave configurations sketched in the inset of each figure: single plane wave coming from broad side (a), two plane waves coming from $\beta_i = \pm 15°$ with in-phase (b) and out-phase (c) configurations, and $\beta_i = \pm 55°$ with in-phase (d) and out-phase (e) configurations.

the in-phase and out-phase outward observable field patterns are similar and are both characterised by two distinct beams related to the direction of the incident waves. Conversely, for electrically small radii, the plane wave configuration makes a significant difference in the pattern of the observable field. Note that for small radii, due to the low directivity, the observable field tends to reproduce a Huygens' pattern for the in-phase case.

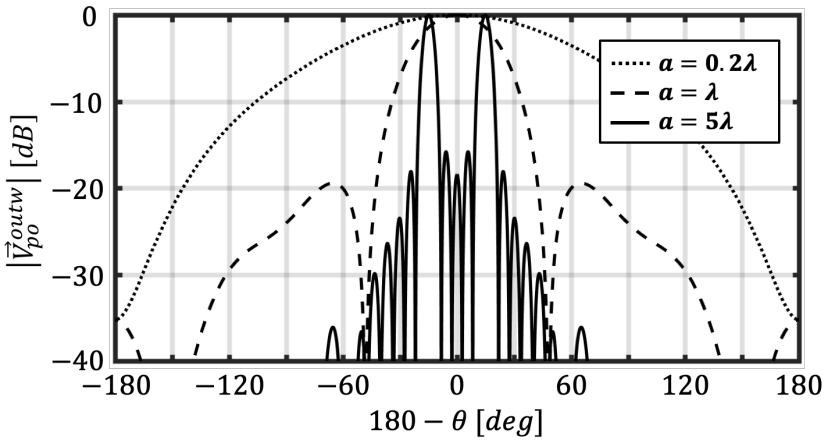

(a)

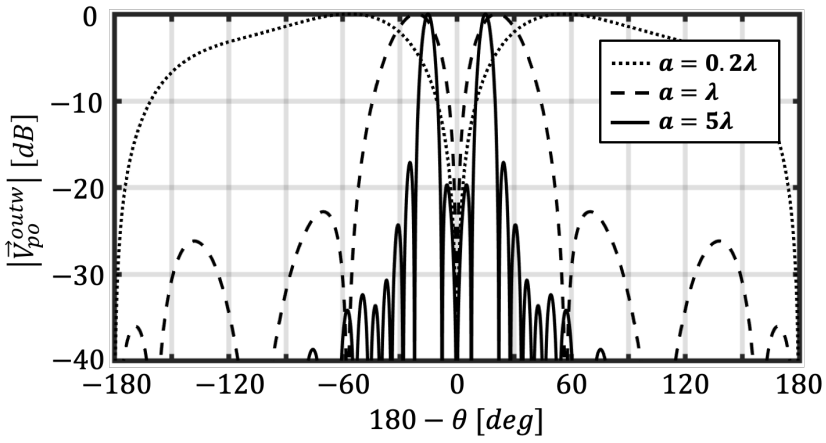

(b)

Figure 5.5: Normalised magnitude plots of the outward component of the observable field predicted by the ideal current procedure for three different antenna radii when two plane waves are impinging from $\beta_i = \pm 15^\circ$ for the in-phase (a) and out-phase (b) configurations.

5.2.2 Amplitude of the observable field

The amplitude C of the observable field was given analytically in [52] for a single plane wave. In case of a generalised incident field, this amplitude depends on the superposition of all the plane wave components and has to be evaluated numerically. To this purpose, the observable field in (5.3) can be thought as the product of a single basis function, $\vec{f}_{po}$ and its associated amplitude, C. Appendix E clarifies how this amplitude can be approximated resorting to the reciprocity reaction integral between the incident field and the field radiated by the ideal antenna, as follows:

$$C \simeq \frac{< \vec{f}_i, \vec{f}_{tx} >}{< \vec{f}_{po}, \vec{f}_{tx} >} \tag{5.8}$$

where the reaction integral between two generic basis $\vec{f}_b = \binom{\vec{e}_b}{\vec{h}_b}$ and test $\vec{f}_t = \binom{\vec{e}_t}{\vec{h}_t}$ functions is taken as follows:

$$< \vec{f}_b, \vec{f}_t >= \iint_{S_\infty} \left(\frac{1}{\zeta} \vec{e}_b(\vec{r}) \cdot \vec{e}_t(\vec{r}) - \zeta \vec{h}_b(\vec{r}) \cdot \vec{h}_t(\vec{r}) \right) \tag{5.9}$$

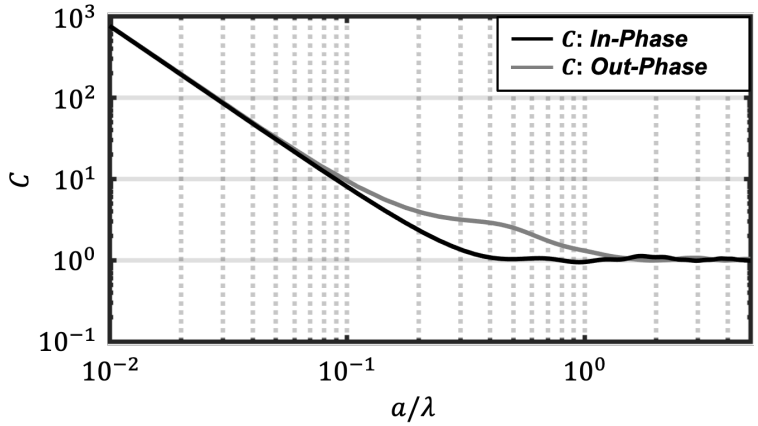

Figure 5.6: Value of the amplitude constant C as a function of the antenna dimension in case of two plane waves incoming from $\beta_i = \pm 15°$ for the in-phase and out-phase configurations described in Fig. 5.4 (b) and (c), respectively.

The integration in (5.9) is performed on a spherical surface, S_∞, located in the far field of the antenna. In (5.8) $\vec{f}_i$ is the field vector associated to the incident field,

while $\vec{f}_{tx}$ is the field vector associated to the fields radiated by the ideal antenna when operating in transmission (for more details refer to Appendix E).

Fig. 5.6 shows the value of the amplitude constant C for the same incident field cases of Fig. 5.5 as function of the antenna domain radius. It can be seen that for electrically large domains, where the scattered field by the PO currents represents well the incident field in the region behind the antenna, the amplitude constant tends to unity, and a field picture similar to that of the penumbra region in large objects is achieved [49]. In this case, the power received by the ideal antenna under a single plane wave can be represented with an effective area tending to its physical area [52]. Instead, the amplitude C grows for $a/\lambda \to 0$ compensating the fact that the physical area tends to zero.

5.3 Estimation of the available power

Using the Thevenin equivalent circuit, the power received by a matched antenna can be expressed in terms of its open circuit voltage, V_{OC}, and its radiation resistance, R_{rad}, as follows:

$$P_{rec} = \frac{|V_{OC}|^2}{8R_{rad}} = \frac{|V_{OC}I_0|^2}{16P_{rad}^{tx}(I_0)} \tag{5.10}$$

where the radiation resistance is expressed in terms of the power $P_{rad}^{tx}(I_0)$ radiated by the same antenna assuming I_0 as the value of the current flowing into the antenna terminals when operating in transmission. It is known that $V_{OC}I_0$ can be expressed as a reaction integral [61] on the surface of a sphere S_∞ at large distance from the antenna, as:

$$V_{OC}I_0 = \iint_{S_\infty} \left(\vec{e}_{tx}(\vec{r}) \times \vec{h}_i(\vec{r}) - \vec{e}_i(\vec{r}) \times \vec{h}_{tx}(\vec{r})\right) \cdot \hat{r} d\vec{r} \tag{5.11}$$

where $\vec{e}_i, \vec{h}_i$, is the incident field in absence of the antenna and $\vec{e}_{tx}, \vec{h}_{tx}$ are the fields radiated by the antenna when operated in transmission. For the ideal antenna, these fields are those radiated by the currents $\vec{j}_{tx}(\vec{r}_a), \vec{m}_{tx}(\vec{r}_a)$ defined in

(E.3). The amplitude of these currents is proportional to I_0 which value is, however, not relevant for calculating the received power in (5.10).

Since the fields evaluated in (5.11) are in the far field region of the antenna $\vec{h}_{tx} = \frac{1}{\zeta}\vec{r} \times \vec{e}_{tx}$, and (5.11) can be re-written as:

$$V_{OC} I_0 = \iint_{S_\infty} \left(\frac{1}{\zeta} \vec{e}_{tx}(\vec{r}) \cdot \vec{e}_i(\vec{r}) - \zeta \vec{h}_{tx}(\vec{r}) \cdot \vec{h}_i(\vec{r}) \right) d\vec{r} = < \vec{f}_i, \vec{f}_{tx} > \tag{5.12}$$

which corresponds to the reaction integral in (5.9).

On the other hand, as demonstrated in Appendix E, the power radiated by the ideal antenna in transmission can also be expressed in terms of a reaction integral as $P_{rad}^{tx} = \frac{1}{4} < \vec{f}_{po}, \vec{f}_{tx} >$. Accordingly, by using equation (5.10) and (5.12), the available power to any antenna bounded by the surface S_a can be expressed as follows:

$$P_{ava} = \frac{\left| < \vec{f}_i, \vec{f}_{tx} > \right|^2}{4 < \vec{f}_{po}, \vec{f}_{tx} >} \tag{5.13}$$

Finally, by using the expression of the observable field (5.3) and the approximation of its amplitude (5.8), the available power becomes equal to the inward (or the outward) power associated to the observable field:

$$P_{ava} = \frac{|C|^2 < \vec{f}_{po}, \vec{f}_{tx} >}{4} = P_{inw} = P_{outw} \tag{5.14}$$

where $P_{inw,outw} = \frac{|C|^2}{2\zeta} \iint_{S_\infty} \left| \vec{e}_{po}^{\,inw,outw}(\vec{r}) \right|^2$. It is worth noting that the calculation of the observable field constant, C, as defined in (5.8), can be costly from a numerical point of view, given the fact that the incident field is characterised by fast oscillations when projected on a sphere of large radius in terms of wavelength. This is a typical situation in many scattering problems. To this regard, resorting to the reciprocity theorem, the field reaction in (5.12), which also appears in the numerator of (5.8), can be performed over the antenna domain sphere, S_a, as follows:

$$< \vec{f}_i, \vec{f}_{tx} >= \iint_{S_a} \left(\vec{j}_{tx} \cdot \vec{e}_i - \vec{m}_{tx} \cdot \vec{h}_i \right) d\vec{r}_a \tag{5.15}$$

The evaluation of this reaction is more efficient as the oscillations of the incident fields are much slower than in (5.12). An application domain in which (5.15) is particularly appropriate is detailed in the next section, which introduces a complex scattering scenario.

To clarify the meaning of the available power under the incidence of multiple plane waves, it is useful to investigate the same cases described in Figs. 5.5 and 5.6 of two incident plane waves with unitary electric field magnitude. Fig. 5.7 shows the available power, normalised to the one obtained from a single incident plane wave with unitary electric field magnitude impinging from $\beta_i = 0$, as a function of the antenna radius a. The dashed lines shows the results evaluated using the proposed procedure for both in-phase and out-phase configurations. For small antenna radii the curves pertinent to the in-phase field configuration start from values close to 4, indicating an almost coherent summation of the field contributions. The out-phase curves, starting almost from zero, indicate an almost complete cancellation. For larger radii, the outward observable field tends to reconstruct two completely independent beams, pointing toward $\theta = 180° \pm 15°$, as shown in Fig. 5.5. Accordingly, the total available power remains equal to twice the contribution of each plane wave when considered individually. For this scenario, there is no qualitative difference between the in-phase and out-phase cases, and the power density carried by each incident plane wave is summed incoherently. In the same figure, a comparison between the available power calculated by using a spherical modes representation, as suggested by [50], is also reported. As in the case of a single plane wave described in [52], the quantised nature of the spherical wave expansion emerges clearly; however, the curves, obtained using both the spherical modes and the ideal currents procedure, are qualitatively equivalent for larger antenna radii, where the discretisation error becomes negligible.

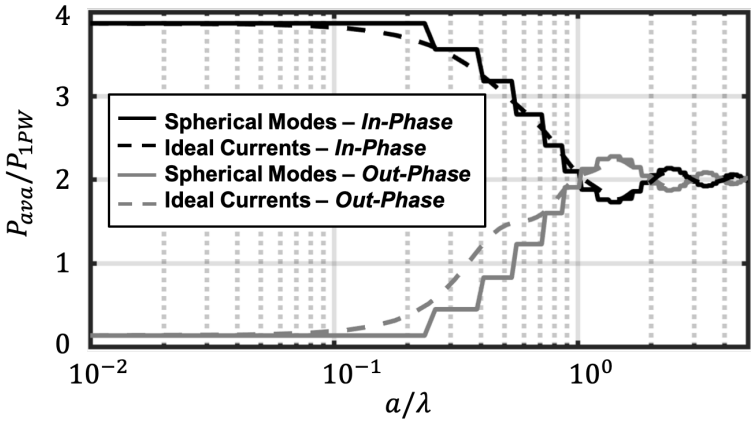

Figure 5.7: Available power as a function of the antenna domain radius for two plane waves, with unitary electric field magnitude and impinging from $\beta_i \pm 15°$, normalised to the available power obtained for a single plane wave having the same magnitude. Comparison between ideal currents (solid) and $N = [ka)$ spherical modes (dash) procedures.

5.4 The stadium scenario

With reference to Fig. 5.1 a stadium with tens of thousands of spectators is considered equipped with a wireless system as described in [15]. The wireless link to the spectators is provided via a centrally positioned base station (assumed for simplicity to be at a distance of 100m from the investigated spectator). A carrier frequency of 120GHz is considered. A radiated power of $P_t = 14dBm$ is transmitted in each beam that the base station generates independently. The gain of the base station antenna is characterised by an effective area at of $G_t\lambda^{/}(4\pi) = 12.5cm^2$. At the envisioned high frequencies scenario, the base station generates thousands of narrow independent beams, each covering a small angular cell that hosts $\simeq$50 spectators.

In the present example, the line of sight (LOS) field reaches the spectator with an angle of $\theta_{BS} = 0°$ with respect to the horizon (see Fig. 5.8) and a linear polarisation along $\hat{y}$. To obtain a complete description of the incident fields on the terminal antenna, the LOS contribution must be complemented by the field scattered by the surroundings. The schematic representation of the scatterers around the investigated terminal antenna is shown in Fig. 5.8: they are the

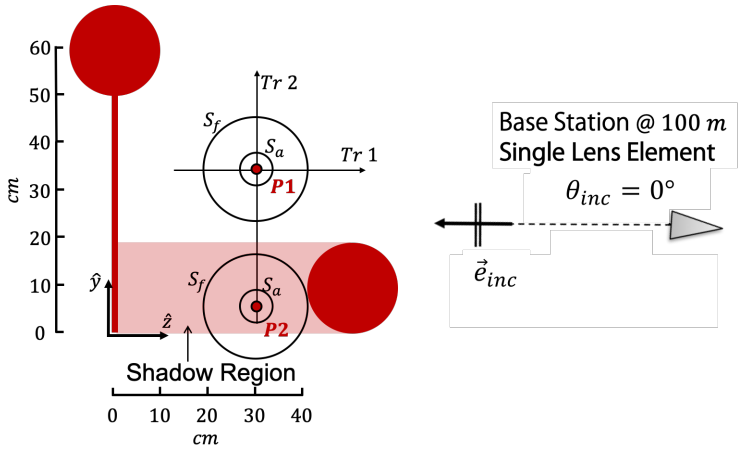

Figure 5.8: Geometry of the problem relevant to the area surrounding the user terminal antenna. Chosen reference system aligned with the direction of incidence of the LOS field. In red are the main scatterers: head and torso of the user under analysis, and head of the user in front. The red dots, P_1, P_2, indicate the two points where the observable field is evaluated. S_a indicates the antenna domain (sphere of radius $a = 3.5mm$), while S_f is the surface used to calculate the incident field spectrum (in this case $R_f = 70mm$). Tr1, Tr2, indicate the reference system used to evaluate the incident field maps and received power.

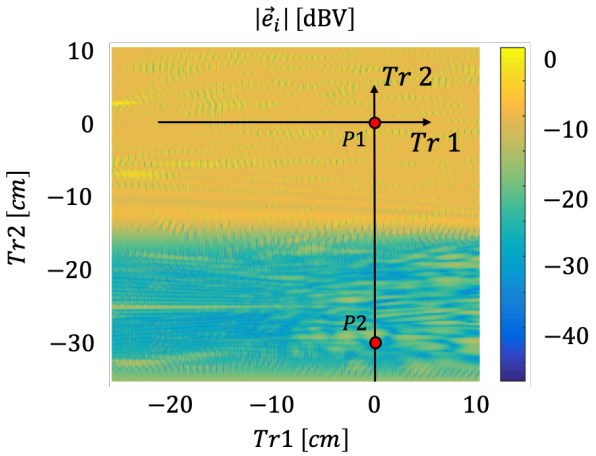

Figure 5.9: Incident field magnitude map at 120 GHz. The axes Tr1 and Tr2 are shown for the sake of completeness.

head and the torso of the spectator under analysis, and the head of the spectator in front. All of these objects are modelled as thick dielectrics, with a complex relative permittivity of $\varepsilon_r = 6 - j6$ at 120 GHz [62]. The surface of the scatterers is considered rough. The torso has a rms of 1mm, and a correlation length of 3.5cm along x and of 5cm along y, whereas the heads have a rms of 4.7mm, and a correlation length of 7cm along x and of 6cm along y. A Physical Optics tool [42] is used to calculate the scattered field.

The incident field on the surroundings of the antenna terminal is shown in Fig. 5.9 at 120GHz. The visible interference pattern with the LOS field is given by the reflection from the torso, which does not scatter a plane wave due to the rough surface. Moreover, the head of the neighbouring spectator creates a shadow region with respect to the LOS field from the base station.

Let us consider a terminal antenna characterised with an Airy pattern of 19dB directivity. This corresponds to the ideal antenna for a single plane wave in a sphere of radius 3.5mm as described in [52]. Fig. 5.10 shows the received power by this antenna oriented both with the broadside direction towards the base station and towards the torso. The figures show the results in both the axes Tr1 and Tr2 of Fig. 5.8. In this case, one can observe that along Tr1, the received power remains constant, since no significant fading effect is present due to the high terminal antenna directivity, and it is equal to the one evaluated via the Friis LOS formula. However, when the Airy pattern points towards the torso, as shown in the same figure, the received power is drastically reduced. A similar effect occurs at the beginning of the Tr2 axis, when the terminal antenna is located in the shadow region, see Fig. 5.8.

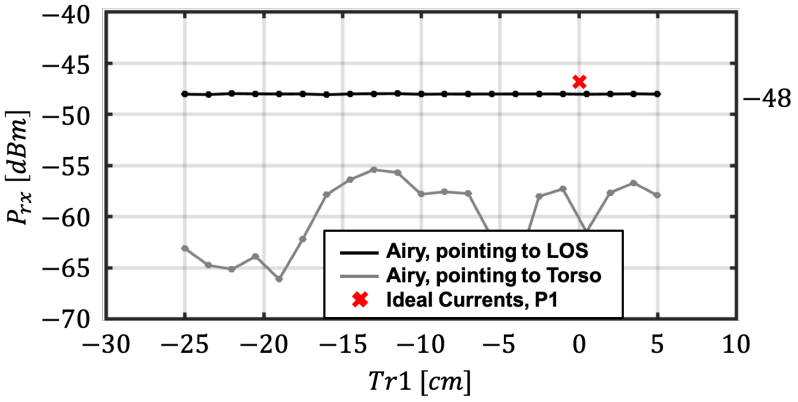

(a)

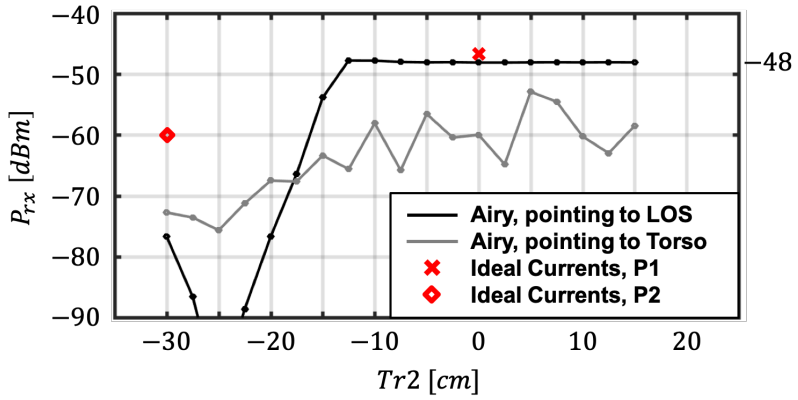

(b)

Figure 5.10: Power received by the 120GHz antenna terminal as a function of its position along the two axes of Fig. 5.8: (a) Tr1 and (b) Tr2. The red cross and square symbols indicate the available power given by the proposed Observable Field procedure in P_1 and P_2, respectively.

5.5 Multi-path driven antenna beamforming

To improve the coverage, the availability of a terminal antenna pattern with dynamic beam forming capabilities would be a great advantage. This is mostly possible at high frequencies where the terminal antennas can be made electrically large. In this case, the terminal's beam pattern can be changed by dynamically tuning amplitude and phase of the received signals with a coherent array of antennas. To maximise the received power, the array elements weights should be fine-tuned to synthesise the pattern radiated by the ideal currents.

For the stadium scenario presented in the previous section, the observable field, and its associated available power, have been calculated in two relevant points, shown in Fig.8: P1 where the LOS field is dominant, and P2 located within the shadow region. It is worth noting that the observable field is independent of the terminal orientation inside the antenna domain. For the sake of simplicity, let us consider a spherical volume of radius to evaluate the available power.

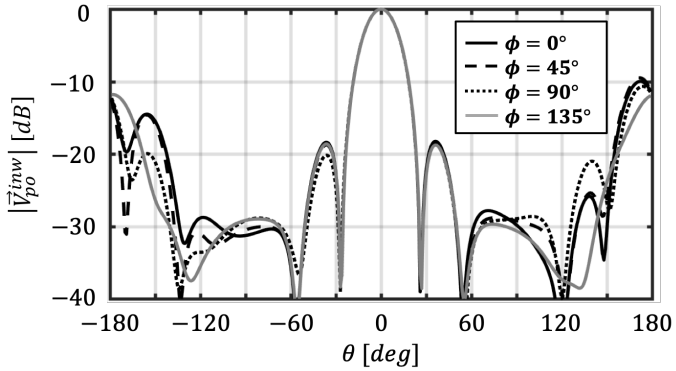

Figure 5.11: Normalised magnitude of the inward component of the observable field pattern for four different ϕ cuts in P1

Fig. 5.11 shows the inward component of the observable field calculated via the ideal currents procedure described in this chapter, associated to an antenna domain S_a, centred in P1. The pattern in Fig. 5.11 has two main beams: one along the direction of the LOS incident wave; the other, essentially due to the reflection from the torso, pointing at the user ($\theta = 180°$). The antenna should have a pattern as the one radiated by the ideal currents to receive the maximum power. Moreover,

the pattern should change dynamically as function of the terminal location. The realisation of such an antenna is out the scope of this work, and maybe limited by practical considerations.

The available power in P1 results $P_{ava,P1} = -47.2dBm$, only 1dB greater than the one calculated with an Airy pattern, see Fig. 5.10. This increment in the available power is due to the coherent sum of the LOS beam and the one associated to the field reflected by the torso, which is 10dB lower. Therefore, for $a = 1.4\lambda$, if the terminal is in a region where the incident field is dominated by the LOS, the required dynamic beam forming should essentially steer an Airy beam towards the LOS, and the torso contribution can be neglected.

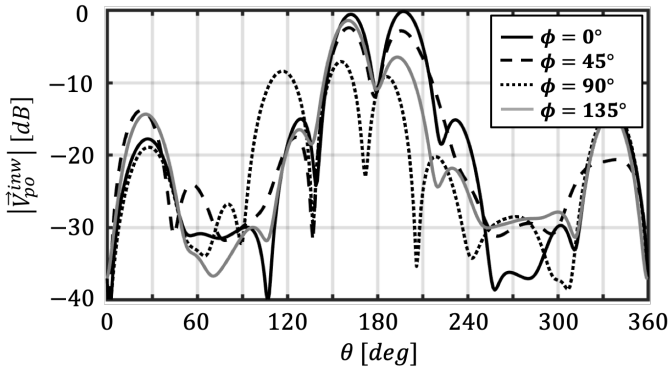

Figure 5.12: Normalised magnitude of the inward component of the observable field pattern for four different ϕ cuts in P2 at 120GHz. Note that to highlight the beam splitting around $\theta = 180°$ the field is plotted for $\theta = 0 \rightarrow 360°$

Fig. 5.12 shows the inward component of the observable field associated to the same antenna domain centred in P2. Since the scatterers dimensions and their roughness are not negligible in terms of the wavelength, the interference pattern created by the LOS, and the scattered field is complex. For the considered example, it is apparent that the main contribution is given by the scattering from the torso, and it is located around $\theta = 180°$. It is worth noting that there is a split in this main beam due to the torso roughness. A secondary contribution comes from the LOS direction, $\theta = 0°$, and it is due to the field scattered by the head of the spectator sitting in front of the user under analysis. The pattern of the ideal antenna is, in

this example, quite different from an Airy pattern.

The estimated power available in P2 is $P_{ava,P2} = -60dBm$, much higher than the one achieved by the terminal antenna described in the previous section (Airy pattern), which resulted only -76dBm when pointing towards the torso and -83dBm when pointing towards the base station, as shown in Fig. 5.10. Therefore, in case of LOS blockage the field scattered by the users can be received to improve the connection to the base station. In this case, the terminal antenna should have not only dynamic steering, but also shaping abilities.

For the sake of completeness Fig. 5.13 shows the magnitude and phase of the PWS (see Appendix D) of the incident field used to derive the observable field in the two previous examples at high frequencies. The PWS is evaluated on a sphere, S_f, of radius $R_f = 3cm$ enclosing the antenna domain, see Fig. 5.8. Fig. 5.13 (a) and (b) show the PWS when the receiver is located in P1. In this case, it presents a stationary phase point in the top sphere around $\theta = 0°$. Thus, the LOS field will be the dominant contribution to the integral in equation (5.7). For this reason, the relevant ideal currents shown in Fig. 5.14 (a) resemble those obtained for a single plane wave coming from $\theta = 0°$ (see Fig. 5.4 (a)). The inward component of the observable field will be thus similar to that of an Airy pattern, as shown in Fig. 5.11.

In P2, the main contribution is instead given by the field scattered from the torso, since the magnitude in the bottom sphere is close to the maximum, and around $\theta = 180°$ the phase is not highly oscillating. However, there is not a clear stationary phase point since the field scattered by a rough surface does not have a predominant direction of propagation. The ideal currents relevant to this case are shown in Fig. 5.14 (b). The current distribution is clearly different from that associated to an Airy pattern of Fig. 5.4 (a).

5.5.1 Spectral bandwidth

In this subsection, the observable field is investigated over a 10 GHz bandwidth, which is wider than the spatial channels proposed in the 120 GHz scenario of [63]. The proposed procedure is applied to different incident fields evaluated with the field transmitted by the base station varying now from 115GHz to 125GHz, while

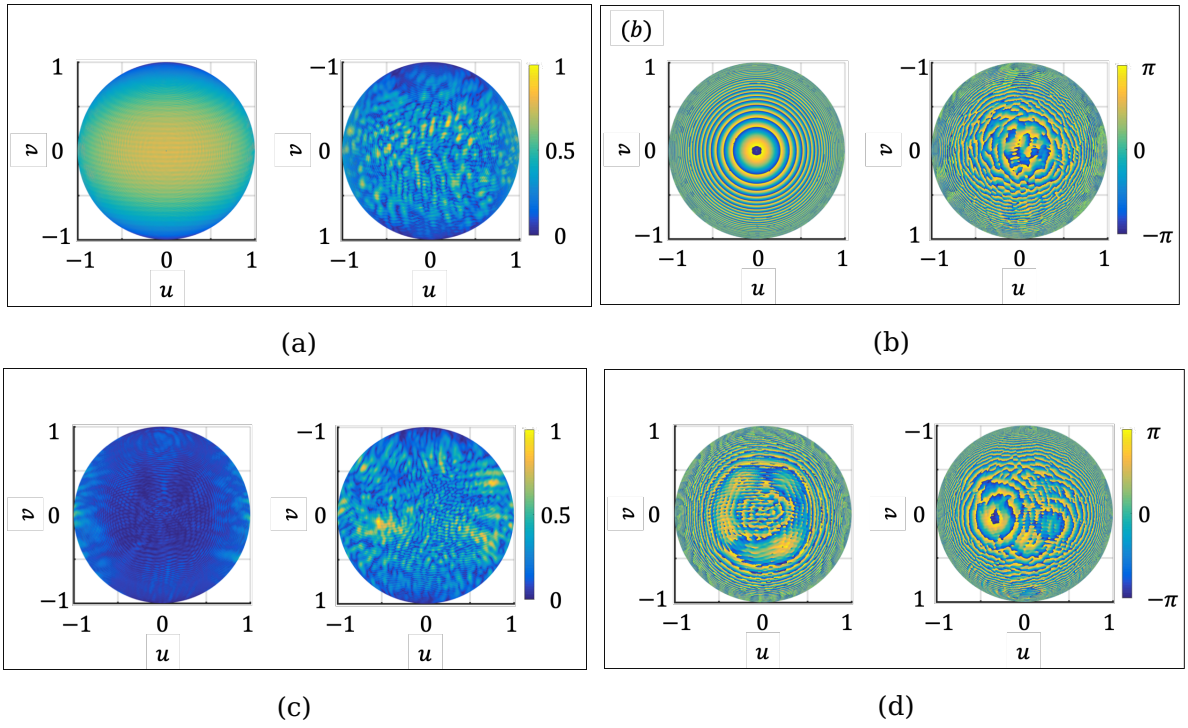

Figure 5.13: Normalised magnitude (a), (c) and phase (b), (d) of the y component of the PWS of the incident electric field at 120GHz when the terminal antenna is located in P1 (a) and (b), or in P2 (c) and (d). Top and bottom hemispheres are shown on the left and right, respectively.

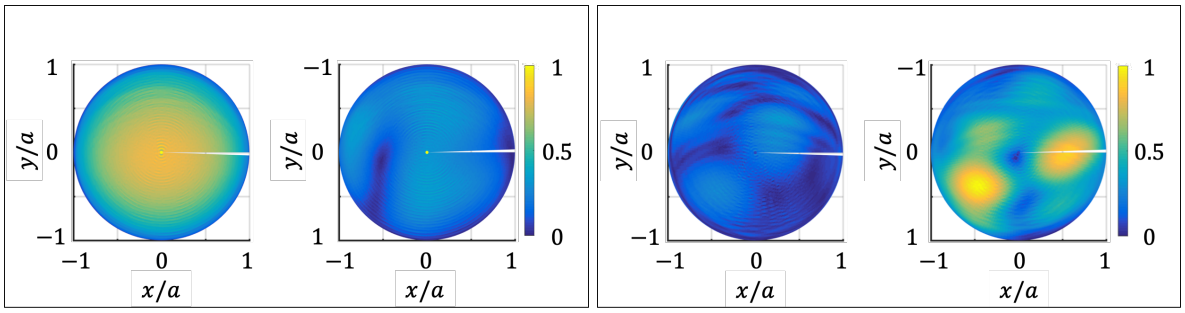

Figure 5.14: Normalised magnitude of the y component of the ideal electric currents at 120GHz when the antenna is located in P1 (a), and P2 (b). Top and bottom hemispheres are shown on the left and right, respectively.

keeping the same base station directivity. The inward component of the observable field at the extremes of the band is shown in Fig.5.16. It can be seen that even if small variations on the level of the multiple lobes are present, the shape of the ideal pattern is very similar. Therefore, the available power remains basically the same over the considered bandwidth, as shown in Fig. 5.17.

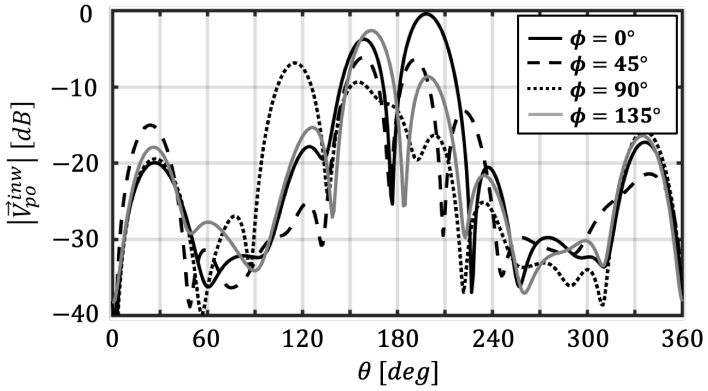

(a)

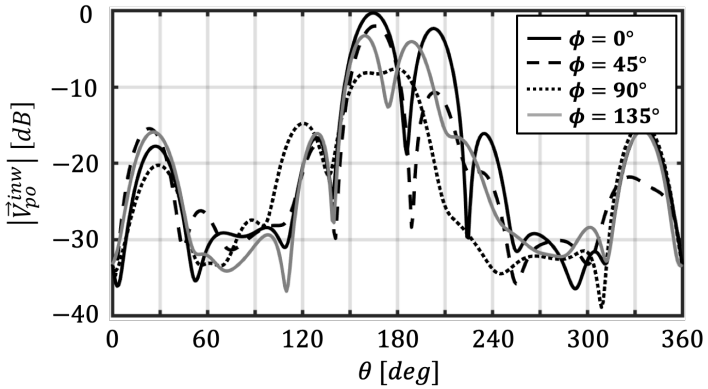

(a)

Figure 5.16: Normalised magnitude of the inward component of the observable field's pattern for four different ϕ cuts in P2 at 115GHz (a) and 125GHz (b). Note that to highlight the beam splitting around $\theta = 180°$ the field is plotted for $\theta = 0 \rightarrow 360°$

To be more realistic, we have also considered the case where the terminal antenna is in P2, and its pattern does not change over the considered spectral

band, i.e. it is frequency independent: Fig. 5.17 plots the received power by a terminal antenna with a frequency independent radiation pattern equal to the one of the observable field at 120 GHz, shown in Fig. 5.12. The received power is lower than that of the ideal terminal antenna in this case but remains within a 1.5 dB difference.

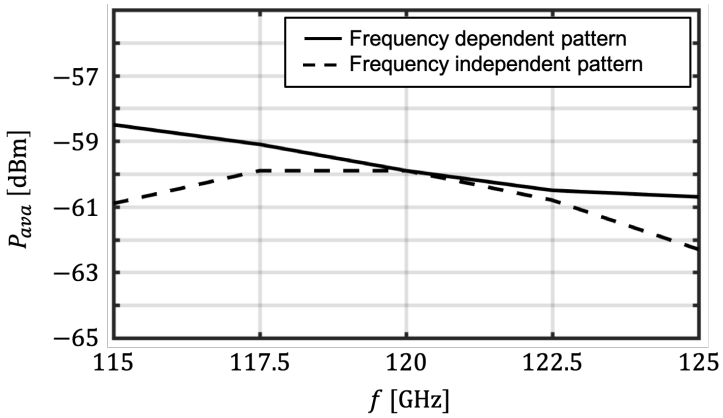

Figure 5.17: Available power as a function of the frequency in case of an ideal terminal antenna in P2 with a frequency dependent radiation pattern (solid black line), or with a frequency independent radiation pattern (dotted black line).

5.6 Conclusions

The observable field represents the portion of an arbitrary incident field that an ideal antenna, allocated in certain volume, can receive. Specifically, the ideal antenna operated in reception should scatter a field that is equal and opposite to the outward propagating wave portion of the observable field, so that the inward propagating portion is entirely absorbed.

This chapter introduces an operative procedure to approximate the observable field for generalised incidence cases: the outward component of the observable field has an angular distribution that is equal to the PO field radiated by equivalent currents defined on the truncated surface of the antenna domain. The amplitude of the observable field is instead obtained by exploiting the reciprocity theorem to project the incident field onto the PO field.

The observable field concept is then proposed as tool to synthesise the radiation pattern that maximises the power received by antennas immersed in complex scattering scenarios and thus illuminated by arbitrary fields. The procedure is applicable to any field but is especially beneficial in environments where the incident field is composed of multiple coherent planes waves, such as those present in sensing (*e.g.* communicating PCAs in TDSS systems) and communication (*e.g.* the example presented in this chapter) scenarios where the receiver is located close to multiple scatterers. In these situations, the knowledge of the amplitude, the phase, and the direction of incidence of the different contributions can be used to fine-tune the design of the receiving antenna pattern.

Chapter 6

Conclusions and Outlooks

The work presented in this thesis has been carried out over a period of roughly four years at the TeraHertz Sensing Group of the microelectronics department at the Delft University of Technology, the Netherlands.

The topics treated in the project lie in the field of THz technology, specifically in the analysis, design and testing of PCAs to be employed in the TDSS systems. The areas where such systems can be effectively exploited include the non-invasive inspection of different packaging, the study of biological samples and aid of medical diagnostics, non-destructive testing of pharmaceutical products as well as security screening.

It emerges from the literature the most of the efforts of the community are oriented towards the engineering of the photoconductive substrate over which the antenna is printed, with little focus on the antenna architecture. The work developed and presented in this thesis aims to bridge the gap between these two aspects of the PCA, offering a tool that predicts its behaviour including both the material parameters and the antenna radiation characteristics.

This chapter summarises the key points of the work, lists the most significant results and shows possible outlooks for its continuation.

6.1 Time domain model of PCAs

This work introduces a novel equivalent circuit in time domain that predicts the behaviour of photoconductive antennas subject to optical excitations of varying intensity. The model is constructed starting from a careful analysis of the physical processes involved in the induction of the current in a biased photoconductor excited by a pulsed laser, an equivalent circuit model in time domain including the antenna response is then derived; the model can be then transformed in the frequency domain in order to include the electromagnetic features of the device such as the antenna impedance and the quasi-optical channel efficiency. The procedure is applicable to any kind of antenna, given the parameters of the materials and details of the architecture.

The model consists in a simple Norton equivalent circuit, and an equivalent Thevenin, that estimates the temporal evolution of both the photocurrent flowing across the gap of the PCA and the transient voltage across it, while including the parameters of the photoconducting material as well as of the laser exciting it. The time-evolving photocurrent can be then translated into the spectral domain to operate with the radiation characteristics of the antenna and the efficiency of the quasi optical path guiding the radiation.

The equivalent circuit gives a clear picture of what concurs in the generation of the emitted THz field and what limits it, such as radiation field screening effects. It also allows to analyse the entire power budget of the system, from the laser exciting the transmitter to the field captured by the receiver, while accounting for all the characteristics of the optical signal, the semiconductor, the antenna architecture and radiation pattern and the quasi optical channel.

An especially relevant aspect of the proposed model lies in that accounting for saturation phenomena it predicts the power radiated by PCAs accurately even in case of large optical excitations with outstanding accuracy, where previous models failed. It appears that the saturation emerging under high laser power levels is given by the radiation of the antenna, whose near field opposes the bias applied across its terminals.

The hereby introduced procedure aims at bridging the gap between the pure material engineering and the antenna engineering, serving as a tool to analyse the

behaviour of PCA's and to evaluate the power budget of the entire link, from the excited semiconductor of the transmitter to the power detected by the receiver.

6.2 Theory and measurements: characterisation of a bow tie and a leaky wave PCA

In order to assess the validity of the model presented in this thesis a campaign of measurements is undertaken to characterise two photoconductive lens antennas: one presenting a slotted bow-tie geometry, one presenting a similar geometry but exploiting the leaky wave phenomenon, thanks to the introduction of an electrically small air gap between the substrate and the HR lens.

In both cases the laser source adopted is part of the TERA K15 from Menlo Systems GmbH; the parameters of the laser beam can be found in Table 2.1. For each antenna it has been implemented an *ad-hoc* laser delay that guides the optical excitation and focuses it onto the PCA gap. The PCAs are excited by varying laser power while being biased at different voltage potentials, and the acquired power is compared against the prediction of the model presented in Chapter 2: in both cases the equivalent circuit is able to track the behaviour of the antennas with great accuracy.

6.2.1 Bow tie PCA

To characterise the bow tie PCA, the antenna is position in place of the in-fibre fed transmitter native to the TERA K15. In order to synchronise the transmitting bow tie PCA and the receiver of the TERA K15 a 390cm free space optical delay line is built; at the end of the line the beam is focused down to match the gap using a polymer lens.

After a precise alignment procedure, the power radiated by the bow tie PCA excited by different optical and biasing conditions is acquired and compared to the predictions of the model: the antenna radiation impedance, its beam pattern and the efficiency of the quasi optical channel guiding the radiation are extracted from both commercial EM and in-house software. The LT GaAs carrier scattering time

is the only unknown: a value of 8.5 fs, in line with ranges found in the literature [18], lead to an outstanding agreement between the measurements and the results from the equivalent circuit, with differences lying within only 1dB. The saturation of the radiated power is very well accounted for from the model, and is ascribed to screening phenomena induced by the field radiated by the PCA itself, which tends to counteract the biasing field applied over its gap.

Next, after further alignments and synchronisation, the time evolving pulse radiated with the bow tie PCA under test is acquired with the receiver of the TERA K15, and its spectrum is calculated. The gathered data are also tested with the equivalent circuit. The agreement is good, even though heavily influenced by the response of the Auston switch adopted as receiver by the TERA K15, whose efficiency is rather poor below 250GHz and whose polarisation results frequency dependent. Also, to simplify the circuit derivation, the response of the bow tie PCA is approximated as instantaneous

6.2.2 Leaky lens PCA

While the bow tie is a common architecture, it is the first time that a leaky wave lens antenna is adopted as PCA and tested in a TDSS setup. To characterise the antenna, a 40cm free space optical delay line is built; at the end of the line the beam is focused down to match the gap using an off-axis gold parabolic mirror.

After a precise alignment procedure, the power radiated by the bow tie PCA excited by different optical and biasing conditions is acquired and compared to the predictions of the model: the antenna radiation impedance, its beam pattern and the efficiency of the quasi optical channel guiding the radiation are extracted from both commercial EM and in-house software. The LT GaAs carrier scattering time is the only unknown: a value of 8.5 fs, same as for the bow tie PCA and in line with ranges found in the literature, lead to an outstanding agreement between the measurements and the results from the equivalent circuit, with differences lying around only 1dB. The saturation of the radiated power is very well accounted for from the model, and is ascribed to screening phenomena induced by the field radiated by the PCA itself, which tends to counteract the biasing field applied over its gap.

Given the larger radiated power for the same excitation and biasing conditions compared to the bow tie PCA, the novel leaky wave PCA presented in this thesis stands out as an excellent candidate for time domain sensing and spectroscopy systems. Indeed, the dynamic range of such systems is highly dependent on the power radiated by the TX PCA and its coupling with the QO channel. The adoption of optical fibres to excite the photoconductive device would make the system more compact as well as easier to transport and maintain, without the need of cumbersome free space laser delay lines. This is indeed the solution generally chosen by commercial systems, which used with the leaky wave PCA presented here allow for larger levels of THz radiated power, and thus larger dynamic ranges.

6.3 The observable field

Nowadays, there are many applications, such as time-domain sensing, radar systems, wireless communications, and automotive applications, where the receiving antenna is immersed in a complex environment, and the incident field cannot be represented with a single plane wave. In such complex scenarios, it is useful to *a priori* understand what the theoretical maximum power that can be received by a lossless antenna is. In fact, this knowledge allows to evaluate the margin of improvement that could be expected when a complex antenna system is exploited.

The observable field is defined as the portion of a general incident field that can contribute to the signal received by an antenna occupying a fixed spherical volume. In particular, the incident field is expressed as a superposition of homogeneous plane waves distributed over a spherical surface via its plane wave spectrum.

The observable field in the far field region is expressed as the product of a normalised spherical wave and an amplitude, both functions of the incident field and the antenna domain. Specifically, the observable field is represented as the sum of an inward and an outward propagating wave. The inward/outward component of the observable field has an angular distribution that is equal to the PO field radiated by equivalent currents defined on the truncated surface of the antenna domain. The amplitude of the observable field is instead obtained by exploiting the reciprocity theorem to project the incident field onto the PO field.

An ideal antenna operated in reception should scatter a field which is equal but

opposite to the outward propagating wave of the observable field cancelling it out. In other words, the ideal antenna absorbs the entire inward propagating power of the observable field.

The methodology is applicable to any field, and results especially beneficial in environments where the incident field is composed of multiple coherent planes waves, such as those present in sensing (e.g. communicating PCA's in TDSS systems) and communication (e.g. the example presented in this chapter) scenarios, with receivers located close to multiple scatterers. In such situations, the knowledge of the amplitude, the phase, and the direction of incidence of the different contributions can be used to fine-tune the design of the receiving antenna pattern.

6.4 Future outlooks

A proper modelling of the behaviour of a PCA, from the physical phenomena concurring in the photocurrent generation to the characteristics of the consequent radiation, leads to a better understanding of the device operation. Not only does this allow for better designs, it also highlights all the potential advantages of the conjunct engineering of both the antenna architecture together with the material. This opens much room for improvements:

- It is apparent that for broad band antennas, such as the bow tie PCA, to assume the impulse response as instantaneous represents a good approximation, which greatly simplifies the solutions of the model. Instead, in case the antenna radiation impedance presents a less stable behaviour with a non-negligible reactive component, an more accurate evaluation of the time domain impulse response of the antenna would result in a better estimation of the temporal evolution of the current signal and its radiation. The impulse response would appear in the equivalent circuit as an integral relation in place of the approximated load r_a.

- The saturation of the power radiate by the leaky wave PCA as a function of the optical excitation happens much faster than in the bow tie PCA; this is mainly given by its larger radiation impedance. However, the 2 μm membrane is mechanically fragile, and possibly other higher order effects which are not

accounted for should be considered; these effects might be joule heating, multiple reflections in the membrane and the absence of current in the bulk, to name a few. This might be worth looking into.

- To make two identical either bow tie or leaky wave PCA communicate as transmitter and receiver in the TDSS set up of chapter 3 is an important step to take in order to increase the dynamic range of the system significantly. Indeed, these antennas radiate much more efficiently than the Auston switches adopted by the TERA K15. Moreover, their radiation characteristics are known, and can thus be deconvoluted from the measured time domain pulse.

- To use more efficient PCAs with good coupling under the same biasing and excitation leads to detected pulse of much larger amplitude, which in turn translates into higher signal to noise ratios. This is of great relevance, as higher signal to noise ratios mean faster and cheaper TDSS systems, as shorter integration times are needed to detect the wanted signals.

6.5 Research Output

The work presented in this paper has led to a number of publications, as listed in the Chapter 'List of publications' at page 143. A total of 4 peer review journal papers are published, under review or in preparation, along with 9 conference publications. Specifically, the work in Chapter 2 and 3 is under review for a paper for the IEEE Transaction on Antennas and Propagation. The content of Chapter 4 is part of a paper in preparation for the IEEE. The content of Chapter 5 is published in a paper for the IEEE Transaction on Antennas and Propagation, and was nominated for the *Best Student Paper Award* in the European Conference on Antennas and Propagation (EuCAP), Krakow, Poland, 2019.

Appendix A

Amplitude of the optical excitation

The temporal evolution of the carrier density function in the active volume of a photoconductor depends on the characteristics of the laser exciting it as well as the properties of the material. The generation of charge particles is induced by modulated laser pulses, and following a similar procedure than [28] is expressed as:

$$g_{gen}(t,\vec{r}) = \frac{P_0}{hf_c}\left(1-|\Gamma|^2\right)\frac{e^{\frac{\rho^2}{2\pi\sigma_\rho^2}}}{2\pi\sigma_\rho^2}\frac{d}{dz}e^{-\frac{|z|}{\alpha}}e^{-4ln2\frac{t^2}{\tau_p^2}} \tag{A.1a}$$

$$P_0 = \tilde{P}_L\frac{T_L}{\tau_p}\sqrt{\frac{4ln2}{\pi}} \tag{A.1b}$$

where $\hat{\rho} = \hat{x}+\hat{y}$ is the observation point in the horizontal plane $z=0$, P_0 is the laser peak power, $\tilde{P}_L$ the laser average power, $\sigma_\rho = \frac{D_L}{2\sqrt{2ln2}}$, D_L is the laser pulse vector -3dB diameter. In general, the carrier generation function is in general different for every observation point; thus, in order to simplify the analysis and get rid of the spatial dependence, it is convenient to average the generation function in the whole active volume:

$$\bar{g}_{gen}(t) = \frac{1}{Vol}\int_{-\frac{W_x}{2}}^{\frac{W_x}{2}}\int_{-\frac{W_y}{2}}^{\frac{W_y}{2}}\int_{-W_z}^{0} g_{gen}(t,\vec{r})dzdydx = Ag_{gen,N}(t) \tag{A.2}$$

where $Vol = W_xW_yW_z$, and:

$$A = \frac{P_0}{hf_c}\frac{\left(1-|\Gamma|^2\right)}{2\pi\sigma_\rho^2}\frac{1}{Vol}\int_{-\frac{W_x}{2}}^{\frac{W_x}{2}}\int_{-\frac{W_y}{2}}^{\frac{W_y}{2}}\int_{-W_z}^{0} e^{\frac{\rho^2}{2\pi\sigma_\rho^2}}\frac{d}{dz}e^{-\frac{|z|}{\alpha}}dzdydx \tag{A.3a}$$

$$g_{gen,N}(t) = e^{-4ln2\frac{t^2}{\tau_p^2}} \tag{A.3b}$$

Equation (A.2) is useful to express the complete carrier generation function as the product of the normalised Gaussian temporal envelope and an amplitude.

Next, an optical efficiency is defined, η_{opt}, in order to obtain a more compact expression for the amplitude:

$$A = \frac{P_0}{hf_c}\frac{\left(1-|\Gamma|^2\right)}{2\pi\sigma_\rho^2}\frac{1}{Vol}C \tag{A.4a}$$

$$C = \int_{-\frac{W_x}{2}}^{\frac{W_x}{2}}\int_{-\frac{W_y}{2}}^{\frac{W_y}{2}}\int_{-W_z}^{0} e^{\frac{\rho^2}{2\pi\sigma_\rho^2}}\frac{d}{dz}e^{-\frac{|z|}{\alpha}}dzdydx \tag{A.4b}$$

In general the solution of equation is calculated numerically. However, if $D_L = W_x = W_y$, this efficiency will have an analytical solution, $C = 2\pi\sigma_\rho^2\eta_{SO}\left(1-e^{-\frac{W_x}{\alpha}}\right)$, where $\eta_{SO} = 0.58$. When this condition is verified the amplitude results:

$$A = \eta_{opt}\frac{\tilde{P}_L}{hf_c}\frac{T_L}{\tau_p}\sqrt{\frac{4ln2}{\pi}}\frac{1}{Vol} \tag{A.5a}$$

$$\eta_{opt} = \eta_{SO}\left(1-|\Gamma|^2\right)\left(1-e^{-\frac{W_x}{\alpha}}\right) \tag{A.5b}$$

Where the overall optical efficiency η_{opt} is a design parameter, and ideally $\eta_{opt} = 0.35$.

Appendix B

Thevenin equivalent circuit in time domain

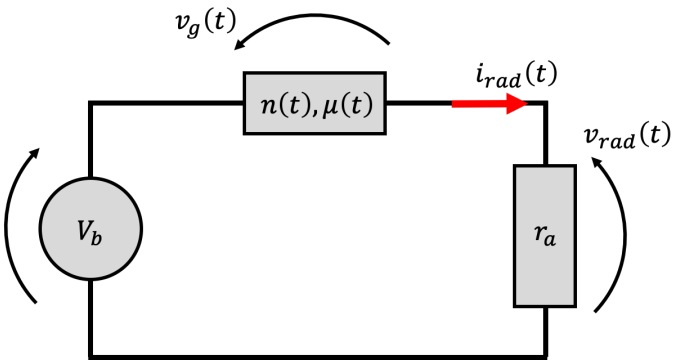

Figure B.1: Equivalent circuit in time domain consisting in a constant voltage source (*i.e.* the bias), V_b, a component representing the excited PCA gap, $n(t), \mu(t)$, and a component representing the effect of the antenna radiation, r_a

A Thevenin equivalent circuit representing the problem under investigation is shown in Fig. B.1. The component representing the excited PCA gap, (2.9), appears here as a component in series with a load, which represents the antenna response. The equivalent generator is the constant voltage bias, V_b, applied at the antenna terminals.

To properly represent the effect of the antenna in time domain, the impulse response of the architecture should be included. However, electrically long, broad-

band antennas have impulse responses can be approximated as Dirac's deltas, when one neglects late time reflections from the edges. For these configurations it is then legitimate to represent the load as a real radiation resistance, and the field radiated by the antenna as a voltage drop across the load. The total voltage across the gap of the PCA is thus affected both by the bias and the generated radiation:

$$v_g(t) = V_b - v_{rad}(t) \tag{B.1}$$

To solve the circuit and substitute equation (B.1) in (2.9) leads to a system of two equations and two unknowns, $(i_{rad}(t), v_{rad}(t))$, that can be solved numerically:

$$i_{rad}(t) = q_e \frac{W_y W_z}{W_x} \int_{-\infty}^{t} n_p(t, t'') \int_{t''}^{t} \mu(t - t') \left(V_b - v_{rad}(t')\right) dt' dt'' \tag{B.2a}$$

$$v_{rad}(t) = i_{rad}(t) r_a \tag{B.2b}$$

For the sake of simplicity, the begin of the laser pulse is set at $t'' = 0$. The system is identical to the one in (2.11).

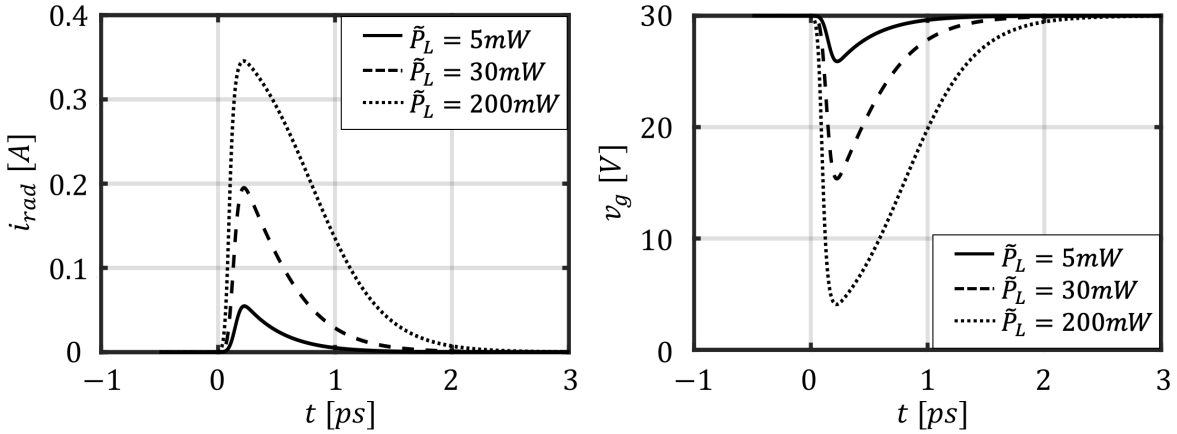

Figure B.2: Temporal evolution of current, $i_{rad}(t)$, and voltage, $v_g(t)$, across the photoconductive gap for a bias voltage of $V_b = 30V$, a radiation resistance of $r_a = 75\Omega$, a scattering time of $\tau_s = 8.5fs$, an optical efficiency of $\eta_{opt} = 0.35$ and three different optical excitation $\tilde{P}_L$.

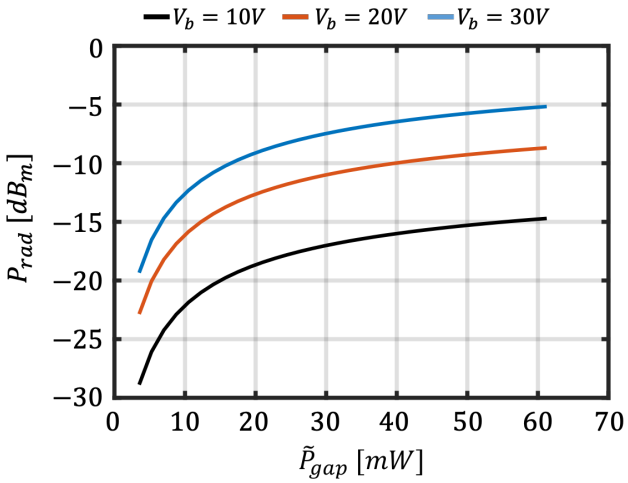

Figure B.3: Power radiated by the load, r_a, as a function of the average laser power absorbed by the gap, $\tilde{P}_{gap} = \eta_{opt}\tilde{P}_L$, with $\eta_{opt} = 0.35$, for three different bias voltage, $V_b = 10, 20, 30V$.

The representation of the time domain circuit of Fig. B.1 is typical of Thevenin equivalent circuits, and similar to other circuits found in literature, such as in [27]. In this case, it offers a clear physical insight into the field screening induced by the radiation generated by the antenna, responsible for the saturation that occurs for high optical excitations. Indeed, when the laser pulse is not active ($t < 0$), there are no free charge particles ($n_p(t < 0, t'') = 0$) and no current flows in the circuit ($i_{rad}(t < 0), v_{rad}(t < 0) = 0$). When the pulse hits the PCA gap and injects free carriers into the conduction band ($t \geq 0$), a current starts flowing ($i_{rad}(t \geq 0) \neq 0$), and the radiation it induces is represented in the circuit through a voltage drop across the load ($v_{rad}(t \geq 0) \neq 0$); this drop effectively reduces the gap voltage, $v_g(t) = V_b - v_{rad}(t)$. Once the pulse ends, the photocarriers are progressively reabsorbed, the radiation stops and the circuit returns to its initial state ($i_{rad}(t), v_{rad}(t) = 0$).

Fig. B.2 shows the temporal evolution of the radiation current and the PCA gap voltage predicted by the circuit for three different laser power levels arriving at $t'' = 0$, a bias of $V_b = 30V$, and an antenna radiation impedance of $r_a = 75\Omega$; the material and laser parameters are given in Table 2.1. It is important to stress the fact that not only does a linear increase of the optical excitation not lead to a

corresponding increase in amplitude, it also modifies the time signature of both the current and the voltage on the gap.

After having solved the circuit and calculated the induced photocurrent, the power radiated by the feed, r_a, is evaluated as:

$$P_{rad}(f) = \frac{2}{T_L} \int_0^\infty r_a \left| I_{rad}(f) \right|^2 df \tag{B.3}$$

Fig. B.3 shows the power radiated by the feed, r_a, predicted by the equivalent circuit of Fig. B.1 as a function of the average laser power absorbed by the gap, $\tilde{P}_{gap} = \eta_{opt} \tilde{P}_L$, for three different bias voltage, $V_b = 10, 20, 30V$. As discussed in Appendix A the ideal optical efficiency adopted to produce these results is $\eta_{opt} = 0.35$. The power radiated by the antenna saturates as one increases the optical excitation level: this is the mark of the radiation field screening caused by the generated radiation.

To choose between the Thevenin (Fig. B.1) and Norton (Fig. 2.2) representation is up to one own's preference, as the two tools provide identical results.

Thevenin equivalent circuit the Thevenin representation offers a clear visual picture of the feedback of the antenna on the induced photocurrent: indeed, the EM field radiated from the antenna effectively reduces the voltage applied at the terminals of the device gap. The stronger the excitation, $\tilde{P}_L$, the stronger the photocurrent, $i_{rad}(t)$, the stronger the radiation, $v_{rad}(t)$, and the stronger the reduction of the voltage that accelerates the photocarriers, $v_g(t) = V_b - v_{rad}(t)$. Moreover, the equivalent circuit is close to the actual architecture of the device, with the bias source in series with the excited PCA gap and the antenna.

Norton equivalent circuit the Norton representation is slightly more complicated to construct. However, it has a validation based on the equivalence theorem in [34]. Also, it needs to be said that the inversion from Norton to Thevenin is not immediate, as the relation between source and impedance consists in a double convolution, so the validation in [34] is not necessarily valid for the Thevenin circuit.

Appendix C

Enhanced leaky wave PCA transmitter fabrication

The fabrication of the leaky-lens antenna is always done on a suspended membrane of semiconductor which, in the present case, consist of a thin layer of photoconductive low-temperature grown GaAs. Several previous works show that dry (*i.e.* plasma) etching has an intrinsic limitation in the maximum etched depth, thus setting the minimum membrane thickness to few hundreds of micrometers. This is due to the fact that Ga fluoride, chloride and bromide, generated as by-products of etching reactions, present very high vapour pressures. The etching is then strongly limited by their desorption from the surface and, as a consequence, it is extremely hard, if not impossible, to etch hundreds of microns-thick GaAs substrates. Alternatively, [2] shows that deeper GaAs trenches can be etched by means of wet etches base on citric acid.

For the procedure adopted in this work a dedicated selective wet etch based on NH4OH/H2O2 mixtures has been developed. The wet etching of GaAs in NH_4OH/H_2O_2 mixtures is highly crystallographic, as the relative etch rate of the crystalline planes follows this order: $[111]_{\text{As rich}} > [100] > [110] > [111]_{\text{Ga rich}}$ [64]. The specific etching ratio depends on the specific NH_4OH/H_2O_2 ratio [65]. Because of this etch rate difference, the walls of the membrane cavity assume a tapered shape, although it is not relevant for the properties of the devices in analysis. The etching method is similar to the one reported in [66], where the authors employ a citric acid/H_2O_2 mixture instead. However, in the present case, the etching is

dramatically faster, taking ∼1.5 hours instead of ∼20 hours.

The leaky wave PCA is manufactured from a 3 inch diameter and 525μm thick semi-insulating (SI) single-crystalline GaAs wafer, as in Fig. 3.2 (a). A multilayer consisting of 0.2μm thick GaAs, 0.4μm thick $Al_{0,75}Ga_{0,25}As$ and 2μm thick LT-GaAs is deposited by Molecular Beam Epitaxy (MBE) on the front side of the SI-GaAs wafers (see multilayer cross section in Fig. III-1). The GaAs layer serves as a buffer layer to accommodate the growth of the $Al_{0,75}Ga_{0,25}As$ film, which acts as the sacrificial etch-stop layer for the membrane release process.

The LT-GaAs layer constitutes the active photo-conductive substrate of the membrane for the leaky wave lens antenna. These layers are grown by the University of Leeds. The back side of the wafer as received from the foundry is rough; for this reason polishing is necessary, in order to obtain a uniform and constant etching during the membranes release over the back surface. The polishing ensures that the different crystal facets of the rough surface are smoothened out, making the crystallographic nature of the bulk etching less of a risk for etch stop of non-homogeneity.

The fabrication of the leaky lens antenna chips is performed at the Else Kooi Laboratory of the Delft University of Technology. The fabrication process starts with the cleaning of the wafer from organic contamination, removal of the LT-GaAs native oxide and chemical polishing of the wafer back side. The cleaning and removal of the native oxide is done by soaking the wafer at room temperature in acetone first, then in isopropanol and finally in NH4OH (28% bath). The wafer back side polishing is performed by immersing the wafer in a NH_4OH (28%) and a H_2O_2 (31%) bath mixed at a 1:2 volume ratio at room temperature for 5 minutes. After this procedure the back of the wafers is inspected under a microscope to be sure that it results smooth and optically polished. The wafer is afterwards soaked in NH_4OH (28%) for 5 minutes.

Next, a 3μm thick, low temperature, plasma enhanced chemical vapour deposited (PECVD) SiO_2 layer, with a compressive stress $<$150MPa is deposited on the back of the wafer. This SiO_2 layer will be patterned later in the process to define the future location of the membranes.

The antenna metallization layer is realised through DC sputtering at room temperature. A 1μm thick aluminium (99,999% purity) layer is deposited on top of

native oxide-free LT-GaAs surface in an Ar atmosphere. The LT-GaAs native oxide is stripped dipping the wafer in a NH_4OH (28%) solution at room temperature for 4 minutes just before the deposition. The deposition at room temperature serves to avoid any uncontrolled annealing and/or inter-diffusion induced variation of the LT-GaAs electrical properties.

Later, the Al is patterned to realise the desired antenna geometry as well as the pads for the biasing of the structure. The Al is etched by a double-step etching (first dry etching and a soft wet landing) to maintain intact the pristine LT-GaAs surface quality, important for the charge carriers recombination at the surface and the overall mechanical stability of the LT-GaAs membrane. The etching of the first 0.8-0.9μm is done in an inductively coupled plasma reactive ion etching (ICP-RIE) reactor, using a Cl_2/HBr gas mixture and photo-resist as the mask. The remaining 0.1-0.2μm of Al are later removed by wet etching in diluted (10% vol.) NH_4OH, which, contrary to the Cl-based RIE, is harmless for the LT-GaAs surface.

A 2.6μm thick layer of Cytop [35], a transparent fluoropolymer with a refractive index of 1.34 that does not affect the laser absorption in the gap of the antenna, is spin coated on the front side of the wafer and cured on a hot plate (30min at 80° first and then 1h at 200°) in air. The Cytop layer is patterned, with photoresist as mask, by plasma etching in a RIE reactor with O_2 gas to expose the antenna Al contact pads for wire bonding. The Cytop coating and etching do not have any impact on the LT-GaAs and Al properties, yet it protects the PCA surface from external agents adsorption (*e.g.* moisture) while providing mechanical support to the LT-GaAs membrane.

The LT-GaAs membrane is fabricated with a double-step wet etching of the SI-GaAs substrate using, subsequently, two NH_4OH/H_2O_2 mixtures. HF-patterned low-T PECVD SiO_2 film is adopted as the hard mask on the wafer backside. During the whole wet etching process, the LT-GaAs side is protected from the aggressive chemical solutions using a PEEK holder from A.M.M.T. [67]. The first etching step is done soaking the wafer in a solution of NH_4OH (28% vol.) and H_2O_2 (31% vol.), mixed at a volume ratio of 1:2. This is the same solution used to polish the back side of the wafer. The etch rate of this solution is $\sim 8\mu m/min$, and is able to remove the major portion of the substrate much faster than the citric acid solution.

An important point to take into consideration is that some etching reaction

products, such as $Ga(OH)_3$, are not very soluble in water [66], and they tend to form a reaction-limiting stain on the surface under etching. Thus, it is necessary to constantly stir the solution to have a uniform etching of the GaAs substrate. However, as reported in [65], this mixture is not selective with any AlGaAs alloy. Therefore, the last $50\mu m$ of the substrate are etched using a volume ratio of 1:30. This solution has an etch rate of $\sim 2\mu m/min$, roughly four times slower than the previous one, though showing a great selectivity for the $Al_{0,75}Ga_{0,25}As$ layer (etching ratio of at least 100 [65]). Indeed, when the relative amount of the peroxide is that high, the etching of $Al_{0,75}Ga_{0,25}As$ is slowed down by the formation of quasi-passivating Al oxide [65]. The $Al_{0,75}Ga_{0,25}As$ layer is eventually removed, together with the SiO_2 mask, by soaking the wafer in buffered (1:7) HF at room temperature for 20 minutes, process that is harmless for the LT-GaAs layer.

Appendix D

Plane wave spectrum

The aim of this appendix is to propose a procedure to derive a homogeneous plane wave expansion of a general incident field, valid in the surrounding of a chosen origin. The proposed procedure relies only on the knowledge of the incident field on a sphere of radius R_f centred in the origin.

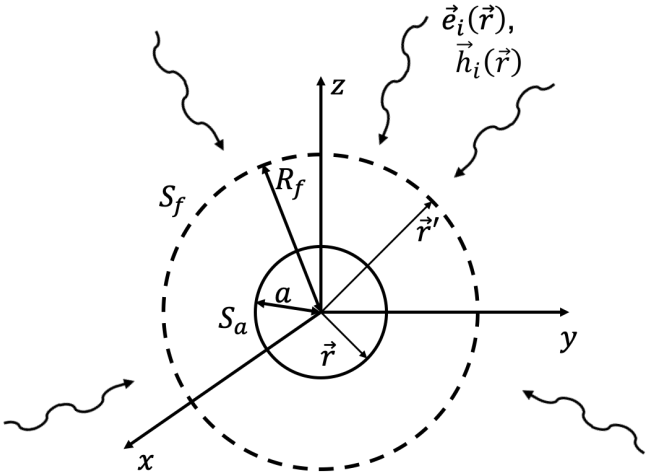

Figure D.1: Geometry of the problem

Resorting to the equivalence theorem, the electric field inside S_f can be expressed as the radiation integral due to the equivalent currents:

$$\vec{j}_{eq}(\vec{r}') = -\hat{r}' \times \vec{h}_i(\vec{r}') \tag{D.1a}$$

$$\vec{j}_{eq}(\vec{r}') = -\hat{r}' \times \vec{h}_i(\vec{r}') \tag{D.1b}$$

where $|\vec{r}'| = R_f$.

The electric field can be expressed as the sum of the contributions due to the equivalent electric and magnetic currents, *i.e.* $\vec{e}_i(\vec{r}) = \vec{e}_i^{\,j}(\vec{r}) + \vec{e}_i^{\,m}(\vec{r})$. Each contribution can be evaluated resorting to the dyadic Green's function of an unbounded homogeneous medium as follows:

$$\vec{e}_i^{\,j}(\vec{r}) = -j\omega\mu \iint_{S_f} \left(\overline{\overline{I}} + \frac{\vec{\nabla}\vec{\nabla}}{k^2} \right) \frac{e^{-jk\left|\vec{r}-\vec{r}'\right|}}{4\pi\left|\vec{r}-\vec{r}'\right|} \cdot \vec{j}_{eq}(\vec{r}')d\vec{r}' \tag{D.2a}$$

$$\vec{e}_i^{\,m}(\vec{r}) = -\iint_{S_f} \vec{\nabla} \frac{e^{-jk\left|\vec{r}-\vec{r}'\right|}}{4\pi\left|\vec{r}-\vec{r}'\right|} \times \vec{m}_{eq}(\vec{r}')d\vec{r}' \tag{D.2b}$$

By making use of the addition theorem for the Legendre Polynomials (§7.5 of [68]) one obtains:

$$\frac{e^{-jk\left|\vec{r}-\vec{r}'\right|}}{4\pi\left|\vec{r}-\vec{r}'\right|} = -\frac{jk}{4\pi} \oiint_U e^{j\vec{k}_q\cdot\vec{r}} T_L(\vec{k}_q, \vec{r}')d\hat{k}_q \tag{D.3}$$

where U is the unit sphere (*i.e.* the Ewald sphere), $d\hat{k}_q = sin\alpha d\alpha d\beta$, and the translation operator:

$$T_L(\vec{k}_q, \vec{r}') = \sum_{l=0}^{L} (-j)^l (2l+1) h_l^{(2)}(kr') P_l(\hat{r}\cdot\hat{k}_q) \tag{D.4}$$

being P_l the Legendre polynomial, and $h_l^{(2)}$ the spherical Hankel function of the second kind of order l. The previous expression can be rewritten as superposition of homogeneous plane waves, as follows:

$$\vec{e}_i^{\,j}(\vec{r}) = -\frac{\zeta k^2}{(4\pi)^2} \iint_U \left(\overline{\overline{I}} - \hat{k}_q\hat{k}_q \right) \cdot \vec{\tilde{S}}_L(\vec{k}_q) e^{j\vec{k}_q\vec{r}} d\hat{k}_q \tag{D.5a}$$

$$\vec{e}_i^{\,m}(\vec{r}) = -\frac{k^2}{(4\pi)^2} \iint_U \hat{k}_q \times \vec{\tilde{Q}}_L(\vec{k}_q) e^{j\vec{k}_q\vec{r}} d\hat{k}_q \tag{D.5b}$$

where $\vec{\tilde{S}}(\vec{k}_q) = \iint_{S_f} T_L(\hat{k}_q, \vec{r}')\vec{j}_{eq}(\vec{r}')d\vec{r}'$, and $\vec{\tilde{Q}}_L(\vec{k}_q) = \iint_{S_f} T_L(\hat{k}_q, \vec{r}')\vec{m}_{eq}(\vec{r}')d\vec{r}'$. Note that in case $kR_f \gg 1$ the translation operator goes to $T_L(\hat{k}_q, \vec{r}') \to j4\pi\frac{e^{-jkR_f}}{kR_f}\delta(\hat{r}' \cdot \hat{k}_q)$, and thus:

$$\vec{e}_i^{\,j}(\vec{r}) \simeq -jk\zeta\frac{e^{-jkR_f}}{kR_f}\int_0^{2\pi}\int_0^{\pi}\left(\overline{\overline{I}} - \hat{r}'\hat{r}'\right)\cdot\vec{j}_{eq}(\vec{r}')e^{j\vec{r}\vec{r}'}d\vec{r}' \tag{D.6a}$$

$$\vec{e}_i^{\,m}(\vec{r}) \simeq -jk\zeta\frac{e^{-jkR_f}}{kR_f}\int_0^{2\pi}\int_0^{\pi}\hat{r}' \times \vec{m}_{eq}(\vec{r}')e^{j\vec{r}\vec{r}'}d\vec{r}' \tag{D.6b}$$

The expressions (D.6) are valid only in a limited region surrounding the origin. The limiting radius r_a^{max} of this region can be evaluated assuming a 10% error in amplitude, and $\pi/8$ in phase, as described in [69], so that:

$$\vec{E}^{pws}(-\hat{k}_i) = -jkR_f\frac{e^{-jkR_f}}{kR_f}\left(-\hat{k}_i \times \zeta\vec{h}_i(R_f\hat{k}_i) + \hat{k}_i \times \left(\hat{k}_i \times \vec{e}_i(R_f\hat{k}_i)\right)\right) \tag{D.7}$$

Similarly, the spectrum of the magnetic field around the origin can be approximated in terms of the incident electric and magnetic fields, as follows:

$$\vec{h}_i(\vec{r}_a) = \frac{1}{\zeta}\int_0^{2\pi}\int_0^{\pi} -\hat{k}_i \times \vec{E}^{pws}(-\hat{k}_i)e^{jk\vec{r}_a\cdot\hat{k}_i}d\hat{k}_i \tag{D.8}$$

Appendix E

Evaluation of the amplitude of the observable field

The evaluation of the amplitude C of the observable field in (5.8) is expressed as a field reaction. This reaction is set as follows: the incident electric and magnetic fields are first expressed using the observable and the remaining fields, as in (5.1):

$$\vec{f}_i(\vec{r}_\infty) = C\vec{f}_{po}(\vec{r}_\infty) + \vec{f}_{rem}(\vec{r}_\infty) \tag{E.1}$$

Then, both the left-hand and the right-hand side of (E.1) are multiplied with a field test function, $\vec{f}_t(\vec{r}_\infty)$, and integrated over a sphere S_∞ in the far field of the antenna domain, as follows:

$$< \vec{f}_i(\vec{r}_\infty), \vec{f}_t(\vec{r}_\infty) >= C < \vec{f}_{po}(\vec{r}_\infty), \vec{f}_t(\vec{r}_\infty) > + < \vec{f}_{rem}(\vec{r}_\infty), \vec{f}_t(\vec{r}_\infty) > \tag{E.2}$$

where the reaction integral is defined as in (5.9).

The choice for the test function consists in the fields radiated by the ideal antenna when operated in transmission: $\vec{e}_t(\vec{r}_\infty) = \vec{e}_{tx}(\vec{r}_\infty), \vec{h}_t(\vec{r}_\infty) = \vec{h}_{tx}(\vec{r}_\infty)$. The fields $\vec{f}_{tx}$ radiated by the ideal can be expressed as those radiated by a set of equivalent currents defined over the antenna domain: $\vec{j}_{eq}(\vec{r}_a), \vec{m}_{eq}(\vec{r}_a)$. These currents are related to those describing the inward component of the observable field as:

$$\vec{j}_{tx}(\vec{r}_a) = -\vec{j}^*_{po}(\vec{r}_a) \tag{E.3a}$$

$$\vec{m}_{tx}(\vec{r}_a) = -\vec{m}^*_{po}(\vec{r}_a) \tag{E.3b}$$

Therefore, the angular distribution of the fields radiated by the antenna in transmission can be related to those of the observable field by the antenna in reception, as:

$$\vec{e}_{tx}(\vec{r}_\infty) = \vec{V}^{inw,*}_{po}(\hat{k})\frac{e^{-jkr_\infty}}{r_\infty} \tag{E.4a}$$

$$\vec{h}_{tx}(\vec{r}_\infty) = \frac{1}{\zeta}\hat{k} \times \vec{e}_{tx}(\vec{r}_\infty) \tag{E.4b}$$

The value of the constant C can then be obtained by solving (E.2) knowing that the reaction between the remaining field and the antenna angular distribution in (E.4) can be approximated to be zero: $< \vec{f}_{rem}(\vec{r}_\infty), \vec{f}_{tx}(\vec{r}_\infty) > \simeq 0$. This is because the remaining and observable fields are basically orthogonal, similar to the expansion of low and high order spherical modes as clarified in [52]. The fields radiated by the antenna have the same orthogonality property with the remaining field since they have the same angular distribution as the observable field, (E.4). With this approximation it follows that:

$$C = \frac{< \vec{f}_i(\vec{r}_\infty), \vec{f}_{tx}(\vec{r}_\infty) >}{< \vec{f}_{po}(\vec{r}_\infty), \vec{f}_{tx}(\vec{r}_\infty) >} \tag{E.5}$$

It is worth noting that the denominator in (E.5) can be related to the radiated power by the ideal antenna in transmission. In fact, expanding the angular distribution of the observable field in inward and outward components, $\vec{f}_{po} = \vec{f}^{inw}_{po} + \vec{f}^{outnw}_{po}$, one can easily demonstrate that $< \vec{f}^{outw}_{po}, \vec{f}_{tx} >= 0$, and thus:

$$< \vec{f}_{po}, \vec{f}_{tx} >=< \vec{f}^{inw}_{po}, \vec{f}_{tx} >= 4P^{tx}_{rad} \tag{E.6}$$

where P^{tx}_{rad} is the power radiated by the currents in (E.3), with $I_0 = 1$.

Appendix F

Transmission line modelling of bulk absorbers at sub-mm wave frequencies using Drude theory; theory and measurements

This appendix shows how using transmission line theory together with the Drude model leads to an efficient analysis and design of bulk absorbers in a vast range of frequencies, with specific focus on the (sub-) THz regime. The conductivity of the media is described as an electron gas with a controlled carrier density. The Drude model predicts the existence of two frequencies of interest: one associated with the carrier scattering time and one associated with plasma oscillations in the electron gas. Drude theory is useful to predict the behaviour of both good conductors, such as gold, as well as semiconductors (SC), which will obviously present different features.

With specific focus on semiconductor based bulk absorbers, it emerges that the dimensions for a specific frequency range of operation can be minimised by tuning the doping levels. Eventually, the maximum ohmic absorption from the medium is achieved when the real part of the characteristic impedance of the absorber is matched to the one of the surrounding medium, and when the imaginary part of the characteristic impedance is high enough so that the power entering the material is

transformed in heat.

Using a classic transmission line representation, a matching layer is introduced to further increase the absorption capabilities of an SC slab. Measurements using a TDSS system show the increased accuracy of the Drude model compared to the quasi-static approximation of the conductivity. The transmission line representation in combination with the Drude model proves to be a simple and accurate tool for integrated antenna front-end design and absorber optimisation.

The frequency dependent conductivity predicted by the Drude model is:

$$\sigma(\omega) = \frac{\sigma_{qs}}{1 + j\omega\tau} \tag{F.1a}$$

$$\sigma_{qs} = \frac{nq_e^2\tau}{m_0} \tag{F.1b}$$

where n is the electron density in the medium (holes contribution is neglected), τ is the carrier scattering time and the other parameters can be found in Table 2.1. The introduction of eq (F.1) in Maxwell's equation leads to the effective dielectric constant:

$$\varepsilon_{eff}(\omega) = \varepsilon_0\varepsilon_{r,eff} = \varepsilon_0\varepsilon_{r\infty}\left(1 - \frac{j\sigma(\omega)}{\omega\varepsilon_0\varepsilon_{r\infty}}\right) \tag{F.2}$$

The two frequencies of interest, related to the carrier scattering time, f_τ, and the plasma oscillations, f_p, are expressed as (note that $f = \omega/2\pi$):

$$f_\tau = \frac{1}{2\pi\tau} \tag{F.3a}$$

$$f_p = \frac{q_e\sqrt{n}}{2\pi\sqrt{\varepsilon_0\varepsilon_{r\infty}m_0}} \tag{F.3b}$$

By making the plasma frequency explicit in (F.2), one can separate real and imaginary part of the dielectric constant:

$$\varepsilon_{eff}(\omega) = \varepsilon_{r\infty}\left[1 - \omega_p^2\tau^2\frac{1}{1+\omega^2\tau^2}\right] - j\varepsilon_{r\infty}\omega_p^2\frac{\tau}{\omega}\frac{1}{1+\omega^2\tau^2} \tag{F.4}$$

Next, the characteristic impedance of a doped SC is:

$$\zeta(\omega) = \frac{\zeta_0}{\sqrt{\varepsilon_{r,eff}(\omega)}} = e^{j\pi/4}\sqrt{\frac{\mu_0\omega}{\sigma_{qs}}}\sqrt{\frac{1+\omega^2\tau^2}{1+j\gamma(\omega)}} \tag{F.5a}$$

$$\gamma(\omega) = \frac{\omega}{\omega_p^2\tau}(1+(\omega^2-\omega_p^2)\tau^2) \tag{F.5b}$$

The behaviour of $\zeta(\omega)$ is showed in Fig. F.1. In case of very low frequencies, $\omega \ll \omega_p$, the characteristic impedance corresponds to the Leontovich approximation for good conductors:

$$\gamma(\omega \ll \omega_p) = \sqrt{\frac{\mu_0\omega}{2\sigma_{qs}}}(1+j) \tag{F.6}$$

In case of very high frequencies, $\omega \gg \omega_p$, the characteristic impedance tends to the asymtptotic value:

$$\gamma(\omega \gg \omega_p) = \sqrt{\frac{\mu_0}{\varepsilon_0\varepsilon_{r\infty}}} \tag{F.7}$$

To validate Drude theory and the effective dielectric constant predicted by it, eq. (10.4), the TERA K15 from Menlo Systems GmbH [36] is adopted with its factory configuration, Fig. 1.1. The QO path consists in 4 lenses (Thorlabs TPX50) with an iris placed in the center. The iris is removed and the Si wafer to test is positioned in its place. The THz pulse is acquired with and without the Si wafer, so that from the difference in the two spectra the dielectric properties of the medium can be extrapolated.

The Si slab under test is much larger than the THz beam width in the transverse direction, $< x, y >$ plane, and has a thickness h in the longitudinal direction, z, with free-space around it. The beam profile is represented as an incident plane wave as:

$$\vec{E}_t(\vec{r}) = V(z)\hat{e}_t \tag{F.8}$$

The voltage is expressed resorting to a transmission line representation, Fig. F.2, where medium 1 and 3 are free space, while medium 2 is the Si slab:

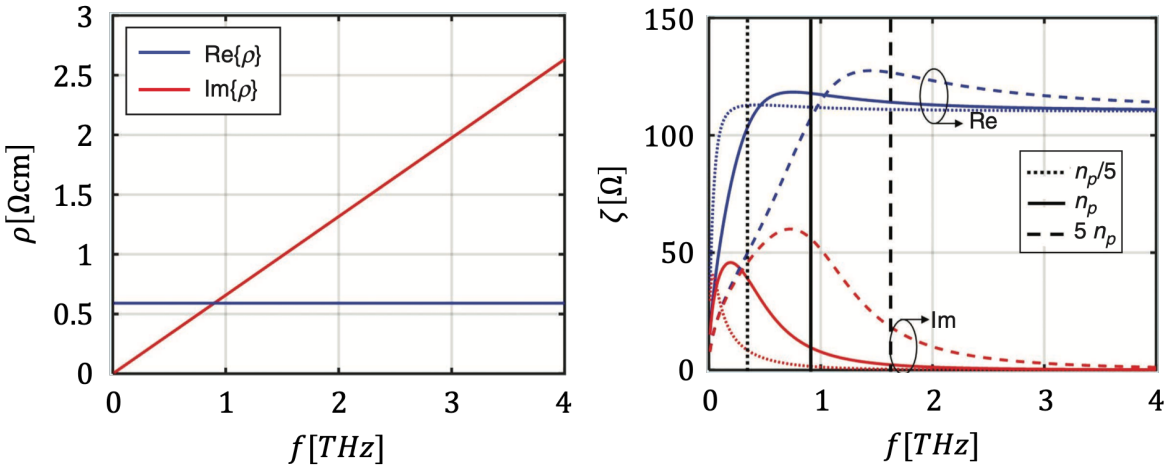

(a) (b)

Figure F.1: (a) Resistivity of doped Si ($n_p = 8.8 \times 10^{21} m^{-3}$), calculated with the given parameters as a function of the frequency. (b) Characteristic impedance of doped Si, calculated using the given parameters, for three levels of doping. The plasma frequencies, f_p, are indicated in the plot as vertical lines for each doping level.

$$V_i(z) = V_i^+ e^{-jk_i z} + V_i^- e^{jk_i z} \tag{F.9}$$

with $i = 1, 2, 3$ indicating the portion of space. The solution of the transmission line leads to:

$$V_3^+ = V_2^+(1 + \Gamma_{out}) = V_1^+ \frac{e^{jk_1 h}(1 + \Gamma_{in})(1 + \Gamma_{out})}{e^{jk_2 h} + \Gamma_{out} e^{-jk_2 h}} \tag{F.10}$$

where $\Gamma_{in} = (Z_{in2} - \zeta_0)/(Z_{in2} + \zeta_0), \Gamma_{out} = (\zeta_0 - \zeta)/(\zeta_0 + \zeta)$ are the voltage reflection coefficients at the cross sections $z = -h, z = 0$, respectively. Fig. F.3 shows the transmission coefficient $T = V_3^+/V_1^+$ as a function of the frequency for a slab of Si of thickness $h = 434 \mu m$ and declared resistivity $5 \Omega cm$. The value of $\varepsilon_{r,\infty}$ of the waver is found to be 10.5. A nominal resistivity $\rho_{qs} = 3.77 \Omega cm \rightarrow n = 1.16 \times 10^{21} m^{-3}$ led to the best fit. The scattering time is calculated as $\tau = \mu m_{Si}/q_e$. From the plot it is apparent that the frequency-independent nominal resistivity, or conductivity,

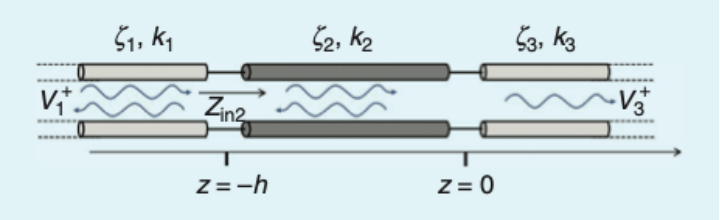

Figure F.2: The transmission line model representing the absorbing slab surrounded by a lossless host medium

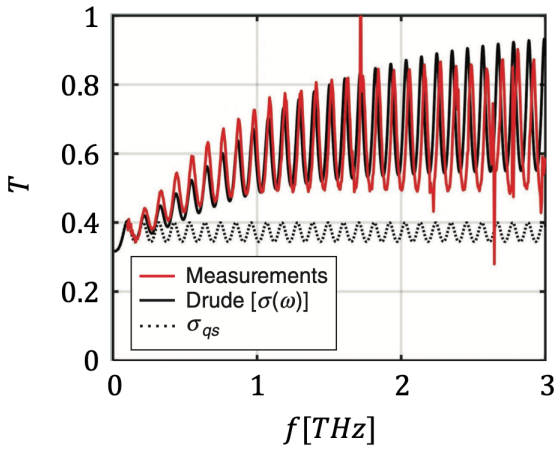

Figure F.3: The transmission through a doped Si slab, $h = 434\mu m, n = 1.16 \times 10^{21} m^{-3}$. Comparison between the measurements, the predictions of the Drude model and the quasi-static approximation.

cannot represent the losses in the dielectric slab at frequencies higher than a few hundred GHz. The transmission coefficient evaluated via the full Drude model and the measured one show very good agreement in measurement accuracy. The expected and measured oscillations are directly related to the multiple reflections at the dielectric air interfaces.

Next, the index of refraction ($\sqrt{\varepsilon_{r,eff}}$) is extracted with the TERA K15 software. The data are compared to the predictions from the Drude model and its quasi-static approximation, Fig. F.4 (a). In particular, a closer look at $\Im\sqrt{\varepsilon_{r,eff}}$, Fig. F.4 (b) - (d) shows that the quasi-static approximation holds only at low frequencies, while the measurements start to diverge from the prediction as the frequency increase. On the contrary, the Drude model well predicts the dominant features of the measurements, whose oscillations are given by the multiple reflection occurring in the slab.

The Drude model together with the transmission line representation in eq. (F.10) can thus be used to achieve more efficient absorber designs by tuning the doping, n, as well as the thickness, h, of the SC: the highest absorbing efficiency is achieved by the thinnest slab that absorbs the maximum power for a given frequency. By introducing a matching layer, the absorption can be as high as more than 95% of the incident power, with a slab of 1/5 of the wavelength in free space, [31].

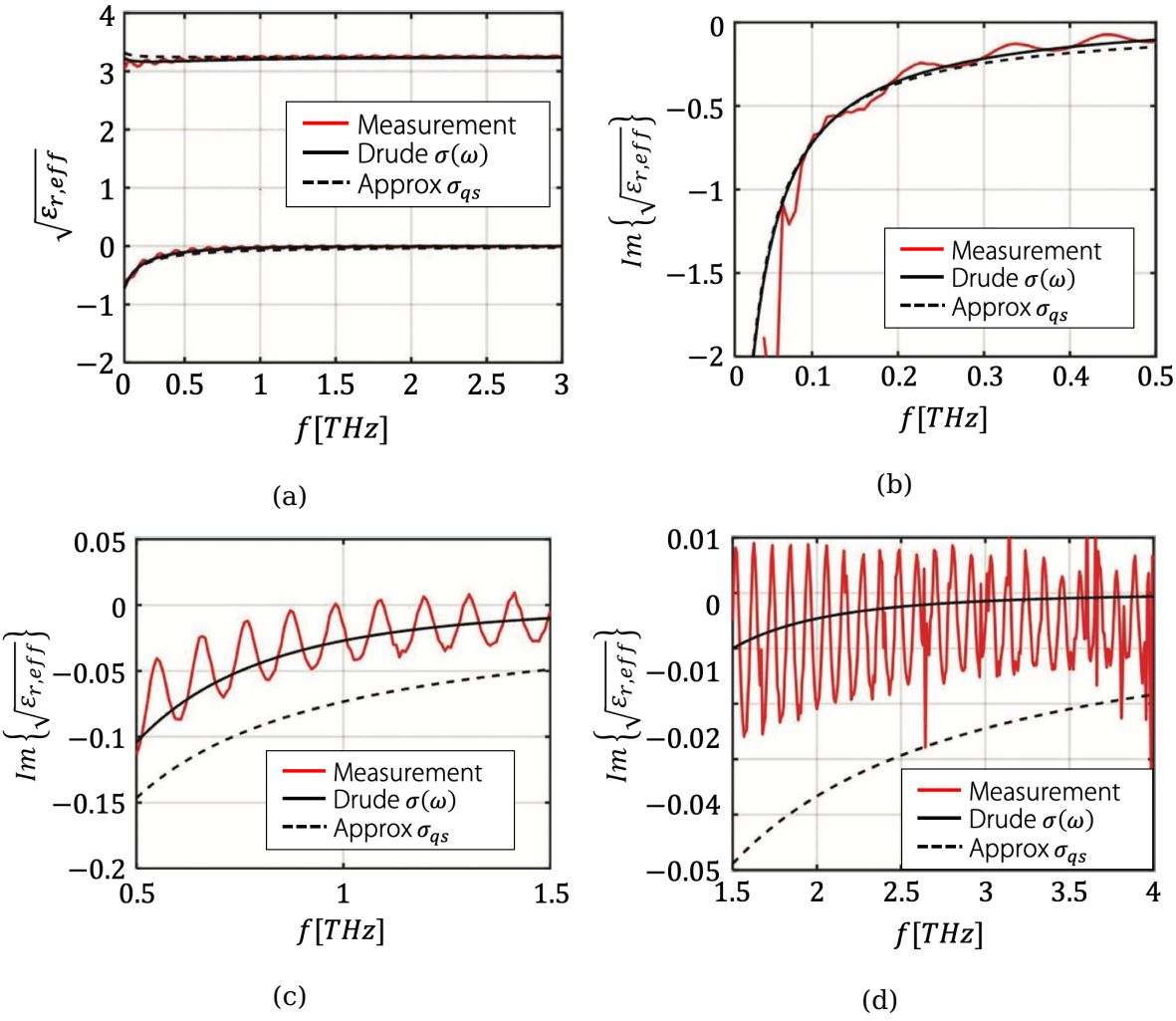

Figure F.4: Index of refraction of the Si slab with $h = 434\mu m, n = 1.16 \times 10^{21} m^{-3}$

Bibliography

[1] P Uhd Jepsen, David G Cooke, and Martin Koch. “Terahertz spectroscopy and imaging–Modern techniques and applications”. In: *Laser & Photonics Reviews* 5.1 (2011), pp. 124–166.

[2] Daryoosh Saeedkia. *Handbook of terahertz technology for imaging, sensing and communications*. Elsevier, 2013.

[3] Masayoshi Tonouchi. “Cutting-edge terahertz technology”. In: *Nature photonics* 1.2 (2007), pp. 97–105.

[4] Masanori Hangyo et al. “Spectroscopy and imaging by laser excited terahertz waves”. In: *Plasma and Fusion Research* 2 (2007), S1020–S1020.

[5] Philip F Taday. “Applications of terahertz spectroscopy to pharmaceutical sciences”. In: *Philosophical Transactions of the Royal Society of London. Series A: Mathematical, Physical and Engineering Sciences* 362.1815 (2004), pp. 351–364.

[6] T Globus et al. “THz-frequency spectroscopic sensing of DNA and related biological materials”. In: *International Journal of High Speed Electronics and Systems* 13.04 (2003), pp. 903–936.

[7] John F Federici et al. “THz imaging and sensing for security applications—explosives, weapons and drugs”. In: *Semiconductor Science and Technology* 20.7 (2005), S266.

[8] Min Ki Choi, Alan Bettermann, and DW Van Der Weide. “Potential for detection of explosive and biological hazards with electronic terahertz systems”. In: *Philosophical Transactions of the Royal Society of London. Series A:*

Mathematical, Physical and Engineering Sciences 362.1815 (2004), pp. 337–349.

[9] Yun-Shik Lee. *Principles of terahertz science and technology*. Vol. 170. Springer Science & Business Media, 2009.

[10] David H Auston, Kin P Cheung, and Peter R Smith. “Picosecond photoconducting Hertzian dipoles”. In: *Applied physics letters* 45.3 (1984), pp. 284–286.

[11] Stuart D Brorson, Jucheng Zhang, and So/ren R Keiding. “Ultrafast carrier trapping and slow recombination in ion-bombarded silicon on sapphire measured via THz spectroscopy”. In: *Applied physics letters* 64.18 (1994), pp. 2385–2387.

[12] WE Bron, J Kuhl, and BK Rhee. “Picosecond-laser-induced transient dynamics of phonons in GaP and ZnSe”. In: *Physical Review B* 34.10 (1986), p. 6961.

[13] Ian S Gregory et al. “High resistivity annealed low-temperature GaAs with 100 fs lifetimes”. In: *Applied physics letters* 83.20 (2003), pp. 4199–4201.

[14] Marian A Herman and Helmut Sitter. *Molecular beam epitaxy: fundamentals and current status*. Vol. 7. Springer Science & Business Media, 2012.

[15] MC Nuss, DH Auston, and F Capasso. “Direct subpicosecond measurement of carrier mobility of photoexcited electrons in gallium arsenide”. In: *Physical review letters* 58.22 (1987), p. 2355.

[16] N Vieweg et al. “Terahertz-time domain spectrometer with 90 dB peak dynamic range”. In: *Journal of Infrared, Millimeter, and Terahertz Waves* 35.10 (2014), pp. 823–832.

[17] D Grischkowsky et al. “Far-infrared time-domain spectroscopy with terahertz beams of dielectrics and semiconductors”. In: *JOSA B* 7.10 (1990), pp. 2006–2015.

[18] P Uhd Jepsen, Rune Hylsberg Jacobsen, and SR Keiding. “Generation and detection of terahertz pulses from biased semiconductor antennas”. In: *JOSA B* 13.11 (1996), pp. 2424–2436.

[19] S Verghese, KA McIntosh, and ER Brown. “Highly tunable fiber-coupled photomixers with coherent terahertz output power”. In: *IEEE Transactions on microwave theory and techniques* 45.8 (1997), pp. 1301–1309.

[20] Alessandro Garufo et al. “A connected array of coherent photoconductive pulsed sources to generate mW average power in the submillimeter wavelength band”. In: *IEEE Transactions on Terahertz Science and Technology* 9.3 (2019), pp. 221–236.

[21] Alessandro Garufo. *Towards the engineering of pulsed photoconductive antennas*. 2017.

[22] Nuria Llombart and Andrea Neto. “THz time-domain sensing: The antenna dispersion problem and a possible solution”. In: *IEEE Transactions on Terahertz science and technology* 2.4 (2012), pp. 416–423.

[23] Masahiko Tani et al. “Emission characteristics of photoconductive antennas based on low-temperature-grown GaAs and semi-insulating GaAs”. In: *Applied optics* 36.30 (1997), pp. 7853–7859.

[24] Zhisheng Piao, Masahiko Tani, and Kiyomi Sakai. “Carrier dynamics and terahertz radiation in photoconductive antennas”. In: *Japanese Journal of Applied Physics* 39.1R (2000), p. 96.

[25] Karsten J Siebert et al. “Field screening in low-temperature-grown GaAs photoconductive antennas”. In: *Japanese journal of applied physics* 43.3R (2004), p. 1038.

[26] OA Castañeda-Uribe et al. “Comparative study of equivalent circuit models for photoconductive antennas”. In: *Optics express* 26.22 (2018), pp. 29017–29031.

[27] Gabriel C Loata et al. “Radiation field screening in photoconductive antennae studied via pulsed terahertz emission spectroscopy”. In: *Applied Physics Letters* 91.23 (2007), p. 232506.

[28] Alessandro Garufo et al. “Norton equivalent circuit for pulsed photoconductive antennas–Part I: Theoretical model”. In: *IEEE Transactions on Antennas and Propagation* 66.4 (2018), pp. 1635–1645.

[29] Alessandro Garufo et al. “Norton equivalent circuit for pulsed photoconductive antennas—Part II: Experimental validation”. In: *IEEE Transactions on antennas and propagation* 66.4 (2018), pp. 1646–1659.

[30] Paul Drude. “Zur elektronentheorie der metalle; II. Teil. galvanomagnetische und thermomagnetische effecte”. In: *Annalen der physik* 308.11 (1900), pp. 369–402.

[31] Ralph Matthijs van Schelven et al. “Drude Dispersion in the Transmission Line Modelling of Bulk Absorbers at Sub-mm Wave Frequencies: A Tool for Absorber Optimization”. In: *IEEE Antennas and Propagation Magazine* (2021), pp. 2–12.

[32] D Grischkowsky. “Nonlinear generation of sub-psec pulses of THz electromagnetic radiation by optoelectronics–applications to time-domain spectroscopy”. In: *Frontiers in Nonlinear Optics* (2021), pp. 196–227.

[33] Jie Shan and Tony F Heinz. “Terahertz Radiation from Semiconductors”. In: *Ultrafast Dynamical Processes in Semiconductors*. Springer Berlin Heidelberg, 2004, pp. 1–56.

[34] Andrea Neto, Angelo Freni, and Nuria Llombart. “On the Accurate Characterization of Pulsed Photo Conductive Sources: The Norton Circuit in Time Domain”. In: *IEEE submitted* ().

[35] Asahi Glass Co. ltd AGC Chemicals. URL: `http://www.agc.com/kagaku/shinsei/cytop/en/`.

[36] Menlo Systems GmbH. URL: `https://www.menlosystems.com/`.

[37] Inc. Virginia Diodes. URL: `https://www.vadiodes.com/en/`.

[38] Thorlabs GmbH. URL: `https://www.thorlabs.com/`.

[39] John M Khosrofian and Bruce A Garetz. “Measurement of a Gaussian laser beam diameter through the direct inversion of knife-edge data”. In: *Applied optics* 22.21 (1983), pp. 3406–3410.

[40] CST Microwave Studio. URL: `http://www.cst.com/`.

[41] TU Delft TeraHertz Sensing Group. URL: `http://terahertz.tudelft.nl/Research/project.php?id=155&pid=25`.

[42] TICRA Grasp. URL: http://www.ticra.com/software/grasp.

[43] B Globisch et al. “Carrier dynamics in Beryllium doped low-temperature-grown InGaAs/InAlAs”. In: *Applied Physics Letters* 104.17 (2014), p. 172103.

[44] H Roehle et al. “Next generation 1.5 μm terahertz antennas: mesa-structuring of InGaAs/InAlAs photoconductive layers”. In: *Optics express* 18.3 (2010), pp. 2296–2301.

[45] Sumipro BV. URL: https://www.sumipro.nl/.

[46] Inigo Liberal and Richard W Ziolkowski. “Analytical and equivalent circuit models to elucidate power balance in scattering problems”. In: *IEEE transactions on antennas and propagation* 61.5 (2013), pp. 2714–2726.

[47] J Bach Andersen and Aksel Frandsen. “Absorption efficiency of receiving antennas”. In: *IEEE Transactions on Antennas and Propagation* 53.9 (2005), pp. 2843–289.

[48] Hamid Shannan and Raphael Kastner. “On the incident power on a receiving slender antenna and the optical theorem in the near field”. In: *IEEE Transactions on Antennas and Propagation* 65.5 (2017), pp. 2421–2427.

[49] L Brillouin. “The scattering cross section of spheres for electromagnetic waves”. In: *Journal of Applied Physics* 20.11 (1949), pp. 1110–1125.

[50] Do-Hoon Kwon and David M Pozar. “Optimal characteristics of an arbitrary receive antenna”. In: *IEEE Transactions on Antennas and Propagation* 57.12 (2009), pp. 3720–3727.

[51] Per-Simon Kildal, Enrica Martini, and Stefano Maci. “Degrees of Freedom and Maximum Directivity of Antennas: A bound on maximum directivity of nonsuperreactive antennas”. In: *IEEE Antennas and Propagation Magazine* 59.4 (2017), pp. 16–25.

[52] Andrea Neto, Nuria Llombart, and Angelo Freni. “The observable field for antennas in reception”. In: *IEEE Transactions on Antennas and Propagation* 66.4 (2018), pp. 1736–1746.

[53] Theodore S Rappaport et al. “Millimeter wave mobile communications for 5G cellular: It will work!” In: *IEEE access* 1 (2013), pp. 335–349.

[54] Bo Xu et al. “Radiation performance analysis of 28 GHz antennas integrated in 5G mobile terminal housing”. In: *Ieee Access* 6 (2018), pp. 48088–48101.

[55] Wonbin Hong. “Solving the 5G mobile antenna puzzle: Assessing future directions for the 5G mobile antenna paradigm shift”. In: *IEEE microwave magazine* 18.7 (2017), pp. 86–102.

[56] Shuai Zhang et al. “A planar switchable 3-D-coverage phased array antenna and its user effects for 28-GHz mobile terminal applications”. In: *IEEE Transactions on Antennas and Propagation* 65.12 (2017), pp. 6413–6421.

[57] Igor Syrytsin et al. “Compact quad-mode planar phased array with wideband for 5G mobile terminals”. In: *IEEE Transactions on Antennas and Propagation* 66.9 (2018), pp. 4648–4657.

[58] Wonil Roh et al. “Millimeter-wave beamforming as an enabling technology for 5G cellular communications: Theoretical feasibility and prototype results”. In: *IEEE communications magazine* 52.2 (2014), pp. 106–113.

[59] Mathew K Samimi and Theodore S Rappaport. “Ultra-wideband statistical channel model for non line of sight millimeter-wave urban channels”. In: *2014 IEEE Global Communications Conference*. IEEE. 2014, pp. 3483–3489.

[60] Marta Arias Campo et al. “On the use of fly’s eye lenses with leaky-wave feeds for wideband communications”. In: *IEEE Transactions on Antennas and Propagation* 68.4 (2020), pp. 2480–2493.

[61] V Rumsey. “On the design and performance of feeds for correcting spherical aberration”. In: *IEEE Transactions on Antennas and Propagation* 18.3 (1970), pp. 343–351.

[62] Ting Wu, Theodore S Rappaport, and Christopher M Collins. “The human body and millimeter-wave wireless communication systems: Interactions and implications”. In: *2015 IEEE International Conference on Communications (ICC)*. IEEE. 2015, pp. 2423–2429.

[63] N Llombart et al. “Fly’s eye spherical antenna system for future Tbps wireless communications”. In: *Proc. Eur. Conf. Antennas Propag.(EuCAP)*. 2017, pp. 1–4.

[64] Jin Liu et al. “High-Q optomechanical GaAs nanomembranes”. In: *Applied Physics Letters* 99.24 (2011), p. 243102.

[65] Yuji Uenishi, Hidenao Tanaka, and Hiroo Ukita. “Characterization of AlGaAs microstructure fabricated by AlGaAs/GaAs micromachining”. In: *IEEE transactions on electron devices* 41.10 (1994), pp. 1778–1783.

[66] Christine Bryce. “A kinetic study of gallium arsenide etching in H2O2-NH4OH-H2O solutions”. In: (1996).

[67] AMMT GmbH. URL: `http://www.ammt.com/products/wet-etching/`.

[68] Julius Adams Stratton. *Electromagnetic theory*. Vol. 33. John Wiley & Sons, 2007.

[69] Nuria Llombart et al. “Fourier optics for the analysis of distributed absorbers under THz focusing systems”. In: *IEEE Transactions on Terahertz Science and Technology* 5.4 (2015), pp. 573–583.

Summary

In recent years, the interest in terahertz technology witnessed a constant increasing interest and attention from the scientific community, as it allows to unlock the THz bandwidth, that can be used for a wide range of applications: it helps the study of biological samples and help medical diagnostics; it serves as a harmless non-destructive testing technique for medical and pharmaceutical products; it is used to inspect food and other packaging for quality control in a non-invasive fashion; it is adopted in body scanner systems for security screenings of people.

Photoconductive antennas are optoelectronic sources that radiate and detect electromagnetic fields in the THz spectrum, and represent the driving component of TDSS systems, typically employed for the aforementioned applications. PCAs consist in a metallization printed over a substrate of semiconductor and radiating into a dense dielectric lens, while excited by pulsed lasers.

Even though PCAs come at a relatively low cost, thanks to the advancements in semiconductor technology, they typically suffer from low levels of radiated power. This worsens the signal to noise ratio of the link, which in turns requires long integration times to detect the wanted signals and makes them inconvenient for long range applications. To obviate to the issue and increase the radiate power, the THz community mainly focused on the engineering of the semiconducting substrate, with little focus on the radiation characteristic of the antennas.

The work presented throughout this thesis aims to bridge the gap between this two aspects: it has been developed a novel equivalent circuit containing both the parameters on the material and the behaviour of the photocarrier as well as the radiation properties of the architecture. The model is constructed starting from a thorough analysis of the physical processes involved in the induction of the current in a biased photoconductor excited by a pulsed laser, an equivalent

circuit model in time domain including the antenna response is then derived. The model can be translated in the frequency domain to include the electromagnetic features of the whole link, such as the quasi optical channel efficiency. This allows a complete analysis of the power budget of the entire system, from the laser exciting the transmitter to the pulse detected by the receiver, while accounting for all the characteristics of the optical signal, the semiconductor, the antenna geometry and the quasi optical channel.

Moreover, the equivalent circuit predicts with great accuracy the saturation in the power radiated by PCAs happening under large optical excitations, and it gives an immediate and clear physical picture of what causes it, *i.e.* a screening on the bias applied over the antenna gap by the radiation of the device itself.

The equivalent circuit is tested with a campaign of measurement of PCAs. Specifically, two PCAs are characterised during the campaign: one bow tie PCA, and one leaky wave PCA which, for the first time, is adopted as PCA. For both antenna an *ad-hoc* measurement set up is built, using as optical source and read out electronics a TDSS system commercially available: the TERA K15 from Menlo Systems GmbH.

The bow tie PCA is characterised first by detecting its radiated power as a function of the laser power exciting it for three different bias point. The agreement with the predictions of the equivalent circuit is very good, with differences lying within 1dB; also the saturation of the THz radiated power under large optical excitations is well predicted and ascribed to field screening induced by the radiation itself over the gap of the antenna. Then, the antenna is made communicate with the native receiver of the TERA K15. The collected time domain pulse and thus its spectrum are heavily affected by the receiver, whose impulse response is not known and that is not efficient for frequencies below 250 GHz. However, a good agreement is found between the predictions of the model of the radiated spectra and the gathered data, even though the behaviour of the Auston switch is not defined.

The leaky wave PCA is characterised first by detecting its radiated power as a function of the laser power exciting it for three different bias point. The agreement with the predictions of the equivalent circuit is good, with differences lying around 1dB; also the saturation of the THz radiated power under large optical excitations

is well predicted and ascribed to field screening induced by the radiation itself over the gap of the antenna. However, the leaky wave PCA saturates much faster than the bow tie PCA, mainly due to its larger radiation impedance.

Finally, the observable field is derived for a general incident field. The methodology is applicable to any field, and results especially beneficial in environments where the incident field is composed of multiple coherent planes waves, such as those present in sensing (e.g. communicating PCAs in TDSS systems) scenarios, with receivers located close to multiple scatterers. In particular, the observable field is defined as the portion of the incident field that can contribute to the signal received by an antenna occupying a fixed spherical volume. After describing the incident field as a superposition of homogeneous plane waves distributed over a spherical surface via its plane wave spectrum, the observable field is represented as the sum of an inward and an outward propagating spherical wave. The inward/outward component of the observable field has an angular distribution that is equal to the PO field radiated by equivalent currents defined on the truncated surface of the antenna domain. The amplitude of the observable field is instead obtained by exploiting the reciprocity theorem to project the incident field onto the PO field. An ideal antenna operated in reception should scatter a field which is equal but opposite to the outward propagating wave of the observable field cancelling it out. In other words, the ideal antenna absorbs the entire inward propagating power of the observable field.

Samenvatting

De afgelopen jaren worden gekenmerkt door alsmaar toenemende interesse en aandacht voor terahertz technologie vanuit de wetenschappelijke gemeenschap om de terahertz bandbreedte te benutten die een heel scala aan toepassingen kent: hulp bij het bestuderen van biologische monsters en bij medische diagnostiek; het dient als onschadelijke niet-destructieve testtechniek voor medische en farmaceutische producted; het wordt gebruikt om eten en verpakkingen op niet-invasieve wijze te inspecteren voor kwaliteitsdoeleinden en het wordt gebruikt in lichaamsscanners ten behoeve van beveiliging.

Fotogeleidende antennes (PCAs) zijn opto-elektronische bronnen die elektromagnetische velden zenden en ontvangen in het THz spectrum. Zij vormen het hoofdonderdeel van TDS-systemen (tijddomeinspectroscopie) die veelal in gebruik zijn bij bovengenoemde toepassingen. PCAs bestaan uit een metaallaag die op een halfgeleidersubstraat wordt bedrukt en vervolgens in elektromagnetische straling uitzenden in een dichte, dielektrische lens onder invloed van een pulserende laser. Ondanks de relatief lage kosten van PCAs door voortgang in halfgeleidertechnologie, hebben zij vaak te lijden onder een lage hoeveelheid zendvermogen. Dit komt de signaal-ruisverhouding van de draadloze verbinding niet ten goede, wat resulteert in lange integratietijd om de gewenste signalen te detecteren en wat ze ongeschikt maakt voor langeafstandsverbindingen. Om het zendvermogen te verhogen is de THz gemeenschap voornamelijk geënd geweest op het verbeteren van het halfgeleidersubstraat met weinig aandacht voor de zendeigenschappen van de antennes.

Het werk in dit proefschrift beoogt de kloof tussen deze twee aspecten te beslechten: een nieuw equivalent circuit is ontwikkeld dat zowel de materiaalparameters en gedrag van de fotogeleider als de zendeigenschappen van het geheel

bevat. Het model is opgebouwd vanuit een grondige analyse van de natuurkundige processen die betrokken zijn bij het induceren van stromen in een gebiasde fotogeleider onder invloed van een pulserende laser. Een tijddomein equivalent circuitmodel, die ook de reactie van de antenne omvat, werd daarna afgeleid. Het model kan worden vertaald naar het frequentiedomein om de elektromagnetische eigenschappen van het gehele kanaal, zoals de quasi-optische kanaalefficientie, mee te rekenen. Hierdoor is het mogelijk om een complete analyse van het vermogensbudget, van laserbelichting van de bron tot aan de puls bij de ontvanger, uit te voeren waarbij rekening wordt gehouden met alle karakteristieken van het optische signaal, de halfgeleider, de opbouw van de antenne en het quasi-optische kanaal.

Het equivalente circuitmodel voorspelt tevens met grote nauwkeurigheid de vermogensverzadiging die optreedt bij PCAs onder grote optische blootstelling en geeft onmiddelijk een helder en fysisch beeld van de oorzaak, dat wil zeggen: veldverscherming over het gat van de antenne door straling van de antenne zelf. Het equivalente circuitmodel is op de proef gesteld door metingen aan PCAs uit te voeren. In het bijzonder zijn twee PCAs gekarakteriseerd: een vlinderdas PCA en een lekgolf PCA die, voor het eerst, als PCA gebruikt is. Voor beide antennes zijn ad hoc meetopstellingen gemaakt, gebruikmakend van commercieel verkrijgbare optische bronnen en uitleeselektronica: de TERA K15 gemaakt door Menlo Systems GmbH.

De karakteristieken van de vlinderdas PCA zijn gevonden door eerst het zendvermogen als functie van het laservermogen te meten voor drie verschillende biaspunten. De overeenkomst tussen de metingen en voorspellingen uit het equivalente circuitmodel zijn uitstekend, de grootste verschillen liggen binnen 1 dB; ook de verzadiging van het THz zendvermogen bij grote optische blootstellingen wordt goed voorspeld en wordt toegeschreven aan veldverscherming die veroorzaakt wordt door de straling zelf over het gat van de antenne. Vervolgens is de antenne gebruikt in combinatie met de ingebouwde ontvanger van de TERA 15K. De ontvangen tijddomeinpuls, en daarmee het spectrum, wordt hevig beïnvloed door de ontvanger, waarvan de impulsresponsie onbekend is en die niet efficient werkt onder 250 GHz. Desalniettemin is een goede gelijkenis gevonden tussen het gemodelleerde uitgestraalde spectrum en de vergaarde data, ondanks het

ongedefieerde gedrag van de Auston-schakelaar.

De karakteristieken van de lekgolf PCA zijn gevonden door eerst het zendvermogen als functie van het laservermogen te meten voor drie verschillende biaspunten. De overeenkomst tussen de metingen en voorspellingen uit het equivalente circuitmodel zijn uitstekend, de grootste verschillen liggen binnen 1 dB; ook de verzadiging van het THz zendvermogen bij grote optische blootstellingen wordt goed voorspeld en wordt toegeschreven aan veldverscherming veroorzaakt door de straling zelf over het gat van de antenne. Echter, verzadigt de lekgolf PCA veel sneller dan de vlinderdas PCA, voornamelijk door de hogere stralingsimpedantie.

Tot slot is het waarneembare veld afgeleid voor generieke invallende velden. De methode is op elk veld toepasbaar en leidt voornamelijk tot voordelen in gevallen waar het invallende veld bestaat uit meerdere coherente vlakke golven, zoals voorkomt bij detectie-opstellingen (b.v. communicerende PCAs in TDS-systemen) waarbij ontvangers dicht bij meerdere verstrooiers staan. In het bijzonder wordt het waarneembare veld gedefineerd als dat deel van het invallende veld dat kan bijdragen aan het signaal dat wordt ontvangen door een antenna van een bepaald bolvormig volume. Nadat het invallende veld is beschreven als een superpositie van homogene vlakke golven verdeeld over een bolvormig oppervlak met behulp van het vlakkegolfspectrum, wordt het waarneembare veld beschreven als de som van een inkomende- en uitgaande sferische golf. De inkomende- en uitgaande componenten van het waarneembare veld hebben een hoekverdeling die gelijk is aan het PO-veld dat wordt uitgestraald door equivalente stromen die bestaan op het afgekapte oppervlak van het antennedomein. De amplitude van het waarneembaar veld wordt daarentegen verkregen door gebruik van het wederkerigheidstheorema om het inkomend veld te projecteren op het PO veld. Een ideëele antenne die gebruikt wordt als ontvanger zal een veld moeten verstrooien die gelijk is, maar tegengesteld in richting aan het uitgaande golf van het waarneembaar veld waardoor zij wordt uitgedoofd. Met andere woorden, de ideëele antenne neemt het gehele invallende vermogen van het waarneembare veld op.

List of publications

1. Arturo Fiorellini Bernardis et al. “Time Domain Modelling of Pulsed Photo Conducting Sources. Part II: Characterization of a LT GaAs Bow Tie Antenna”. In: *IEEE Transactions on Antennas and Propagation, under review* (2022)

2. Arturo Fiorellini Bernardis et al. “Fabrication and characterisation of leaky wave photo-conductive antennas for higher power fibre-based THz time domain systems”. In: *IEEE Transactions on Terahertz Science and Technology, in preparation* (2022)

3. Andrea Neto et al. “The Observable Field in Complex Scattering Scenarios”. In: *IEEE Transactions on Antennas and Propagation* 68.7 (2020), pp. 5544–5555

4. Ralph Matthijs van Schelven et al. “Drude Dispersion in the Transmission Line Modelling of Bulk Absorbers at Sub-mm Wave Frequencies: A Tool for Absorber Optimization”. In: *IEEE Antennas and Propagation Magazine* (2021), pp. 2–12

5. Andrea Neto et al. “The Observable Field for a Multiple Plane Wave Incidence”. In: *2018 12th European Conference on Antennas and Propagation (EuCAP)*. EurAAP. 2018

6. Arturo Fiorellini Bernardis et al. “The Observable Field for Generalized Incidences”. In: *13th European Conference on Antennas and Propagation (EuCAP)*. EurAAP. 2019

7. Arturo Fiorellini Bernardis et al. “Signal to Noise Ratio for a Pico-Second

Pulsed Radar for Imaging at Stand-Off Distances". In: *13th European Conference on Antennas and Propagation (EuCAP)*. EurAAP. 2019

8. Arturo Fiorellini Bernardis et al. "The Observable Field for Generalized Incident Fields". In: *Antennas and Propagation Society Symposium (APS)*. IEEE. 2019

9. Arturo Fiorellini Bernardis et al. "Signal to Noise Ratio Budget of a Pico-Seconds Pulsed Radar System for Stand-Off Imaging". In: *2019 44th International Conference on Infrared, Millimeter, and Terahertz Waves (IRMMW-THz)*. IEEE. 2019

10. Arturo Fiorellini Bernardis et al. "Time Domain Circuit Representation of Photoconductive Gaps in Antennas for Pulsed Terahertz Time Domain Systems". In: *2019 44th International Conference on Infrared, Millimeter, and Terahertz Waves (IRMMW-THz)*. IEEE. 2019

11. Arturo Fiorellini Bernardis et al. "On the Accurate Characterization of Pulsed Photoconductive Sources: Theory versus Measurements". In: *15th European Conference on Antennas and Propagation (EuCAP)*. EurAAP. 2021

12. Arturo Fiorellini Bernardis et al. "On the Power Radiated by Photo Conductive Sources". In: *46th International Conference on Infrared, Millimeter and Terahertz Waves (IRMMW-THz)*. IEEE. 2021

13. Paolo Maria Sberna et al. "Leaky Lens Photo-Conductive Antennas on LT GaAs membranes". In: *46th International Conference on Infrared, Millimeter and Terahertz Waves (IRMMW-THz)*. IEEE. 2021

Propositions Accompanying the Doctoral Thesis

1. The time domain equivalent circuit representation of transmitting photoconductive antennas hereby introduced works well when the antenna radiation impedance is characterised by an approximately constant real part and a negligible imaginary part (pertaining to this dissertation, Chapter 2, 3, 4).

2. The engineering of the material properties alone is not enough to push a photoconductive antenna to its limits (pertaining to this dissertation, Chapter 2, 3, 4).

3. Under the same biasing and excitation conditions of the typically adopted Auston switch, the leaky wave PCA generates more power, with better spectra and higher directivity, even when printed over a simple LT GaAs substrate (pertaining to this dissertation, Chapter 4).

4. The observable field gives the designer the optimal current distribution to synthesise if the incident field is known. To manufacture such an antenna, though, might be not feasible (Pertaining to this dissertation, chapter 5).

5. ”Hard work beats mere talent”, paraphrased from discussions with Prof. Neto.

6. The human mind tends to reduce intricate systems into much simpler versions, and to find an immediate solution to complex problems. Often times, this brings one to neglect some fundamental aspects of the question and to arrive to the wrong answer. Critical thinking demands practice.

7. Everyone filters reality based on their own attitude and experience, and to find one's own correct interpretation of facts can be incredibly painful. One thing is to agree with an interpretation, another is to own it, to feel it. In the end, however, facts are just facts.

8. "It gets easier. Everyday, it gets a little easier. But you gotta do it everyday. That's the hard part. But it does get easier", from the Jogging Baboon in BoJack Horseman, Raphael Bob-Waksberg.

9. "A man learns nothing from winning. The act of losing, however, can elicit great wisdom. Not least of which is, how much more enjoyable it is to win. It's inevitable to lose now and again. The trick is not to make a habit of it", from A Good Year, Ridley Scott.

10. "We cannot go back. That's why it's hard to choose. You have to make the right choice. As long as you don't choose, everything remains possible", from Mr Nobody, Jaco Van Dormael.

About the Author

Arturo Fiorellini Bernardis was born on August 24th, 1992, in Padua, Italy. He received his B.Sc in Biomedical Engineering from the Polytechnic University of Milan (Politecnico di Milano), Milan, Italy, in 2014. He received his M.Sc. (*cum laude*) in Electrical Engineering, Microelectronics, from the Delft University of Technology (TUDelft), Delft, the Netherlands, in a conjunct programme with the Polytechnic University of Milan, in 2017. During his master's he specialised in analog and digital integrated circuits first, to focus then on a thesis project on advanced antenna architectures.

From September 2017 to February 2022 he pursued the Ph.D. degree at the TeraHertz Sensing Group of the Delft University of Technology. During this period, his research interests involved photoconductive antennas, terahertz time-domain and spectroscopy systems, advanced antenna architectures, radar systems and analytical/numerical techniques in electromagnetics. This research has been carried out under the supervision of Prof. Andrea Neto and Prof. Nuria Llombart as promotors, and resulted in 4 journal publications (published, under review or in preparation) together with 9 conference papers (one nominated and runner up for the *Best Student Paper Award* at the European Conference on Antennas and Propagation (EuCAP), Krakow, Poland, 2019).

Acknowledgements

To my promotors, Professor Nuria Llombart and Professor Andrea Neto, for having led me to the end. Thank you for having kept me on the right track while letting me wander enough to realise when I was wrong without getting lost. And thank you for having tried to teach me to seek for help and guidance: I am aware of how crucial that is, and I will manage, sooner or later. I hope.

To Dr. Paolo Sberna, for having offered me a different point of view. Thank you for your friendship and your support, for all the dinners together, and for your selfless advices. People like you are rare, I know you have great things ahead.

To Dr. Juan Bueno, for your experience. Thank you for having showed me that details matter, and that to conduct experiments in a properly-organised, tidy lab does speed everything up.

To Sjoerd and Ralph, for the office. Thank you for the small and big talks, for the coffees and the beers; and for the help, whenever and for whatever it was needed. Needless to say, best room in the building. Stroopwafel.

To my family; to my dad, to my mom, and to Alvi. You were, and still are, the starting point. Needless to say, none of this would make any sense without you. Thanks for the money as well, that is also quite important, I am not going to lie. Exactly the same words as in my Master thesis: nothing has changed, and it never will.

To my friends, for whoever you were, are and will be. People change and so do relationships. This is to you, in the moment you are reading this. I hope these words find you well.

To Vittoria, for I finally have found you. You are so much more than words, they are wasted on you. Grazie.